Novel applications of luminescence for solar energy

by

José João Henriques Videira

A Thesis submitted for the degree of Doctor of Philosophy

Department of Physics

Imperial College London

September 2016

Declaration of Originality

I, José João Henriques Videira, hereby declare that this thesis represents my original work undertaken solely by myself or collaboratively with colleagues, and that I have used no other sources except as noted by citations. All data, figures and text citations which have been reproduced from any other sources, including journals and the internet, have been explicitly acknowledged as such.

Copyright Declaration

Abstract

Luminescent solar concentrators (LSCs) provide indirect light concentration by absorbing both direct and indirect incident light, and have applications in building-integrated photovoltaics (BIPV). Fibre LSCs were found to have a linear relationship between photon concentration and fibre lengths in scales suitable for LSC modules. Using raytrace modelling, cylindrical LSC arrays were found to exhibit light trapping properties at certain angles of incidence, which can pave the way for more efficient BIPV applications.

Novel optics for a double-illuminated water splitting reactor were introduced, for the objective of solar hydrogen for energy storage and sustainable transport fuels. A reflective cone embedded in a waveguide reflects incident concentrated light into the waveguide. Raytrace modelling and practical high concentration measurements demonstrate the viability of the optical system as well as necessity for a perfectly smooth reflective cone. It was also shown that replaced the reflective cone with a quantum well solar cell (QWSC) in order to harness the photoluminescence (PL) is not a viable concept with current QWSC structures.

Another form of sustainable transport fuels is to use biofuels produced by algae. Algae have evolved to absorb excess amounts of energy, even when it is detrimental to their own growth and survival. This causes inefficiencies when growing algae in raceway ponds. The luminescent solar diffuser (LSD) is an optical funnel, optimisable by use of a genetic algorithm, that can be retrofitted into an algae raceway pond in order to better distribute incident light into the pond depths. This was calculated to increase algae growth rates in the pond, thereby increasing the yield of an algae farm.

Acknowledgements

I would like to thank Dr. Amanda Chatten for giving me the opportunity to enter the world of academia. The greatest thanks goes to Dr. Ned Ekins-Daukes for his outstanding supervision. His depth of knowledge and understanding of solar energy is remarkable and it has provided me with a fantastic learning experience, not only in luminescent solar concentrators but in solar power in general. The support he has given me in this PhD is also something I am eternally grateful for. Prof. Emer. Keith Barnham to this day is still highly excitable for research and some of this vigour rubbed off on me during my time here. I also want to thank Dr. Paul Stavrinou for taking the mantle as co-supervisor, and providing support during my time here at Imperial College.

I have been fortunate enough to work with some fantastic scientists on various projects. I'd like to thank Dr. Anna Hankin and Prof. Geoff Kelsall for introducing me to the world of solar fuels, Dr. Emiliano Bilotti for his expertise on fibre manufacturing and his generous contribution of time and material resources and Tom Wilson for allowing me to incorporate pvtrace into his genetic algorithm. Not only can I thank Dr. Mauro Pravettoni for guidance on high concentration measurements, but also on his second-to-none hospitality in Milan; highlights being a cycling tour of the Milan countryside (he is the only person to have seen me in cycling lycra) and trip to the Expo. Dr. Dan Farrell and Dr. Markus Fuhrer were instrumental in helping me to code and improving pvtrace, whilst Dr. Diego Alonso-Alvarez and Dr. Martyn Fisher were amazingly helpful in guiding me through lab techniques. The whole EXSS group have been incredibly supportive and helpful during my time here.

A great research group and office makes for a fantastic work environment. The QPV group, always willing to help...and have cheeky ones down in hbar or the union: Tomos(that's a weird name, man), Tom, Nic, Anthony, Avi, Alex, Megumi and James. Here's to hoping QPV chai breakfast also lives on!

My office colleagues have made vital contributions to my life in the past few

years: Aurelien for his politically incorrect Mondays, James as a trusty partner for late night Imax showings, Irene for her wonderful cakes and ability to neutralise the office muskiness, Jizhong for his hothot and George the coffee machine for aiding me in converting caffeine into science. Romain, I will never forgive myself for missing the church. Friday Freakout skydive malfunction videos and Cocktail Fridays will be a tradition combo I will dearly miss.

Special mentions are given to Vinita and Aoife for allowing me to be the token scientist in their art public displays, Isaac for a) helping me to understand photoelectrochemistry and b) introducing me into the world of skydiving - the most addictive and expensive of all drugs known to man, Kinder for providing me with a constant source of Happy Hippos, the AMD group for allowing me to crash their barbecues and other social events, Nouf for appearing at Imperial with a cup of chai when I needed it the most as well as lending me her ninja Visio skills, Jin for distracting me from work by using me incessantly as an agony aunt, Arjun, Steffen and Ayaz for basic romantic getaways together and of course my family for their love, support and continued faith in me.

Abbreviations

ASTM	American Society of the International Association for Testing and Materials
BAPV	Building Applied Photovoltaic
BIPV	Building Integrated Photovoltaic
CC	Cosine Corrector
CCD	Charge-coupled Device
CIGS	Copper Indium Gallium Selenide
CLSC	Cylindrical Luminescent Solar Concentrator
CPV	Concentrator Photovoltaic
C. Vulgaris	Chlorella Vulgaris
DI	De-ionised
EPSRC	Engineering and Physical Sciences Research Council
EQE	External Quantum Efficiency
EROI	Energy Return on Investment
FLSC	Fibre Luminescent Solar Concentrator
FRET	Förster Resonant Energy Transfer
GA	Genetic Algorithm
IPA	Isopropanol
IPPC	Intergovernmental Panel on Climate Change
LED	Light Emitting Diode
LCA	Lifecycle Analysis
LSC	Luminescent Solar Concentrator
LSD	Luminescent Solar Diffuser
MOVPE	Metalorganic Vapour Phase Epitaxy
PAR	Photosynthetically Active Radiation
PBR	Photobioreactor
PEC	Photoelectrochemical Cell
PL	Photoluminescence
PLQY	Photoluminescent Quantum Yield
PMMA	Polymethyl Methacrylate
PV	Photovoltaic
QD	Quantum Dot
QMUL	Queen Mary University London
QW	Quantum Well
QWSC	Quantum Well Solar Cell
RAM	Random-Access Memory
SMARTS	Simple Model of Atmospheric Radiative Transfer of Sunshine
SQL	Structured Query Language
SUPSI	University of Applied Sciences and Arts of Southern Switzerland
TFLSC	Thin-film Luminescent Solar Concentrator
TIR	Total Internal Reflection

Contents

List of Figures

List of Tables

Chapter 1

Introduction

1.1 The Need for a Sustainable Future

The world's addiction to fossil fuels can be represented by the infographic of the estimated energy use in the U.S. in Figure 1.1. In 2011 80% of the energy used in the U.S. was fossil fuel-based [1]. Fossil fuel use has also continued to rise year on year with the fears of peak oil yet to materialise on the world stage. It is undeniable that fossil fuels give rise to anthropogenic climate change [2].

Humankind therefore has a triple-barrelled energy problem: Energy demands are ever increasing and have to be met whilst oil reserves are dwindling and atmospheric forcing by greenhouse gas emissions are causing significant and detrimental changes to the global ecosystem and environment. Despite the fact that the damage to a country due to climate change can cost around 3.5% of its GDP [3], the main obstacles to amending this issue in the past have been primarily social and political [4].

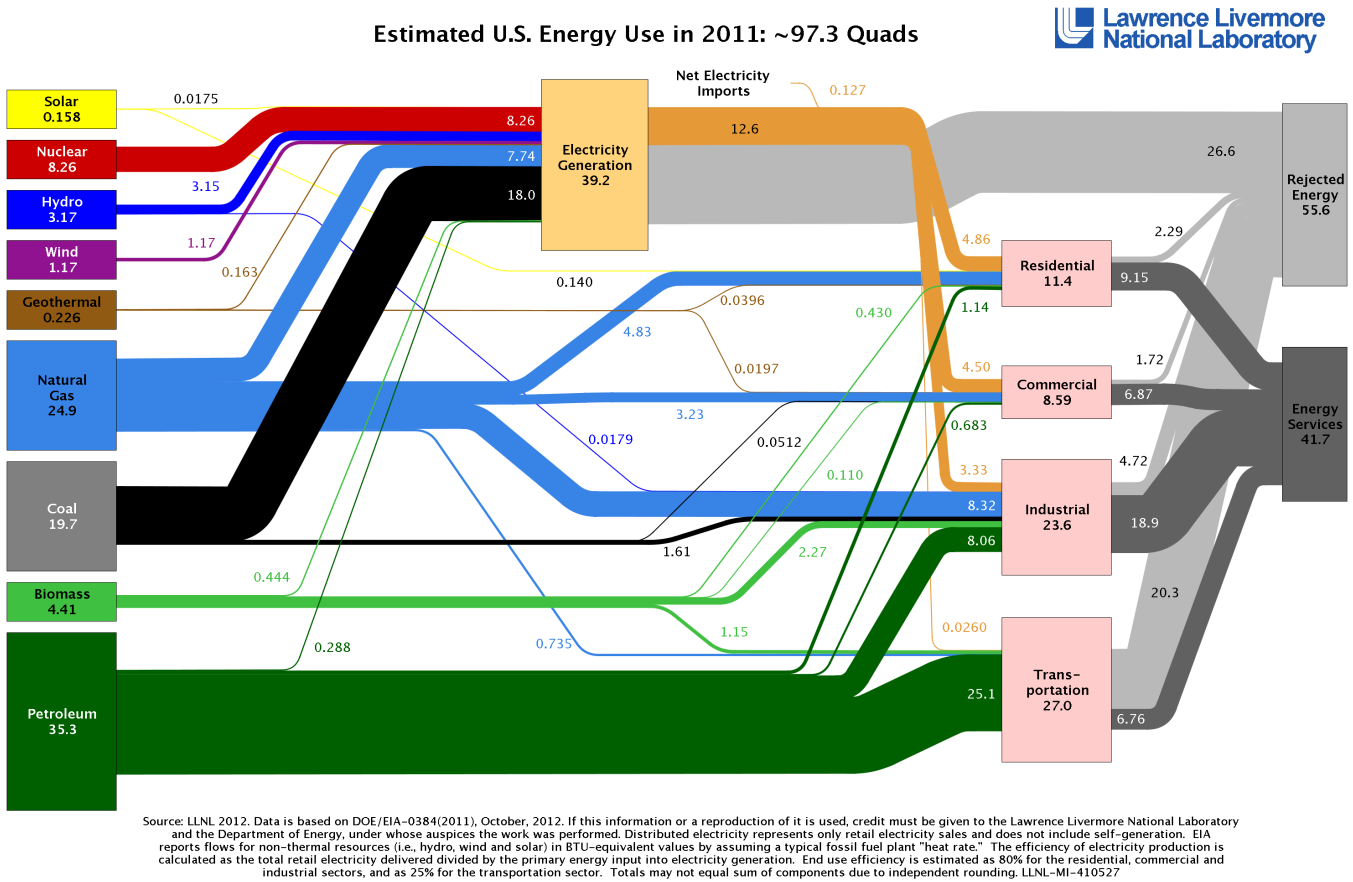

Figure 1.1: Infographic of the energy use in the U.S. in 2011, made by Lawrence Livermore National Laboratory. Fossil fuels take up 80% of the energy portfolio of the country [1]. This thesis aims to remove petroleum, coal and natural gas from the energy stream, and replace them with solar, biofuel and solar hydrogen energy streams. Infographic free to share via Wikimedia Commons.

Governments around the world however have started to react. The European Union (EU) formed a policy framework in January 2014 which outlines a target of reducing domestic greenhouse gas emission by 40% below the 1990 level by 2030 as a stepping stone to reaching an 80% emission reduction by 2050. Part of the policy included a further objective that also by 2030, at least 27% of the EU's energy consumption has to be renewable energy based [5]. The European Commission (EC) had already issued a directive in 2010 that by 2020 all new buildings have to be nearly zero-energy [6].

On a global scale, the 2015 UN Climate Change Conference in Paris has been seen to be a huge leap forward in global climate change policy, where a consensus between 196 nations was established on reducing anthropogenic causes of climate change and keeping global warming to within 2° C of pre-industrial temperatures. From this the Paris Agreement was created. On 22$^{\text{nd}}$ April 2016 175 nations put pen to paper and signed the agreement [7]. For all its pomp and circumstance, getting a consensus was the easy part. The much harder part of this lies ahead: The application of science, technology and lifestyle changes to curb CO_2 emissions and utilise all global resources sustainably. Looking at Figure 1.1, the energy streams from natural gas, coal and petroleum need to disappear, with the other streams increasing to take their places.

One of the many solutions that will play a part in curbing CO_2 emissions will be solar power. Sunlight is the ultimate sustainable energy source: abundant, free to harness, can be done so anywhere in the world, and whereas an oil spill causes ecological devastation, a sunlight spill causes families to have barbecues. The spectrum of sunlight is close to that of a black body at a temperature of 5800K, and at the top of the atmosphere delivers a power of 1366.1Wm^{-2}. Actual intensities on the surface of the Earth depend on the amount of atmosphere which sunlight has to pass through, as well as weather conditions. The atmosphere absorbs and

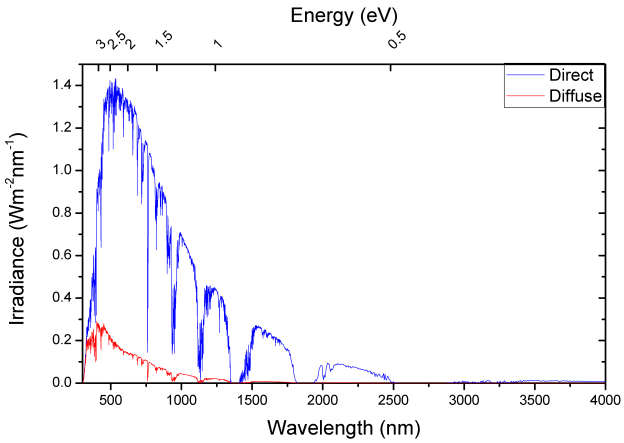

Figure 1.2: International standard light spectrum ASTM G-173-03 for direct and diffuse components of light. The integrated power defined as 1 sun is 1000 Wm^{-2}.

scatters part of the sunlight, giving rise to two types of light incident on Earth: direct planar light from the sun, and isotropic diffuse light from the atmosphere. The international standard light spectrum ASTM G-173-03 [8] is shown in Figure 1.2. The direct component from the sun contributes to 90% of incoming light and consists of the sun's blackbody spectrum minus the spectral regions absorbed by ozone and water. The diffuse light, more blue rich than direct light due to it being generated by Mie scattering in the atmosphere, contributes to 10% of incoming light. Together they have an integrated power of 1000 Wm^{-2}, a value defined as "1 sun".

Photovoltaic (PV) cells harness sunlight and convert it to electricity. The PV industry is rapidly growing, with global installed PV capacity reaching at least 227.1 GW at the end of 2015, which amounts to over 1% of the world's electricity generation capacity [9], and is being predicted to hit 321 GW by the end of 2016 [10].

With this current drive towards increasing building sustainability and zero net-energy policies, building integrated PV (BIPV) is a growing market [11], especially for countries where free space is at a premium. The potential for BIPV has been demonstrated by the fact that in around 1995, the growth rate of the PV global market started to increase more than ever due to greater interest in roof-top PV

[12]. Buildings can even turn from energy consumer, to energy producer [11]. BIPV is discussed in greater detail below in section 1.2.

An important characteristic of photovoltaics is their intermittency in ability to generate electricity, which complicates the assessment of their economic viability [13]. Furthermore the power output of a solar panel due to weather/day cycles is partly decoupled from public demand. For periods of high supply and low localised demand, especially for BIPV and building applied PV (BAPV), where solar panels are retrofitted onto conventional housing, the extra energy can either be stored or distributed further afield to areas of demand without supply [14]. Wind power also suffers more from intermittency than solar power, due to the inherent unpredictable fluctuating nature of wind speeds [15], so with the increase in wind and solar capacity, must also come an increase in energy storage or energy distribution capacity.

Currently, we globally only have capacity to store around 1% of the energy consumed. Conventional large scale energy storage is implemented almost entirely (98% globally) as pumped hydro [16]. Energy storage capacity will need to rise as we increase the number of photovoltaic and wind power stations. New pumped hydro projects however have increasingly high capital costs, and so currently endure difficulty in obtaining funding [17].

There is a plethora of next generation large scale energy storage technologies under investigation[18, 19], with the most likely contenders being: cutting edge battery technology such as metal-air; power-to-gas which revolves around electricity-powered hydrogen production and storage, or around methane which is 3-4 times more energy dense, but also more complex to produce, than hydrogen [20]; power-to-liquid which involves liquefying air by electrical means; and solar fuels, on which part of this thesis focusses on. All of these technologies have the capacity for rapid ramping up (or down) the rate of energy storage or generation [21].

The only current large scale commercial technology is compressed air. Barriers to its deployment appear in the form of difficulty in finding favourable locations that can accommodate gas turbine systems, as well as environmental issues due to the combustion of fossil fuels still being a necessity. Battery technology is still unsuitable for large scale energy storage due to high cost, as well as an inability to find a technology that is cheap, has long term performance lifetime, with high energy density and using abundant materials [22]. Thermal energy storage is used in hot countries, but current technologies in the form of molten salt suffer from issues such as cost, slow response times since phase change transformation can be involved, and a limited cycle life due to material thermal cycling resistance [23].

Battery manufacturing is taking off recently with the help of the rise of electric vehicles, but this technology is far from being suitable for air transport, with the main issue being insufficient energy densities in energy storage, alongside suitably powerful electrical propulsion. The energy density is around 42MJ/kg for Jet A-1 fuel [24] and around 0.54MJ/kg for state-of-the-art, as yet uncommercialised lithium ion batteries [25]. For this reason hydrocarbon fuels for the foreseeable future will continue to be necessary for air and marine transport.

Solar fuels in the form of solar hydrogen and biofuels provide solutions for both large scale energy storage to mitigate intermittancy, and sustainable fuels for transport. It has been stated that the "Holy Grail" of solar energy storage is to use a semiconductor as both a light absorber and energy converter in photo-assisted water splitting, also known as photoelectrolysis, to store solar energy as hydrogen [26]. A detailed discussion of photoelectrochemistry is beyond the scope of this thesis, and a thorough background of the area can be found elsewhere [26, 27, 28, 29]. Renewable, carbon neutral transport fuels are needed for carbon reduction in this infrastructure sector. Biologically produced fuels, or biofuels, can be

a solution to this because the biomass absorbs atmospheric CO_2 in order to grow, raising the possibility of a carbon neutral fuel [30]. Not only does liquid biofuel allow solar energy to be stored, it can also be used directly in existing combustion engines and transport infrastructure. Green fuels which can be directly inserted into existing infrastructure and technology whilst proviinge a means of removing the natural gas, coal and petroleum streams in Figure 1.1 are called "drop-in fuels".

This thesis is aimed at the idea of reducing the fossil fuel energy streams by augmenting the contribution of renewable energy sources to help solve the triple-barelled energy problem. It aims to improve knowledge on three topics of sustainable energy as discussed above: BIPV, and energy storage and sustainable fuels in the form of solar hydrogen and biofuels.

1.2 Building Integrated Photovoltaics

Building integrated photovoltaics (BIPV) are photovoltaics that replace conventional building materials, that are considered as functional part of a building's structure, or are architecturally integrated into a building's design [12, 31, 32, 33]. They are often used in sustainable building initiatives, with solar panels being placed on tops of houses as well as non-residential buildings such as offices and schools [34]. BIPV is also considered one of four key factors of cost reduction, efficiency increase, building integration and storage capability, to ensure the success of the PV industry [35].

BIPV systems provide opportunity for architectural design and can be used purely for aesthetics. They can act as shading devices [12] and also form semi-transparent forms of fenestration [36]. Silicon cells can be used to make a BIPV roof look similar to a conventional roof, or as part of a glass ceiling to provide shading [12, 37].

It has been stated however through a review of papers on life cycle analysis (LCA) of BIPV that most studies do not have comprehensive life cycle and impact coverage of such systems, often omitting crucial factors such as end-of-life disposal [40]. As a response, thorough methodologies for life cycle cost assessments have been proposed [41].

There are also barriers hindering the rise of BIPV. These barriers can be classified into four main groups: institutional, public, economic and technical [42]. For institutional barriers, governments are critically responsible to prepare supportive laws, policies and financial aids such as feed-in tariffs to aid BIPV. Feed-in tariffs especially, are one of the most, if not the most, important factor in a BIPV project [43]. This in turn would provide a drive to improve cost:efficiency ratios of BIPV, a major economic and technical barrier. Other technical barriers exist, such as non-optimal angling of a photovoltaic, if for example it becomes a building façade, and the performance drop caused by it. Lastly, the success of a BIPV project depends on the public's cooperation to support such an technical endeavour. Indeed, it has been shown that public knowledge on the subject is vital to achieve social acceptance, something which requires more effort than is expected [42].

A recent UK poll carried out by Solarcentury, a leading PV provider and installer, confirmed the importance of public opinion on BIPV with 86% of homeowners wanted new home additions to "look stylish" whilst 65% said if they installed solar panels, they would have to be less visible and not stand out [44]. Public buildings however have potential for interesting aesthetics in order to stand out. This has already been demonstrated by luminescent coloured façades on the Musac museum in Léon, Spain and the Palais des Congrès in Montreal, Canada, as shown in Figure 1.3.

Unconventional PV can be used to try and overcome some of these BIPV bar-

(a) The Musac Museum, in Léon Spain.

(b) The Palais des Congrès, in Montreal Canada.

Figure 1.3: Two buildings with coloured façades. (a) Taken by tagago [45], licensed under CC0 1.0. (b) Taken by Emmanuel Milou [46], licensed under CC BY-SA 2.0.

riers whilst integrating some of the aesthetic aspects demonstrated in the colourful buildings. Perovskite solar cells, which are solution-based, semi-transparent thin-film PVs, form the basis of new solar cell company OxfordPV [47]. This company claims high efficiency, low cost solar power, yet successful commercialisation or even a large scale showcase of this technology has yet to be demonstrated. Another type of high efficiency, low cost PV in the form of dye-sensitised solar cells have been demonstrated practically to work in the real world, with the EPFL convention centre having a dye-sensitised solar cell coloured façade since 2013 [48].

This is where luminescent solar concentrators (LSCs) can be used as an alternative to current technologies that are not fully testing. LSCs can be made of different colours, are cheap to produce and the amount of conventional PV needed to couple with the LSCs is much less than the whole façade surface area.

1.2.1 Luminescent solar concentrators and their potential for BIPV

The concept of the luminescent solar concentrator (LSC) was conceived in the 1970s [49, 50, 51, 52] as a practical way to reduce the cost of solar energy. This was an attractive idea on two fronts, the first being the ability to convert roughly similar electrical output with a reduced solar cell area, and secondly the ability to

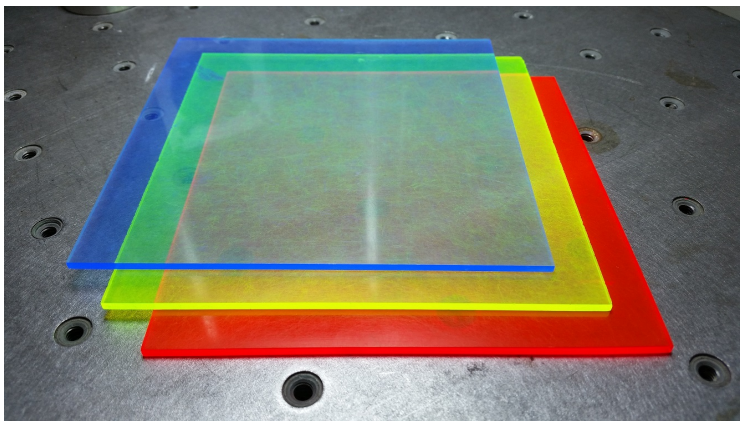

Figure 1.4: A collection of luminescent solar concentrators under illumination. The emission wavelength can be changed by way of using different luminescent material.

collect sunlight from all angles, thereby taking away the necessity for solar tracking as is needed for conventional concentrating setups [53].

In its most basic form, the LSC consists of a transparent waveguide homogeneously doped with, or coated with, luminescent material. Luminescence is the spontaneous emission of light not caused by the heating of a material, but rather from an electronically excited material [54]. This can be caused by light absorption, chemical reactions or electrically biasing the material. In the case of the LSC, the luminescent material absorbs incident solar light and re-emits it, with a proportion of the re-emitted light trapped within the transparent medium due to total internal reflection (TIR), thereby guiding it to the edge of the LSC. The light is then collected optically by a PV cell, usually optically matched onto the edge using refractive index-matching liquid. One advantage of using an LSC is that the emission spectrum of the luminescent light can be manipulated, by way of changing the luminescent material (see Figure 1.4), so that the peak emission wavelength matches the peak absorption wavelength of the PV cell in use.

After an initial flurry of research activity, interest waned in the 1980s with a combination of limitations with luminescent materials [55], the increasing interest in silicon, and decreasing oil prices [56]. Rather a lot of interest has been picking

up in the past decade [53] due to new global renewable energy policy, as well as a renewed desire for BIPV. LSCs at a module scale cannot compete with standard silicon PV modules in terms of absolute power or standard installation costs [57], but for BIPV applications, LSCs do not directly compete with cheap photovoltaics as they can be incorporated into buildings or other structures in variety of designs and colours [58]. This can satiate the needs for both the public's desire for aesthetically pleasing yet hidden photovoltaic energy generation and the architectural desire for eye-catching building designs and net zero-carbon capabilities.

Whilst being outperformed in absolute terms by PV in module scale, they have a few positive characteristics. LSCs are less adversely affected by lowered light intensity levels, and the relative efficiency of an LSC can actually increase in diffuse light conditions, due to more favourable incident light absorption spectra [59]. An LSC has also been demonstrated to perform closer to its standard test conditions in real life than standard silicon PV modules. Using a performance ratio figure of merit which measures the deviation between the actual performance of a PV module and that which is theoretically achievable working at standard test conditions (STC), Aste *et al.* found that the power generated by an LSC relative to the solar irradiance is 20-40% closer on sunny days and 30-45% closer on cloudy days to its STC power output than standard polycrystalline and monocrystalline PV modules [57].

The LSC in question, which was homogeneously doped with a 2-dye yellow luminescent mixture, was used as a south-facing window in an office and LSC integration into windows was determined to be compatible, and even advantageous, in terms of of visual comfort. A similar study using a LSC with red luminescence quantified maximal visual comfort to be when the LSC made up 25% of a window [60]. Emulating the aesthetics of the two buildings in Figure 1.3, 3D raytrace modelling has been undertaken on LSC stained-glass window designs. Raytrace simulation

results for multi-coloured LSC "stained glasses" were found on average to agree to within 5% of the experimental results, thus paving the way for raytrace modelling to be used as an effective tool to determine LSC windows in a BIPV setting [61]. A year later in 2015, ray-tracing was again used by Grée *et al.* [62] to determine appropriate values for thickness and dye concentration of a roof-tile LSC design. The authors wrote in their paper conclusion that results from this raytrace experiment were going to be used for an real world roof-tile LSC experiment. Results from this practical experiment have yet to be published.

LSCs have been used as part of luminescent lighting devices in a concept known as daylighting [63, 64, 65]. This concept is where incident light is collected by a LSC building's roof, and the luminescent light is waveguided into a room in a building. It has been measured that a 1.44m^2 fibre LSC array, when illuminated at 1 sun, illuminates a room at around 60Wm^{-2} [66]. The same authors go on to say that the intensity output could have been higher had larger fibre diameters been used [67].

Not only can LSCs be used for buildings alone, but they can provide aesthetic and electricity generating aspects to other structures like sound barriers on motorways, atrium panels [53] and curved LSCs even be wrapped around lamp posts [68].

1.2.2 Thesis motivation - Cylindrical LSC arrays

All LSC investigations that are focussed on building integration utilise planar geometries, with the exception of the cylindrical LSC array used for daylighting [66, 67], or the flexible planar LSC investigated at different bend curvatures [68]. These cylindrical arrays were not compared with planar LSCs of equal dimensions. Cylindrical geometries are being investigated because of their increased ratio of incident light collection area to luminescent emission area, albeit as standalone devices. Cylindrical LSCs would be implemented in the real world as arrays, however

Edelenbosch *et al.* [69] are the only authors to publish on the optical effects of having cylinders as arrays. This work focussed on the middle cylinder out of five being illuminated by incident light at normal incidence, and understanding its light recycling processes.

There is an absence of knowledge of how a large scale cylindrical array would work in real world conditions, where incident light is only normal to the array at one point during a day. One of the thesis objectives was to therefore investigate the optical behaviour of neighbouring cylinders at realistic angles of incidence. As a result, incident light trapping effects which are not seen in planar LSC geometries were found. This encourages the investigation of cylindrical array tilt optimisation to take advantage of this light trapping.

Whislt one can optimise BIPV for better integrated solar electricity generation, it still does not take away the current issue of the intermittency of solar power generation. Energy storage technologies are needed to fill the gaps for when the sun is not shining. The following section introduces using solar hydrogen as a renewable form of energy storage.

1.3 Renewable Hydrogen as a Solar Fuel

Renewable hydrogen was introduced in section 1.1 as a solution for energy storage to deal with both renewable intermittency issues, and for transport. Surplus electricity generated by renewable sources can be used by an electrolyser to split water into hydrogen and oxygen, and storing the hydrogen as a fuel. This hydrogen can then be used by a fuel cell either during times of high electricity demand and low renewable supply [70], or in a vehicle [71]. The combustion of hydrogen yields only water, and so alongside electric vehicles, is seen as an attractive fuel especially in urban areas due to the absence of toxic substances such as carbon dioxide, nitrogen oxides and sulphur oxides [70].

Hydrogen however is already used in great quantities around the world, with a desperate need for a more sustainable form of production. Most of the hydrogen produced in the world today is currently used for ammonia production in the fertilizer industry and in oil refineries at the rate of 400-500 billion Nm^3/year (N relates to "normal" conditions of standard temperature and pressure) , and of this, 99% of it is produced from fossil fuels and natural gas [70]. Whilst sustainable hydrogen production still has unavoidable pollution due to infrastructure development and precious metals involved in building the reactors, it is still less polluting even in small-scale production compared to fossil fuel produced hydrogen [71].

Hydrogen can be produced sustainably in a few ways. Conventional electrolysis can be driven by renewable energy sources such as PV and wind. It can be produced via fermentation of biomass as well as a form of excretion by certain cyanobacteria [72]. Solar hydrogen can be produced by water splitting, either by high-temperature processes [73], or by photoelectrochemical means [74].

1.3.1 Solar hydrogen by photoelectrochemical means

There is great attention in hydrogen production through photoelectrochemical means. First demonstrated by Fujishima and Honda in 1972 [75], it uses incident sunlight to generate charge carriers that can split water photocatalytically at specialised semiconductor interfaces.

The premise of photo-water splitting is to use sunlight to transfer excited charge carriers from a conductive electrode into water at a larger potential bias than the potential to split water into gaseous hydrogen and oxygen. Sufficient potential difference is applied across the water in order to drive two half-reactions happening on two electrodes [76]:

$$2H_2O(l) \rightleftharpoons O_2(g) + 4H^+ + 4e^- \tag{1.1}$$

$$4H^+ + 4e^- \rightleftharpoons 2H_2(g) \tag{1.2}$$

Equation 1.1 is the oxidation reaction happening on the anode (+), whilst Equation 1.2 is the reduction reaction happening on the cathode (-). In electronic (semi)conductors, charge carriers are electrons and holes. In water however, the charge carriers are ionic species such as H_3^+O and OH^- as there are no free electrons in solution. The free energy needed to split water into hydrogen and oxygen corresponds to a minimum semiconductor bandgap of 1.23 eV. In reality, a larger bandgap of at least 1.9eV is needed [77] due to losses associated with charge carrier separation, charge transport and photocatalytic efficiency [78].

A photoelectrochemical device has an anode and a cathode in contact with an electrolyte. The anode's valence band edge must be lower than the oxidation energy level of the electrolyte, and the cathode's conduction band edge must be higher than the reduction energy level of the electrolyte. This is shown in Figure 1.5. When a semiconductor comes into contact with an electrolyte, Fermi levels equilibrate leading to band bending and the creation of a space charge region. Upon illumination of the semiconductor, electron-hole pairs are created and the Fermi level increases with the internal photovoltage ΔV_{photo}. As stated above, several loss mechanisms then decrease the voltage to an externally measured photovoltage.

Having no free electrons for charge transfer, water is limited by mass transfer of ionic species produced at the electrodes. As such, many reactor systems operate with a pH bias with acid or alkaline solutions. For example, adding sodium hydroxide ($NaOH$) to water causes it to dissociate into mobile ions Na^+ and OH^-. Having free mobile charge carriers causes the water mixture, or electrolyte, to become more conductive. When using an alkaline electrolyte, with pH levels higher

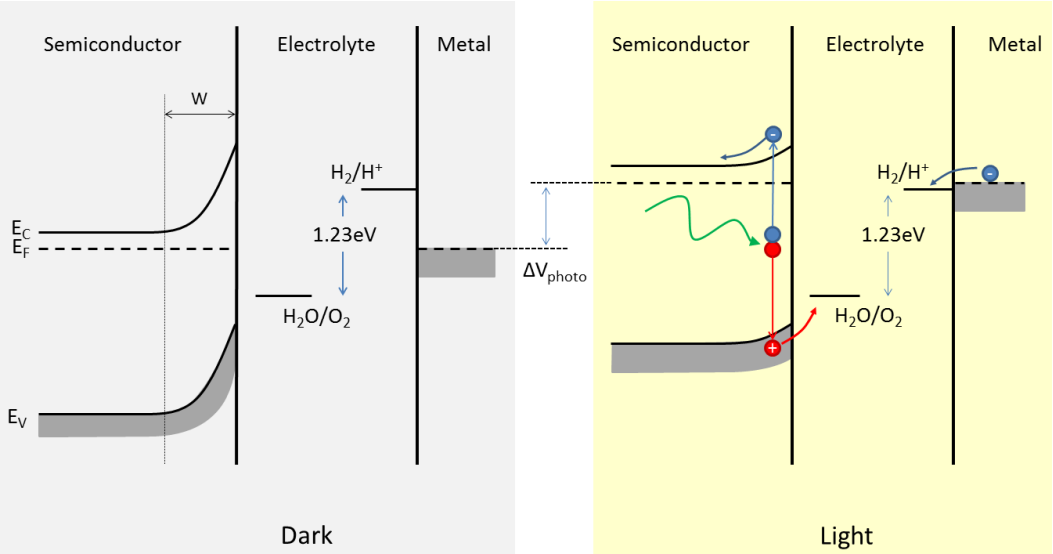

Figure 1.5: Band diagram for a PEC cell where an n-type semiconductor anode and a metallic cathode are used in an electrolyte, in dark conditions (left) and in illuminated conditions (right). The space charge region for charge carriers is depicted as W. Illumination raises the Fermi level by an internal photovoltage ΔV_{photo} and creates electron-hole pairs. Holes and electrons enter the electrolyte for oxidation and reduction respectively.

than neutral (7), equations synonymous to equations 1.1 and 1.2 can be expressed using OH^- ions for oxidation and reduction half reactions [77]:

$$4OH^- + 4h^+ \rightleftharpoons O_2 + 2H_2O \tag{1.3}$$

$$4H_2O + 4e^- \rightleftharpoons 2H_2 + 4OH^- \tag{1.4}$$

where the self-ionization of water can be expressed as:

$$H_2O \rightleftharpoons OH^- + H^+ \tag{1.5}$$

1.3.1.1 Reactor designs

Traditionally speaking there are two designs for water splitting reactors. One involves using conventional PV to power conventional electroylsis reactors, called PV-electrolysers [79]. The other involves a PV or other photo-active structure embedded within the reactor and encapsulated against the water using transparent,

conductive and chemically robust materials. These are called photoelectrochemical (PEC) cells, or more glamorously by some, artificial leaves [80, 81]. These are traditionally monolithic structures, meaning they are front-illuminated with one side of the cell directly contacted with the water, whilst the other end is not in contact with the water but instead linked to a counter electrode. Both designs are shown pictorially in Figure 1.6.

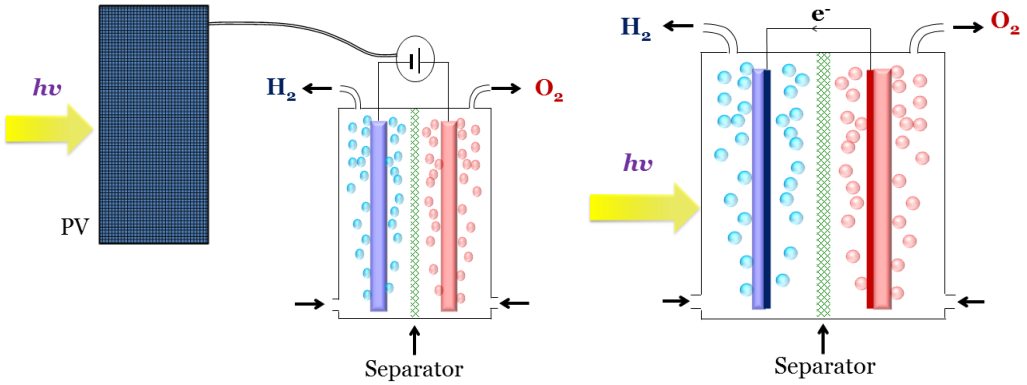

(a) PV electrolyser setup.

(b) Photoelectrochemical (PEC) cell setup.

Figure 1.6: Water splitting with a PV electrolyser (a) and a photoelectrochemical (PEC) cell (b). The PV electrolyser system uses conventional PV to power conventional electrolysis for water splitting. The PEC cell has an integrated photoactive device within the reactor itself. In the case of the reactor in (b), the cathode (coloured blue) has the embedded PV which provides the potential bias to split water.

For single semiconductor devices, not only do they have to have large bandgaps, but their band edges must be suitably matched to the reduction and oxidation potential of water. Several photoabsorbers could also be connected in series to increase the potential bias between the anode and the cathode, but the photocurrent density decreases by a factor equal to the number of connected cells [82]. There is therefore a distinct move into using 2- and 3- junction solar devices to power PEC water splitting, and the most efficient systems are PV-electrolyser types [76]. Some integrated 3-junction PEC designs are reaching solar-to-hydrogen efficiencies of 14%, a number more closely matching that of PV-electrolysers [83].

PV-electrolyser systems have been called "brute force" approaches due to the simple requirement of applying enough voltage to split water. Benefits include the ability to independently optimise the photovoltaic and photoelectrochemical technologies, and the problems related with photo-corrosion of semiconductors and blocking of light sensitive surfaces with hydrogen-evolving or oxygen-evolving catalyst materials are automatically avoided. PEC systems however are considered to be the brighter future prospect as they are more practical, efficient and cheaper methods of hydrogen production because they integrate both light energy collection and water splitting into one device [84]. It has been argued that both designs are one and the same electrochemically, with the only difference being the engineering decision of where to place the photo-active devices [78]. The same authors that claim this have a device design which is halfway between the two conventional approaches, where an encapsulated photovoltaic cell is placed inside the solution, but the half-reactions for water splitting occur on two electrodes that protrude behind the cell [82]. These authors claims are correct only for device designs where the electrode surfaces are not photo-active.

A technological frontier, concentrating optics have been investigated for PV-electrolyser systems. This is where conventional CPV is utilised to power electrolysis [85, 86]. This includes a system with the highest solar to hydrogen conversion efficiency record to date of 24.4% [87]. There is also a hybrid concentrator PV-electrolyser/PEC system, whereby spectrum splitting occurs to light a PEC cell and solar cell simultaneously. The solar cell is used to provide further bias to the reactor as well as power to other auxiliary equipment [88, 89]. A computational paper [90] has been published on the effects of yearly irradiance and temperature variation effects on concentrated PEC reactors to bring into focus real-world deployment strategies for PEC technology. Results showed that annual weighted average solar-to-hydrogen efficiencies in excess of 9 to 11% can be achieved in cloudy and

sunny locations respectively. The PEC reactors, however, were deemed likely to incur damage due to both overheating and freezing without modifications for module cooling and the antifreeze adaptations to the electrolyte respectively.

Efficiency is only one of the pillars of the water splitting trilemma: Efficiency, robustness and economic viability. Currently most water splitting designs use platinum as one of the electrodes. This material is used conventionally for traditional electrolysis, but for the scale of hydrogen production envisioned by the solar hydrogen community, it is too expensive to be scalable. Of all the citations in this section thus far, only Elias *et al.* utilise non-platinum materials on both their electrodes, using instead RuO_2 and NiMoZn on steel for the anode and cathode respectively [79]. A complete list of all reactors and their respective electrode materials can be found in the Ager *et al.* 2015 review [76]. Ahmad *et al.* produced a review that focusses on TiO_2, one of the most commonly used photocatalysts [91], and work done to mitigate its issues of needing a large potential to drive hydrogen, limited light absorption due to its large bandgap of 1.9 - 2.1eV, and rapid charge carrier recombination rates [74]. A comprehensive material benchmarking study was conducted by McCrory *et al.* to investigate the performance of materials at current densities relevant to a 10% efficient water splitting system under 1 sun illumination at both 1 M NaOH and 1 M H_2SO_4 solutions. Results suggest there is a need to develop non-noble metal oxygen evolving catalysts stable in acidic conditions, and most hydrogen evolving catalysts used in the community show high activity and stability in both acidic and alkaline conditions [92].

1.3.2 Thesis motivation - A new double-illuminated PEC reactor design

All PEC reactors in the literature are designed such that they are illuminated from one surface. Whilst most designs involve one electrode to be photo-active [93], some monolithic designs require both electrodes to be photo-active, where the top

photoelectrode is designed to be semi-transparent so that the bottom photoelectrode receives sufficient light [94]. This brings difficulties with the trade-off between photoelectrode performance and light attenuation through the device structure. [95].

chapter 5 covers a novel reactor, designed by Dr. Anna Hankin, in which each photo-electrode is illuminated independently from two light streams on either side, reducing the need for compromise on semiconductor performance and transparency. Since the reactor windows are normal to incidence sunlight, optical devices are needed to direct light from the sun into the photoelectrodes. This introduces opportunities for interesting waveguide designs and light concentration. The simplest optics would be a mirror to direct incident light into reactor. A schematic is shown in Figure 1.7.

The photo-anode material used is hematite, a variation of iron oxide ($\alpha - Fe_2O_3$). It is cheap, abundant and stable in a wide range of PEC environmental conditions[96]. Due to having a band gap of 1.9eV - 2.2eV, it is able to capture around 30% of incident solar energy [97]. For these reasons it has been extensively researched. Hematite is not able to spontaneously split water upon illumination as its conduction band edge lies at a lower energy level required for the hydrogen evolution side of the water splitting reaction [96], and so to operate requires either electrical potential biasing [98], or to be used in tandem with a second semiconductor as the other electrode with the correct band edges to complement it.

Being in a standalone PEC reactor, the photo-cathode must be able to provide the potential bias to the hematite photo-anode. The most straightforward solution is to use a solar cell as part of the photo-cathode. It must also be chemically stable in PEC environmental conditions. This can be ensured by coating it in a protective photocatalytically active layer. Anatase titanium dioxide (TiO_2) is the encapsulant of choice due to its conduction band edge being higher than the energy level required

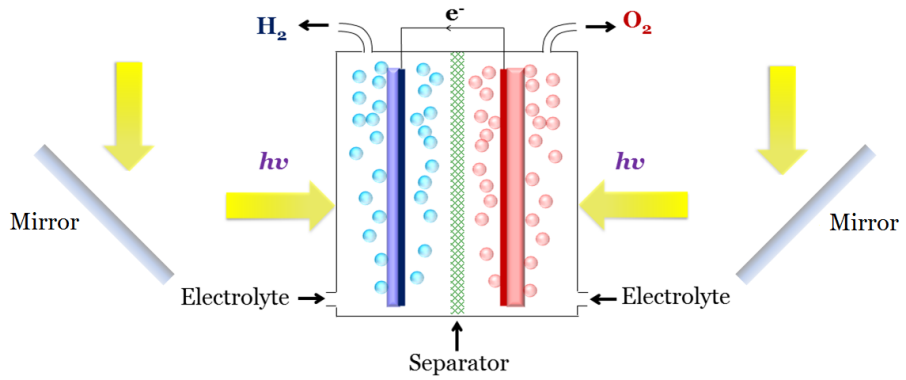

Figure 1.7: The double-illuminated PEC reactor. Both electrodes are photo-active.

to complete the hydrogen-forming half reaction, and is chemically stable[77]. It has also been extensively researched, being one of the most well-known photo-catalysts of the past forty years [74]. Initial attempts were made to use TiO_2 coated CIGS solar cells, but they did not provide enough bias to drive water splitting reactions.

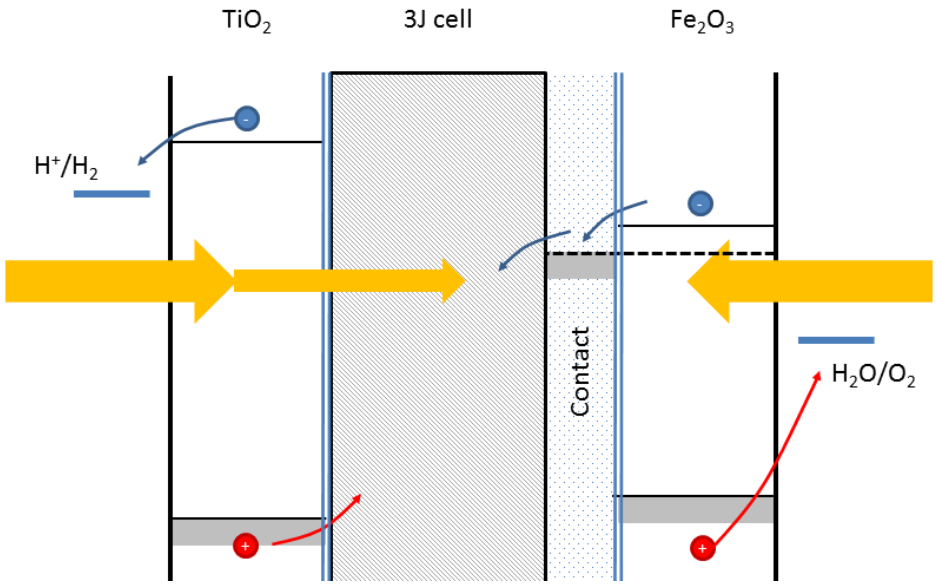

Figure 1.8: A simplified band diagram of the PEC reactor. TiO_2 is coated on an IQE-manufactured triple junction cell as a photo-cathode. It is contacted to a hematite (Fe_2O_3) photo-anode.

Standard triple junction solar cells from IQE [99] were then chosen as the photo-cathode base in order to provide more potential bias to the hematite. A simple band diagram of the PEC reactor is shown in Figure 1.8. The IQE cells used are stan-

dard InGap/GaAs/Ge n-on-p solar cells. Exact specifications are proprietary and therefore unknown. They were received processed, with fully metallised front and back contacts and an anti-reflection coating. Yahya al-Saleh of Imperial College's Quantum Photovoltaics Group performed TiO_2 coating by sputtering.

1.3.2.1 Novel optics for the double-illuminated PEC reactor

The two photo-electrodes are positioned back-to-back, facing opposite directions. They are both in their own compartments with their own optical windows to receive light. The outer case has a slot, in which the waveguide will be inserted. A Solidworks reference diagram of the PEC reactor with and without a waveguide is shown in Figure 1.9. The waveguide is the optical base which can be used either as secondary light trapping with a Fresnel lens/cone setup, or as an LSC. The design of the reactor means that the system is modular, with an array of reactors able to connect up to either end of a waveguide.

The benefit of this optical system is its flexibility in design according to the photo-electrodes' needs. The optics can directly (via lens concentration) or passively (via luminescent concentration) concentrate light into the reactor. Different luminescent dyes can be used to dope the waveguide so that the LSC emission wavelength is matched to the peak absorption wavelength of the photo-electrode.

The prototype for this design uses one PEC reactor, and two waveguides on either side. Because a triple junction cell is used as a photo-cathode, it requires full spectrum illumination. This removes the possibility of using a waveguide as a LSC. chapter 5 discusses a waveguide whereby a reflecting cone is embedded into its centre, and is illuminated by concentrated light by way of a Fresnel lens. The cone reflects this concentrated light into the waveguide.

A secondary investigation is undertaken whereby the reflective cone is replaced

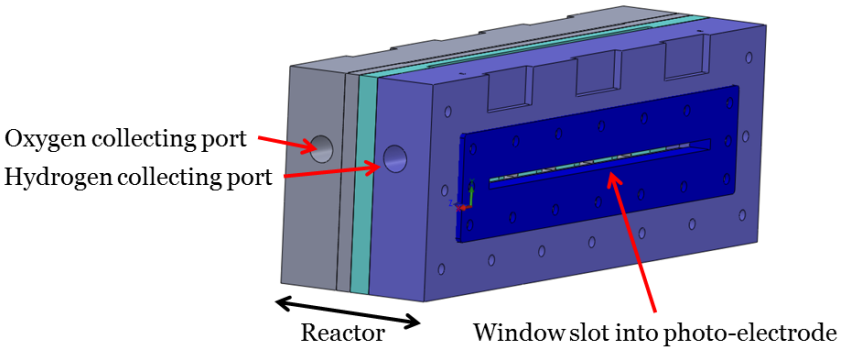

(a)

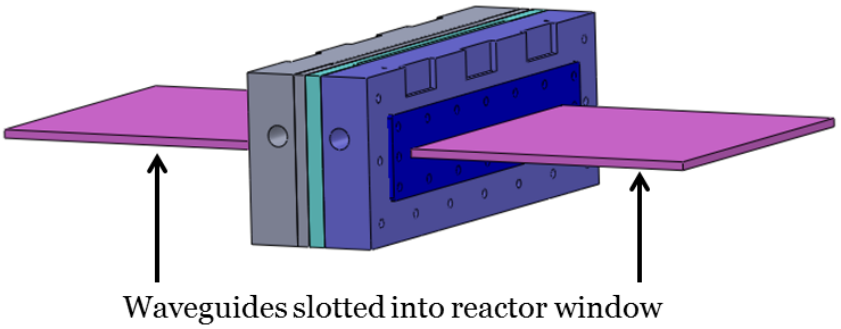

(b)

Figure 1.9: The PEC reactor with the optical window slot exposed (a), and with the waveguides inserted into them (b).

with a quantum well solar cell, which could be used a luminescent centre.

1.3.2.2 The quantum well solar cell as a luminescent centre for simultaneous electricity/hydrogen production

Quantum well solar cells (QWSCs), first invented by Barnham and Duggan [100], offer an way to improve multi-junction solar cells by various factors. Firstly the bandgap of the QWSC can be tuned by changing the dimensions of the quantum well. Secondly, at illumination intensities greater than 200 suns, electron / electron-hole recombination is dominated by radiative processes [101, 102, 103]. In essence, at high concentration, QWSCs can be viewed as luminescent devices. Indeed Lee *et al.* discuss using this recombination-generated light to recycle light back into the solar cells to reduce spectral sensitivity in a solar cell [102].

A QWSC has the ability to behave like a LSC because the photoluminescence (PL) wavelength is below that of the bulk material bandgap of the solar cell, as shown by the external quantum efficiency of a QWSC in Figure 1.10. This is due to the PL wavelength being determined by the QW bandgap, which is lower than the bulk solar cell bandgap, as shown in Figure 1.11. The absorption of PL comes mostly from intrinsic absorption due to free carriers in a doped substrate [104]. This can be remedied by either using a semi-insulating undoped substrate, where free carrier absorption is diminished, or by removing the substrate completely [105]. This ability to behave like a LSC can be unsurprising considering the similarities in basic semiconductor structure between a QWSC and a QW laser diode, which is designed for maximal luminescence output [106, 107].

A QWSC luminesces even when generating electricity. It operates at high concentration, and so works under concentrating optics which only work with direct light. Therefore under conventional concentrating PV operation, the diffuse component of light and the photoluminescence emitted by the QWSC are two un-utilised photon streams. If a QWSC were to be embedded within a waveguide (pictured in Figure 1.12), and the waveguide top surface coated with a luminescent layer that would absorb diffuse light, these two waste photon streams could be harnessed to power a PEC reactor. This setup would generate electricity from the QWSC, and hydrogen from the reactor powered by the QWSC PL and diffuse light.

Both photon streams must be of equal intensity in order for the PEC reactor to function. It is unknown, however, whether the intensity of PL emitted by a QWSC is comparable to that of a waveguide coated in luminescent material. This is investigated in section 5.2.

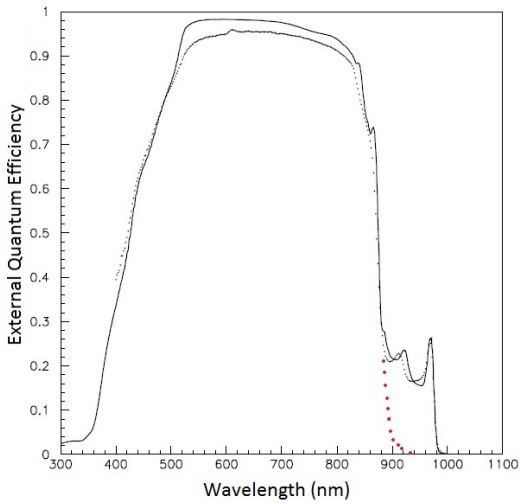

Figure 1.10: Measured and fitted external quantum efficiency (EQE) of strain-balanced quantum well solar cell QT1604, a 22 InGaAs/GaAsP quantum well solar cell. The full structure is shown in Appendix D. The red dotted profile corresponds to what the EQE would look like if the solar cell had no quantum wells (QWs). The QWs extend the quantum efficiency due to having a smaller bandgap, as shown in Figure 1.11.

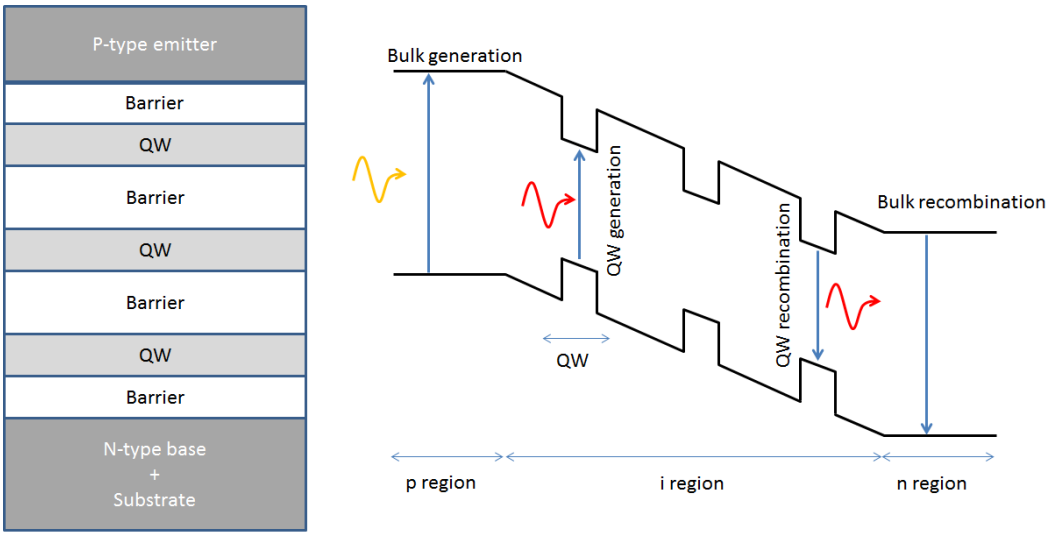

Figure 1.11: Structure of a quantum well solar cell (QWSC) on the right, and its respective band diagram on the left, showing the respective radiative processes of the structure. The QW bandgap is smaller than that of the bulk, giving rising to an extended quantum efficiency range into the infra-red. The photoluminescence peak wavelength of a QWSC corresponds to the QW bandgap.

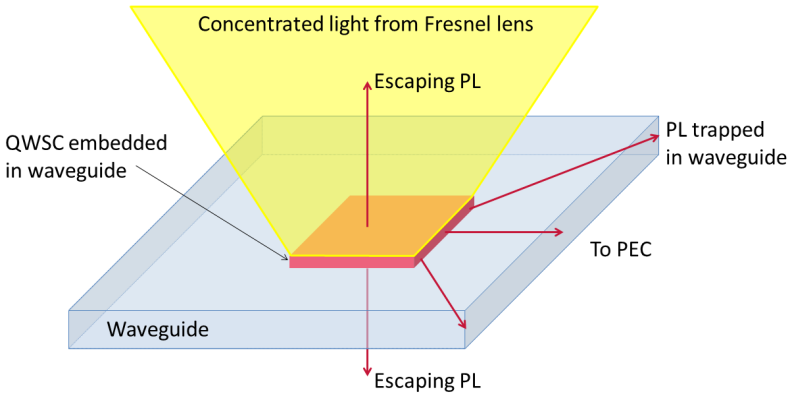

Figure 1.12: A quantum well solar cell is embedded within a waveguide. It is illuminated under concentration and generates electricity. It also photoluminescences due to radiative recombination dominating non-radiative recombination. Some of the photoluminescence, which is emitted at all angles, can be trapped within a waveguide by total internal reflection and guided towards the edge which is coupled onto a PEC reactor.

1.4 Biofuels as a Solar Fuel

The previous section discusses hydrogen as a form of solar fuel, both as a form of energy storage and as a fuel for applications such as electric vehicles. Biofuels provide another option for sustainable fuels and energy storage in the form of hydrocarbon fuel derived by organic means.

Biofuels took up a 2% share of transport fuels globally in 2010 [108]. The most widely available forms of biofuel are in the form of bioethanol, manufactured from sources such as corn starch, sugar cane or sugar beet, or in the form of biodiesel, manufactured from sources like palm and oilseed rape [109]. All of these sources are defined as first generation sources. There are multiple generations of biofuels [110, 111]:

- 1st generation: Biofuels made by converting food crops grown on prime cropland into biodiesel or ethanol. This means using corn for ethanol, and vegetable oil and animal fats for biodiesel.

- 2nd generation: Biomass grown on marginal croplands unsuitable for food production, or using non-food crops and residues, where the biomass is consumed in production. Cellulosic ethanol technology fits in here as do non-food crop technologies such as jatropha plant based biofuel. Biomass used in 2nd generation fuels can be sawdust, residues from paper manufacturing, municipal waste, jatropha, camelina and switchgrass.

- 3rd generation: Biomass grown on non-arable land, based on integrated technologies that produce a feedstock as well as a fuel, and require the destruction of biomass. For this, algae and cyanobacteria are used.

- 4th generation: Like 3rd generation biomass, except biofuel extraction does not require biomass destruction. Algae and cyanobacteria are used.

Large scale production of first-generation biofuels introduce issues into sustainability and commercial viability. First and foremost, these crops compete directly with food crops for land and water, and in the case of Brazil's sugarcane, competing with rainforest. As an example, in 2014 the UK used an estimated 22billion litres of diesel [112]. If this supply was met purely from oilseed rape sources [113], of which biofuel yields are 1,560 L/ha/yr (see Table 1.1) and taking into account that the energy equivalent of biodiesel is around 93% of conventional diesel [109], 15.2 Mhectares would be needed, over half the land area of the UK (24.25 Mhectare). If however algae is used as the biofuel source, only 0.8 - 3.3 Mhectares would be needed. Secondly, the overall savings in energy and greenhouse gas emissions are not particularly high in 1st generation biofuels, an example being that the input of energy required to make biodiesel from oilseed rape and soya is around 50% of the energy contained in the biofuel itself [109].

Biofuel Type	Crop	Biofuel Yield (L/ha/yr)
Bioethanol	Corn	3,800
	Sugarcane	7,200
	Sugar beet	7,900
	Wheat	1,700
	Cassava	137
Biodiesel	Rapeseed	1,560
	Soybean	600
	Canola	1190
	Oil palm	4,200
	Jatropha	1,892 - 2,700
	Algae (C. Vulgaris)	8,200
	Algae (Nannochloropsis)	23,000-34,000
	Microalgae (unspecified) [114]	60,000 - 240,000

Table 1.1: A comparison of biofuel yields in units of litres/hectare/year from biomass feedstocks, with values compiled from various sources [109, 115, 116, 117, 118]. For the algae, the yields are estimates based on laboratory experiments [119] and of pilot scale trials [120].

1.4.1 Algae Biofuel

Algae and cyanobacteria are photosynthetic aquatic organisms. Algae are prokaryotic, meaning they do not have a distinctly defined nucleus, whereas cyanobacteria are eukaryotic, meaning they contain nucleii. They are sometimes referred to as "blue-green algae", which can be a cause of confusion on their biological architecture. They can be both unicellular and multicellular. Their photosynthesis efficiency is generally higher than that of other plants, and some species of algae are considered to be amongst the proportionately fastest growing plants in the world [121].

Aside from the capability to be farmed on non-arable land, algae and cyanobacteria carry further benefits as biofuel sources. They have immensely rapid population growth rates, with a doubling of the biomass having been written as commonly happening within 24hours, and during exponential growth periods (such as early-stage population with full illumination across all members of a population) this

doubling happen in periods as short as 3.5 hours [109, 115]. Other papers suggest a more conservative figure of biomass doubling in 2-5 days [122]. The capacity for improvements on algal growth rate and oil production via biochemical and genetic engineering [123] is also a significant benefit over first- and second- generation plants. Whilst most interest has focussed on unicellular, small "microalgae", there is now interest in growing "macroalgae", a.k.a. seaweed [124].

There are two main ways to grow algae or cyanobacteria in large scale: using photobioreactors or raceway ponds. Diagrams and photograph examples are shown in Figure 1.13. The trade-offs between the two designs revolve around adequate illumination due to the algae's high optical density (saturated concentrations reach absorption coefficients of the order of $100m^{-1}$ [125]), the issues of contamination from unwanted algae species, nutrient and CO_2 control, and cost. Issues that affect both systems in different capacities include oxygen degassing and active cooling of the algae culture for PBRs, and significant loss of water through evaporative cooling and a greater difficulty, and therefore higher energy use, of algae harvesting for raceway ponds.

1.4.1.1 Photobioreactors

Photobioreactors (PBRs) are a closed, controlled environment so that conditions are kept ideal for algae growth (see Figure 1.13). The algae culture is generally, but not always, maintained as single-species. It is enclosed in a transparent array of tubes or plates which is being constantly circulated around via a pump, a nutrient vessel and a monitoring unit. The tubes are usually kept to diameters of 0.1m or less [115] in order to ensure sufficient light to penetrate the whole culture. The fundamental principle of these photobioreactors is to maximise the surface area - volume ratio, thereby providing a much higher oil yield per hectare compared to raceway ponds (which are discussed below). Chisti *et al.* (2007) state the biomass concentration to be nearly 30 times greater in comparison to raceway ponds [115].

Larger surface areas however imply more embodied energy used in materials for construction [109]. This is a contributor to one of the few issues for PBRs. The start-up and operational costs are extremely high, which is the major limitation to large scale production [126]. Secondly, they have been stated to consume more energy than they produce [127] and so have largely been used only for high-end products such as cosmetics and pharmaceutics. Kumar *et al.* (2015) state that the only commercially successful company operating PBRs are the production of astaxanthin, a food additive [128]. As a result most commercial algae companies utilise raceway ponds for large scale algae farming.

1.4.1.2 Raceway Ponds

Raceway ponds (Figure 1.13) are oblong closed loop recirculation ponds, that are shallow and large in surface area. They have been used for mass culture of algae since the 1950s [115]. Pond depths are up to 30cm, and can be tens of metres wide and hundreds of metres long. They are cheap and easy to build and operate [109, 115, 124, 129], and the channels are built in concrete or compacted earth, and sometimes lined with plastic, either for reflective purposes if white, or for ease of cleaning. The low surface area-to-volume ratio of the ponds, in comparison to PBRs, constrains a large amount of the algal population in a optically dark sections of the pond [115, 130], due to the high optical density of algae absorbing most incident light in the first few centimetres of the pond surface [109]. This is because algae cultures are maintained at maximum concentration, and between 10% [131] - 12% [132] of the pond content is harvested daily. This limits the volume productivity of ponds, and therefore means that the algae yield-per-volume of water is a lot lower than PBRs. This light issue is partially mitigated with the use of paddle-wheels, that provide constant mixing of the algae medium. This provides all algae some chance at receiving some sunlight whilst it moves within the turbulent waters.

Assuming then-recent data on capital and maintenance costs, Richardson *et*

al. in 2012 calculated the economics for both systems to be unfavourable for large scale biofuels production. Raceway ponds however were deemed to be more likely to decrease costs sufficiently to become economically feasible. The possibility of increasing biomass yield per volume of pond was not taken into consideration as a way to improve economic feasibility however, and is seen as a constant in economic modelling. This comes down to inherent optical properties of algae, and a lack of innovative optical solutions for raceway ponds.

Outlook on raceway pond economics has however turned slightly more optimistic

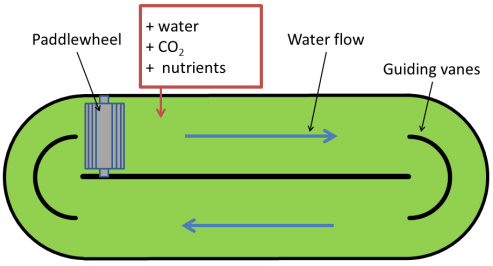

(a) Raceway pond schematic

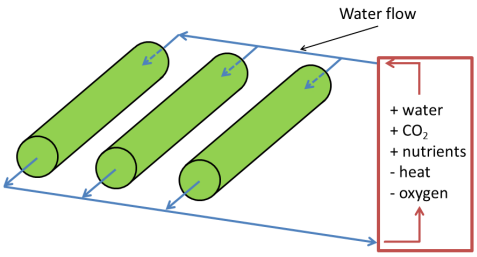

(b) Photobioreactor

(c) Satellite imagery of commercial algae raceway ponds (Cyanotech Corp.)

(d) A photobioreactor facility with an operational volume of 4000litres. (IGV Biotech)

Figure 1.13: The two methods of large scale algae production, raceway ponds and photobioreactors. Figure 1.13c shows satellite imagery of a commercial production facility in Hawaii that utilises raceway ponds for algae food supplements. Note the diverse colours of different algae species. Figure 1.13d shows a commercial facility that grows algae for high end cosmetic products. Raceway ponds are the most popular design due to their lesser initial and maintenance costs. Photograph attributes: 1.13c Map data @2016 Google., 1.13d : IGV Biotech, taken 26 April 2013. Licensed under CC BY-SA 3.0.

of late. Beal *et al.* ran a series of techno-economic and lifecycle analysis on different algae farm scenarios, differing on all aspects of production, from algae species, to electric power source and oil extraction methods. There was a range of pessimistic to optimistic scenarios. The most realistic one indicated a positive energy return on investment (EROI), with a value stated to be on par with U.S. shale oil (EROI=1.16) [133]. Whilst this signifies good progress in cost decrease / demand increase, EROI of values less than 3 have been linked to economic recession [134]. The target scenarios, whereby cutting-edge but yet commercially unproven techniques are used, yield values of EROI = 3.24 - 8.36. The highest EROI scenario involved locating the farm in Hawaii, and included electricity provided renewably through wind power, using combined heat and gas, nutrient recycling and obtaining cheap water through drilled wells. CO_2 supply was assumed to be available at no cost, i.e. the algae farm would have to be located near to a hydrogen plant, fossil fuel power station or cement plant [135].

1.4.2 Algae absorption properties and the issues can arise from them

Algae cultures at maximum concentration can have absorption coefficients of the order of $100m^{-1}$ in raceway ponds or even up to orders of $1000m^{-1}$ in PBRs [115, 125]. Scattering of incident light can be more significant than actual absorption. This is discussed in further detail in subsubsection 6.1.2.3. An example of algae absorption and scattering coefficients is shown in Figure 1.14, of *Chlorella vulgaris*, a commercialised species, in a concentration that is an order of magnitude greater than that found in raceway ponds [131].

A recent paper attempted to simulate illumination profile as a function of depth in a raceway pond for *C. Vulgaris* and *Spirulina Pl* in order to study their photosynthetic rate as a function of depth [136]. Photosynthetic rate can be considered a metric for algae growth. For an algae concentration of 0.3g/L, which is on the

lower end of the scale for concentration in a raceway pond (0.3g/L in [135, 137] and 0.5g/L in [131]), the authors state that the depth threshold for zero photosynthetic activity is 7cm for *C. Vulgaris* and *Spirulina Pl.*

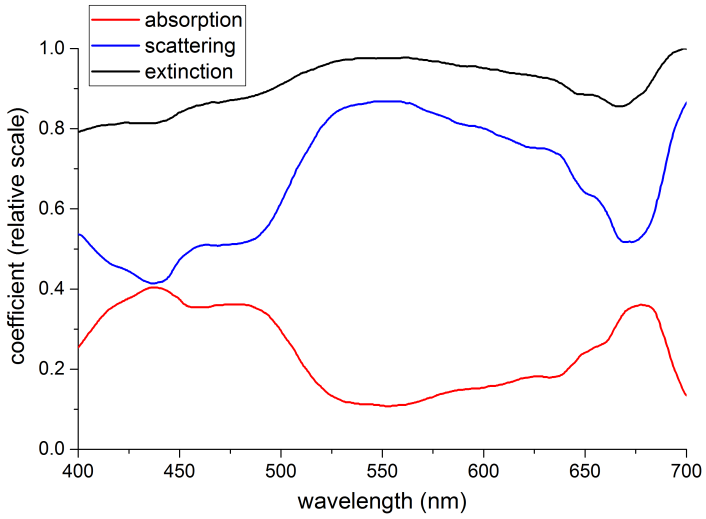

Figure 1.14: Absorption, scattering and extinction spectrum for *Chlorella vulgaris*. This data is taken from Hannis (2013) [125]. The scattering of light plays a bigger role in the extinction of light than absorption.

Algae have evolved to absorb more light than is needed for their own requirements, as a way to stifle competition in an environment with limited illumination. The excess light energy that is absorbed, is dissipated as heat and flourescence [109]. Whilst this gives an evolutionary advantage, it reduces the biomass yield in algae farms. Melis *et al.* (2009) have estimated this loss in harvested weight to be three-fold or greater [138]. Furthermore, as well as a decrease in efficiency of use of absorbed light energy, the excess also damages the photosynthetic machinery in the algae, a process called photoinhibition [139]. As such, the highest photosynthetic efficiencies occur at low light intensities. Melis *et al.* (2009) show that the light saturation of photosynthesis occurs are 400-600 μmolm^{-2}s^{-1} of sunlight, i.e 238 - 358 Wm^{-2} of full spectrum sunlight. Other studies show that optimal light intensities for some algal species can be as low as 200 μmolm^{-2}s^{-1}, which equates to 120 Wm^{-2} of natural sunlight [140, 141, 142].

With the aforementioned optical properties of algae, it is easy to see that conventional illumination procedures for algae is sub-optimal. On a cloudless spring day in the Northern Hemisphere, solar intensity will exceed that required to saturate photosynthesis at around 7 a.m, and continues to exceed it until around 5 p.m. Integrated over the course of the day and depth of a mass algae culture, Melis *et al.* estimated that photosynthesis over-absorbs and wastefully dissipates around 60% of the daily irradiance [138, 143].

1.4.3 Current innovative lighting solutions

All ideas for increasing light intensity/distribution in an algae culture has been for PBR designs in two different ways: By enhancing the illumination wavelength range to that of the photosynthetic absorption spectrum, or by increasing the total

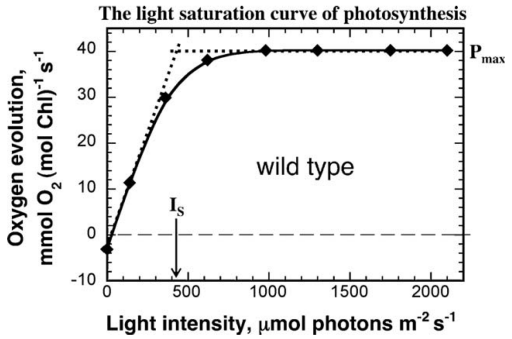

(a) Light saturation curve of photosynthesis of wild algae

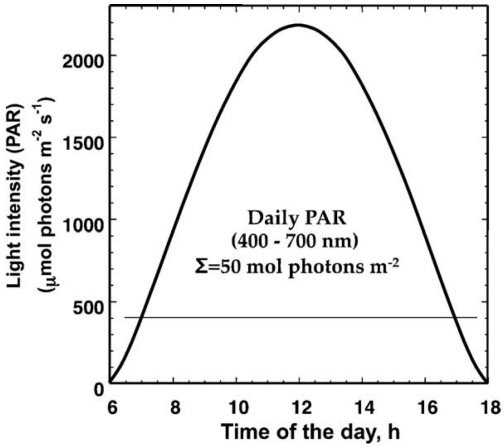

(b) Profile of the daily photosynthetically active radiation (PAR) at sea level.

Figure 1.15: 1.15a: The light saturation curve of photosynthesis, which is demonstrated as oxygen evolution. There is a linear increase in the photosynthetic rate, at which it saturates to a level P_{max} at around 400-600 μmol $m^{-2}s^{-1}$ of sunlight, which corresponds to around 238 - 358 Wm^{-2} of full spectrum sunlight. 1.15b: The profile of the daily solar photosynthetically active radiation (PAR) at sea level. PAR is the bandwidth of light within the solar spectrum which is useful for photosynthesis ($\lambda < 700$nm). The straight line is the photosynthetic saturation light intensity.The incident intensity exceeds that needed for optimal photosynthesis for most of the day. Figures reproduced with permission from Elsevier [138].

amount of incident light into a PBR. The one solution proposed for raceway ponds is to simply decrease a pond's depth to around 10cm [136]. This is more of a non-solution, considering a lower-volume pond for the same surface area of land leads to less total production for a farm.

1.4.3.1 Increasing light distribution via internal lighting

Ogbonna *et al.* (1999) and Chen *et al.* (2008) use a light tracking, light concentrating setup to feed sunlight into fibres, which are fed into a PBR [144, 145, 146]. Inside the PBR, the fibre surfaces can be roughened to allow the escape of light from the fibre into the algae culture, thereby providing uniform light distribution. Zijffers *et al.* (2008) use a single axis solar tracking linear Fresnel lens system to channel light into a light guide of a flat plate PBR. A similar design is presented by Dye *et al.* (2011) [147]. Further raytrace modelling showed that uniform light distribution through these waveguides was not possible over the course of a day [148]. A recent review of PBRs with internal lighting is presented by Heining & Buccholz (2015) [149].

1.4.3.2 Spectral manipulation of illumination

Wang *et al.* (2007) used red LEDs to obtain higher growth rates and biomass production in their culture [150], whilst Katsuda *et al.* (2004) suggested constant switching between red and blue LEDs to maximise production with theirs [151]. For another algae culture however, using a blue LED in addition to a red LED for simultaneous constant illumination however did not change the algae growth characteristics [152].

There has been interest in using luminescent material as spectral converters to illuminate algae with more useful light. Different wavelengths encourage different chemical processes in the algae. Shu *et al.* (2012) found that when illuminating a multiple-species culture, blue light was optimal for oil production, whilst red light

is optimal for growth rates [153]. Whilst some species prefer blue light illumination for increased growth rates [154], for the majority of investigations, illuminating algae with red luminescent light gives a higher algae growth rate than when illuminated with full-spectrum light [155, 156]. This is because most algae species contain chlorophyll types that absorb most efficiently in the red [152].

Either luminescent material is coated onto the front side [156, 157, 158] or the back side [159] of existing tubes or sheets, or bespoke PBRs are created with the tubes doped in luminescent material [160, 161]. It should be noted that all of these ideas are tailored towards the optics of PBRs, with not a single paper dedicated to raceway ponds.

Detweiler *et al.* created a virtually electronically self-sustaining LSC greenhouse [162]. Small algae cultures in flasks, as well as 50 litre raceway ponds, were tried. It should be noted that the raceway ponds used were rather deep. This can only be inferred from looking at an inset photo in a figure, as dimensions were not stated. The cultures in flasks experienced a very small increase in growth rates and yields when surrounded by LSC panels doped with Lumogen Red F 305. There was no difference in growth rates or yields between raceway pond cultures illuminated in a normal, or in a LSC greenhouse. The greenhouse however did have integrated solar panels which provided sufficient power to paddlewheels, fans, sensors and control electronic devices.

1.4.4 Thesis motivation - Novel optics for raceway ponds

At maximum population in an algae pond, incident light penetrates up to 7cm due to the algae's high optical density. A significant amount of this light is wasted through heat dissipation or destruction of the photosynthetic machinery of the algae. Not only is biomass growth stunted due to photoinhibition, but also due to a significant proportion of the population residing in dark optical zones for extended

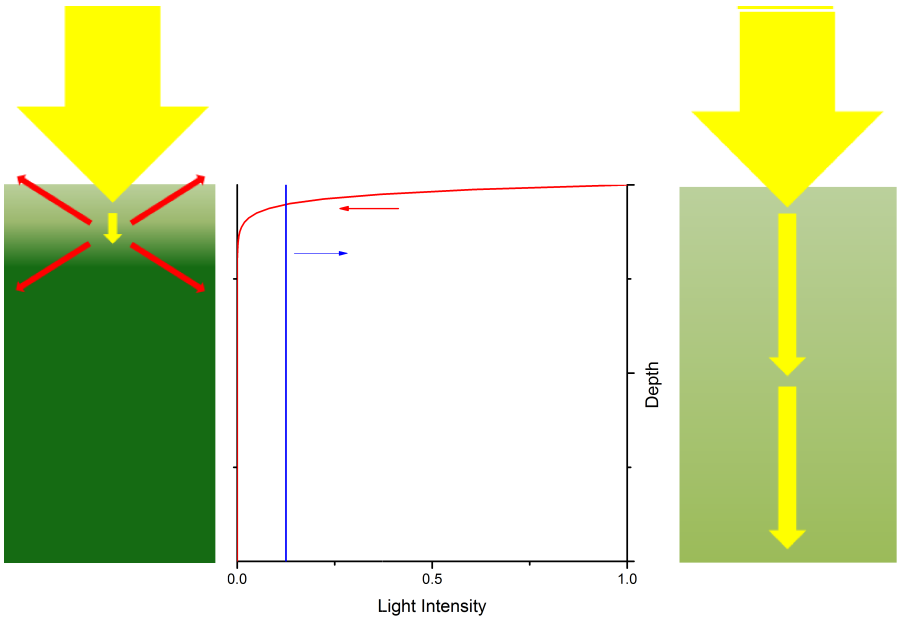

Figure 1.16: Looking at a cross section of a raceway pond. Current illumination intensities across the depth of a pond are highly non-ideal. The first few centimetres absorb all illumination, with a large dark zone, as shown in (a). This is due to saturated concentrations of algae being of the order of 100m^{-1}. Excess energy is dissipated either as heat, or as physical destruction of the algae's own photosynthetic machinery. The ideal light absorption profile across the depth of a pond is a uniform, lower intensity profile (blue line in (b)), as opposed to the normal steep exponential drop off profile (red line in (b)).

periods of time. The ideal illumination profile through a pond is a constant, lower intensity light at the photosynthetic saturation intensity. This is shown pictorially in Figure 1.16.

Until now, the optics of raceway ponds have not been investigated, with the high optical density of a populated pond being an accepted optical limitation. Discussions on raceway optics revolve solely around the trade-offs in pond depths with biomass production[136, 128]. Whilst paddlewheels are used to enhance algae mixing, they do not solve the issue of the optical dead zone within the pond and photoinhibition effects on the upper layer due to over-absorption of light. In this thesis, a truly novel optical concept, called the Luminescent Solar Diffuser (LSD) is introduced to alleviate both these issues by distributing incident light across the

depth of the pond.

The objective of the luminescent light diffuser (LSD) is to capture incident sunlight from the surface of the pond, and redistribute it evenly across the depth of a raceway pond, thereby giving a uniform illumination profile across the depth of a raceway pond. Being a standalone device, it can be retrofitted to any existing raceway pond. This would increase the algae growth rates by a) preventing excess illumination onto the first few centimetres of the pond, thereby decreasing photosynthetic machinery damage and thermal emission, b) reducing the volume of the dark optical zone by waveguiding the excess light from the top surface into the deeper sections, effectively increasing the illumination area/volume ratio of the pond, and c) spectrally converting less efficiently used short-wavelength incident light into that of a more usable wavelength for photosynthesis.

1.5 Thesis structure

Chapter 1 is the introduction to a sustainable future, LSCs in BIPV, photoelectrochemical water splitting for solar hydrogen and algae biofuels for solar biofuels. Motivation for the thesis is given at the end of each of the topic introductions.

Chapter 2 contains LSC theory and background. It discusses intrinsic loss mechanisms and optical designs to improve performance. A history of investigation in cylindrical geometries is given. Recent novel uses for luminescent material is presented.

Chapter 3 demonstrates the methods used in the thesis. This includes LSC characterisation and photoluminescence measurements of solar cells. The raytracer used in this thesis, pvtrace, is introduced as well as the upgrades developed by the author in order to complete his work.

Chapter 4 gives results on cylindrical LSCs. Measurements on fibre LSCs made at Nanforce Ltd are presented. Cylindrical LSC arrays are modelled first in 2D to demonstrate incident light trapping, and then in 3D to demonstrate its effect in boosting optical efficiencies on two specific days. Tessellation variations of fibres are also discussed.

Chapter 5 introduces novel waveguiding optics into a doubly-illuminated water splitting reactor. Raytrace modelling on the reflective cone is shown, as well as practical results taken at a high-concentration flash facility in SUPSI, Switzerland. It also introduces the concept of a quantum well solar cell (QWSC) as a luminescent centre. Edge photoluminescence when illuminated uniformly by a laser is measured to determine the waveguiding efficiency of a QWSC, and its total photoluminescence capability when embedded inside a waveguide and illuminated at high concentration is also investigated.

Chapter 6 introduces the luminescent solar diffuser (LSD). The construction of this model on the raytrace model as well as the addition of a genetic algorithm to optimise the LSD shape is presented.

Chapter 7 contains the conclusions. The thesis achievements are summarised, and the scope for future work is given.

1.5.1 Contributions to this thesis

1.5.1.1 Raytracing program

The raytrace program "pvtrace" was obtained online on GitHub [163]. It was written by Dr. Daniel Farrell on Python2.7, and is open source and free. It was built primarily for modelling LSCs [164]. The author added parallelisation functionality to shorten simulation times. He wrote all functions as described in section 3.1 to measure realistic light scenarios on cylindrical arrays and to model a cone. He

worked in tandem with Callum Deakin to build mesh capability into pvtrace. Tom Wilson wrote the genetic algorithm (GA), and worked in tandem with the author to enable communication between the GA and pvtrace.

1.5.1.2 Cylindrical LSCs

The author alone decided to investigate light paths through cylindrical arrays, discovering a form of angle-dependent light trapping. He developed the 3D simulations. He shadowed Dr. Emiliano Bilotti on manufacturing fibre LSCs by fibre extrusion at Nanoforce Ltd. He performed all experimental measurements for photon concentration vs fibre length and redshifting through re-absorption and re-emission. He was first author for two conference papers (IEEE PVSC and WCPEC) and one full publication in *Optics Express*.

1.5.1.3 Optics for a doubly-illuminated PEC reactor

The author joined the PEC reactor project as the contributor responsible for measuring the QWSC photoluminescence and designing the optics for waveguiding incident light into the reactor. The PEC reactor was designed by Dr. Anna Hankin and Prof. Geoff Kelsall, with Emer. Prof. Keith Barnham producing the idea for using a QWSC for both electricity generation and photoluminescence. Dr. James Connolly used the solar cell modelling software SOL to determine the radiatiative efficiency of the QWSC. The QWSC samples were prepared by Saurabh Kumar and Dr. Kenneth Kennedy. The author performed all experimental measurements on the QWSC, determining its unsuitability for the concept. The author created the idea for a reflective cone embedded in a waveguide, and created all code for raytrace simulations. He worked in tandem with Dr. Mauro Pravettoni at SUPSI to perform full spectrum high concentration measurements of both the QWSC and reflective cone embedded in a waveguide. Dr. Anna Hankin designed the full PEC reactor trolley, and the author designed the optical setup. The author and Dr. Anna Hankin performed outdoor measurements in tandem. The author was first

author on a conference paper on the QWSC hybrid optics (IEEE PVSC) and a second author on a conference paper (SolarFuel16). The author and Dr. Anna Hankin will be joint first authors in the upcoming publication.

1.5.1.4 Luminescent Solar Diffuser

The author alone decided to pursue an optics solution for lighting issues in algae raceway ponds. He devised the basic design and project to investigate its optimal design. Contributions to the simulation code are given above in subsubsection 1.5.1.1. The author performed all calculations for the performance of the LSD, and is first author on a manuscript currently submitted for publication.

1.5.2 Thesis flowchart

A process flowchart for the work in the thesis is shown on the next page.

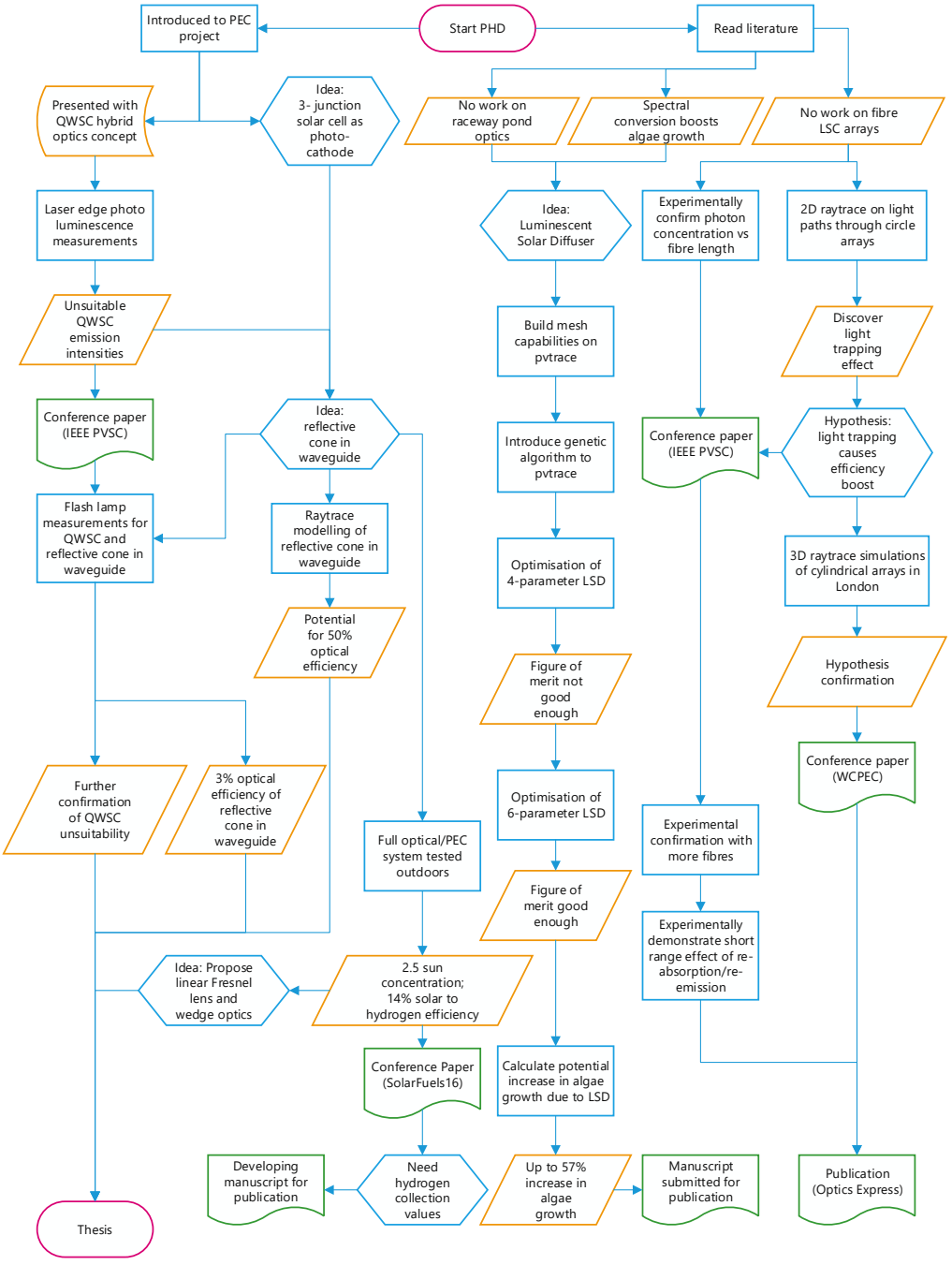

Figure 1.17: Process flowchart for the work presented in the thesis.

Chapter 2

LSC theory and background

This chapter introduces the luminescent solar concentrator. An overview is given on its fundamental concept. Luminophore functionality is discussed. Waveguide physics is shown as well as a discussion on loss mechanism trade-offs with differing refractive indices. A review on previous work on cylindrical geometries is given as well as different uses for luminescent material.

2.1 Basic principles

An LSC in its basic design is a luminescent panel made of highly transparent glass or plastic [49, 50]. It can be homogeneously doped with luminescent materials [51, 52], shown in Figure 2.1a, or consist of a transparent waveguide coated with a thin luminescent active layer, as shown in Figure 2.1b [165, 166]. There are a wide range of luminescent molecules, both organic and inorganic based [53, 59]. Light passes through the top surface and is absorbed by a luminescent centre, or luminophore, inside the LSC, which then re-emits it at a redshifted wavelength. This re-emitted light can then be trapped in the waveguide by total internal reflection (TIR) and directed towards the edges. PV cells can be coupled onto the edges to absorb the light. Mirrors [167] and wavelength selective coatings [168, 169, 170] can be used on surfaces to mitigate re-emission escape losses. One of the main advantages of the LSC, other than the ability to absorb both direct and especially

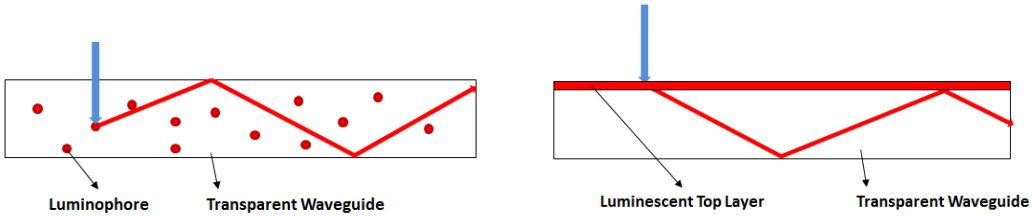

(a) Homogeneously doped LSC, where the entire waveguide is doped with a luminescent dye

(b) LSC with a coated luminescent top layer. The waveguide is ideally completely transparent.

Figure 2.1: The Luminescent Solar Concentrator in both basic forms: the homogeneously doped LSC (a) and the thin-film LSC (b). In both cases, incident light strikes the the LSC and is absorbed by the luminescent material. The re-emitted light is waveguided to the edges by total internal reflection to the edges.

diffuse light without sun tracking systems [171], is that the emission spectrum of its emitted light can be manipulated to match the peak absorption waveband of the specific PV cell in use by changing the luminescent species.

2.2 Figures of merit

There are two figures of merit in use for a LSC: optical efficiency and photon concentration. The optical efficiency μ_{opt} is the number of photons exiting the useful surfaces divided by the number of incident photons:

$$\mu_{opt} = \frac{N_{emission}}{N_{incident}} \tag{2.1}$$

The photon concentration C_γ takes into account the geometric concentration of an LSC C_G. This is the ratio of useful light emitting area and the incident light collection area:

$$C_G = \frac{A_{incident}}{A_{emission}} \tag{2.2}$$

The photon concentration C_γ is the ratio of photon flux coming out of the useful surfaces and the incident photon flux:

$$C_\gamma = \frac{\phi_{emission}}{\phi_{incident}} = C_G \cdot \mu_{opt} \tag{2.3}$$

This means that if a LSC has a photon concentration of $C_\gamma = 1$, the photon flux exiting the edges upon which the light will be utilised is as high as the incident photon flux.

2.3 LSC component properties and loss mechanisms

2.3.1 An overview of losses

The basic performance properties of a LSC are affected by the choice of luminescent dye and waveguide material used. It can be summarised by a breakdown of a LSC's optical efficiency μ_{opt} [53]:

$$\mu_{opt} = (1 - R) \cdot \mu_{TIR} \cdot \mu_{abs} \cdot \mu_{PLQY} \cdot \mu_{Stokes} \cdot \mu_{host} \cdot \mu_{surface} \cdot \mu_{self} \tag{2.4}$$

where R is the reflection of solar light from the LSC surface, μ_{TIR} is the total internal reflection efficiency related to a waveguide's refractive index, μ_{abs} is the fraction of solar light that is absorbed by the luminescent material, μ_{PLQY} is the photoluminescent quantum yield of the luminescent dye(s), μ_{Stokes} is the energy lost due to heat between light absorption and emission, μ_{host} is the transport efficiency of the waveguided photons related to host material absorption, $\mu_{surface}$ is the reflection efficiency of the waveguide determined by the smoothness of the waveguide surface and μ_{self} is the transport efficiency of the waveguided photons related to re-absorption of the emitted photons by another luminophore [50, 53]. A diagrammatic representation of the loss mechanisms is shown in Figure 2.2 and the following sections summarise the mechanisms behind each loss factor.

The LSC's main loss mechanisms can be largely attributed to the luminophore properties, waveguide material properties and surface properties. Some loss mecha-

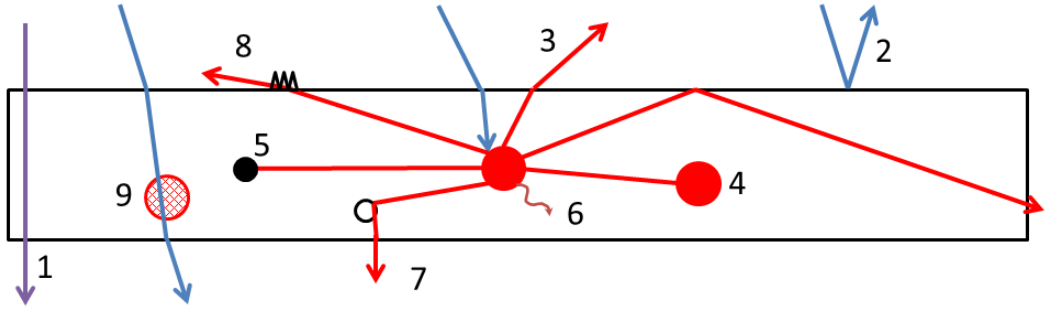

Figure 2.2: Loss mechanisms in a LSC: 1) Transmission of unabsorbed incident light; 2) Reflection of incident light; 3) Emitted light escapes through escape cone due to less-than-critical angle incidence angle on the LSC surface; 4) Re-absorption of luminescent light by another luminophore; 5) Waveguide non-radiative absorption of luminescent light; 6) Non-radiative loss of luminophore due to non-unity luminescent quantum yield; 7) Luminescent light is scattered out of the LSC due to waveguide material; 8) Luminescent light escape due to surface scattering; 9) Luminophore degradation

nisms are more significant than others. For example surface scattering (Figure 2.2.8) is negligible, whilst the largest losses are incident light not being absorbed (Figure 2.2.1) and emitted light escaping from the escape cone (Figure 2.2.3). Depending on the type of luminescent material used, re-absorption of emitted light (Figure 2.2.4) can be a significant factor.

2.3.2 Luminescent Material

The ideal luminophore needs the following requirements [53]:

- Broad spectral absorption
- High absorption efficiency over the whole absorption spectrum
- Large Stokes Shift (No or low overlap in absorption and emission spectra)
- High luminescent efficiency (quantum yield)
- Matching the emitted photons to the spectral response of the coupled photodevice
- Solubility in the host matrix material

The process of luminescence and a breakdown of the various characteristics

mentioned is explained below. The term photo-device is used for anything that absorbs light for a higher purpose, such as a solar cell.

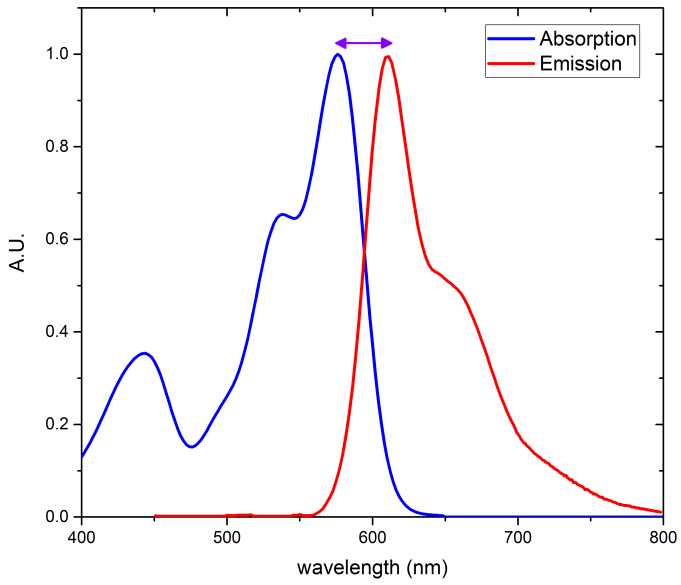

Figure 2.3: Absorption and emission spectra for Lumogen F Red 305, a commercial luminescent dye. The difference in peak wavelengths for absorption and emission, displayed by the purple arrow, is called the Stokes Shift.

2.3.2.1 Luminescence

This thesis focusses on using organic luminescent material. A brief introduction to luminescence is given. Further information can be found elsewhere [54]. A photon of energy higher than the energy gap between the ground and first excited state is absorbed by an electron in the ground state, giving it enough energy to transition into the first excited state. Kasha's rule states that photon emission occurs generally only from the lowest excited state of a molecule [172]. The electron relaxes, or thermalises, down from whichever vibrational state it ended up in, to the lowest excited state extremely quickly (100 - 1000 fs) by the molecule transferring the excess energy into the medium. This happens generally through collisions with other molecules. At the lowest excited state it can then radiatively decay down to the ground state.

As can be seen in Figure 2.3, there is a redshifting of the emission wavelength peak compared to the absorption peak. This difference in wavelength, shown as the purple arrow, is defined as the Stokes Shift [173]. Whilst redshifting of an emitted does occur due to energy lost by vibrational relaxation of an excited electron, in organic materials the emission spectrum can be attributed to the interaction between the luminescent molecule (luminophore) and the medium it is held in, be it liquid solvent or a polymer matrix. The two materials interact with each other by electrostatic and van der Waals forces and arrange each other to approach an interaction minimum. The effect of multidimensional solvent dynamics on reactions can be described by a one-dimensional variable equal to the energy to move the solute along a reaction coordinate [174]. The interactions between the luminophore and the medium molecules are different in the ground and excited state, and the Franck-Condon principle can be applied here, which approximates electronic transitions to be instantaneous in comparison to the timescale of nuclear movements [175], due to the nucleus' massiveness. In this case, electronic transitions are very fast compared with the motion of molecule rearrangement to attain an interaction minimum.

When a luminophore absorbs a photon and enters an excited state, it is taken away from this equilibrium state, and the excited potential well is shifted along the reaction coordinate, as demonstrated in Figure 2.4a. The rearrangement of the solvent molecules corresponds to the black arrows in Figure 2.4a. The quantum mechanical formulation of this principle is that the intensity of a vibronic transition is proportional to the square of the overlap integral between the vibrational wavefunctions of, in this case, the ground and the first excited state [54]. This means in excitation, there are certain preferred transitions. Due to Kasha's rule however, emission can only occur from the lowest excited state. The peak of the wavefunction is shifted in space, which gives rise to a different set of preferred transitions. If the ground and excited state are similar in shape, the spacing of the dominant vibronic bands are about the same in absorption and emission. This can exhibit a mirror

image relationship between the absorption and emission profile of a molecule. This is roughly seen in the absorption and emission spectra for Lumogen F Red 305 [176] (Figure 2.3).

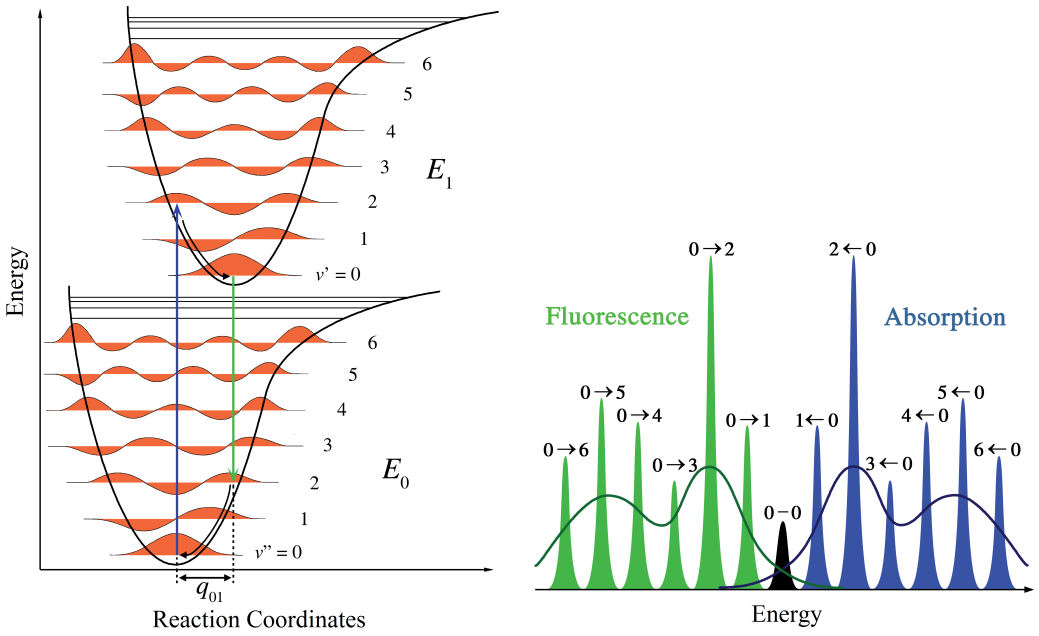

(a) Energy diagram for the ground state E_0 and the first excited state E_1.

(b) Spectral representation of the absorption and emission spectra corresponding to the energy diagram.

Figure 2.4: Diagrams depicting the Franck-Condon principle. Solvent motion can be assumed to be stationary in comparison to electron motion. As such electronic transitions are favoured when there is minimal change in the reaction coordinates. The intensity of a transition is proportional to the square of the overlap integral between the vibrational wavefunctions of the ground E_0 and the first excited E_1 states. When E_0 and E_1 are shifted, this gives rises to different preferred vibronic transitions due to Kasha's rule (see above). Both diagrams drawn by Mark M. Somoza, licensed and modified under CC BY-SA 2.5. [177, 178]

By extension of Kasha's rule, the emission spectrum is independent of excitation wavelength. Vavilov's rule is a corollary of Kasha's rule, which states that because excited electrons tend to relax to the lowest excited state non-radiatively, the photoluminescence quantum yield μ_{PLQY} is generally independent of the excitation wavelength [179]. It is demonstrated as process 6 in Figure 2.2. It is equal to the probability that the absorption of a photon by a molecule will be followed

by a photon emission. In equation form it can be expressed as:

$$\mu_{PLQY} = n_{em}/n_{ab} \tag{2.5}$$

where n_{ab} is the number of photons incident on a molecule and n_{em} is the number of photons emitted by the molecule. The PLQY can be less than unity if the decay of an excited electron happens due to non-radiative processes. Intersystem crossing can occur, where the excited electron can transfer to a state with no radiative coupling to the ground state, for example from a singlet to a triplet state. Internal conversion can also occur, when the vibrational modes of a lower excited state overlap enough with the current excited state which allows an electron to decay purely through relaxation.

2.3.2.2 Absorption limits

The limits of LSC absorption are dictated by the absorption cross section of the luminescent layer and the spectral bandwidth of the luminophore. Typical organic dyes have an absorption bandwidth of 100-200nm [180, 181], as demonstrated by the absorption spectrum of Lumogen F Red 305 in Figure 2.3. Organic luminophores can be mixed with a polymer matrix up to around 2 - 2.5% concentration by weight, which can give a LSC a peak absorption coefficient of the order of 10,000m^{-1}. This means, by using the Beer-Lambert relation, the luminescent layer of the LSC at maximum luminophore concentration needs to be at least 500μm thick to absorb 99% of incident light at the peak absorption wavelength. Even at that thickness, incident light not at peak wavelength has a probability of not being absorbed. Any photon of wavelength not in the absorption spectrum will be transmitted through the luminophore. The ideal LSC would absorb all incident wavelengths shorter than the bandgap of the photo device which is attached to the edges of the LSC. Using Lumogen F Red 305 (Figure 2.3) as an example, its absorption band edge is at around 650nm. Under solar AM1.5G spectrum, integrating the photon flux up until 650nm shows that it can absorb up to 24% of the total incident photon flux.

In reality, if the concentration of luminescent material is not high enough, then the absorption cross section of the LSC will not be high enough to absorb all light in its absorption range. This characteristic is expressed as the absorption efficiency μ_{abs} in Equation 2.4.

2.3.2.3 Luminescence losses

Re-absorption of luminescent light is linked to the overlap of absorption and emission spectra of the luminophore [182, 183], and the absorption coefficient of the luminescent layer, which is in turn linked to the concentration of luminescent material in the host material. The larger the spectral overlap, the larger the chances of re-absorption loss [184, 69]. This is shown in the loss factor μ_{self} in Equation 2.4 represented by process 4 in Figure 2.2, which is the fraction of luminescent photons which reach the LSC edge without having been re-absorbed. Each time a luminescent photon is re-absorbed, it will suffer a probability of being lost through non-unity PLQY, or through escape cone losses (process 3 in Figure 2.2).

Each re-absorption and re-emission event results in the photon losing energy, thus causing a redshift in the luminescence spectrum. There comes a point where a photon has been re-absorbed and re-emitted enough times that it does not have enough energy to be re-absorbed again. It has been shown that re-absorption effects occur within the first few centimetres of a LSC [185]. It was shown in the context of fibre LSCs (introduced later in section 2.4) that maximum re-absorption when around 40% of the total number of luminescent photons produced are re-absorbed [69]. Modelling results have shown that introducing anisotropy luminophore emission can actually decrease the average number of re-absorption/re-emission events for a photon compared to isotropic emission [186]. These models however do not take into account a small tail in the absorption spectrum which stretches in the emission spectral region. This tail has a deleterious effect on overall LSC performance, and has greater effect on larger LSCs [187].

The perfect luminophore would have sharp spectral boundaries between the absorption and emission peaks, as well as minimal Stokes Shift. The reality is that re-absorption from spectral overlap is a much larger loss mechanism than the energy lost in the Stokes Shift, caused by escape cone losses and non-unity PLQY. For this reason the onus on luminophore research is to find materials with larger Stokes Shifts [188]. Whilst organic luminophores traditionally have a small Stokes Shift, including recent materials [189, 190], some new organic materials are being discovered with larger Stokes Shift [191].

Non-radiative energy transfer can play a part in luminescence performance. At a high enough concentration in a matrix, such as above 2.5% concentration by weight for Lumogen F Red 305, luminescent material can agglomerate and a process called luminescence concentration quenching occurs, where the luminescence quantum yield decreases [192]. If luminophore molecules enters a small enough distance of each other, Förster non-radiative energy transfer (FRET) [193] occurs which reduces the overall percentage of excited states decaying radiatively. The FRET rate is determined by the expression [193]:

$$k_{FRET} = \frac{1}{\tau_D^0}\left(\frac{R_0}{R}\right)^6 \tag{2.6}$$

where τ_D^0 is the lifetime of the excited donor state in the absence of acceptor molecules, and R_0 is the critical transfer distance constant. When $R = R_0$, energy transfer and spontaneous radiative decay have equal rate constants, making FRET and radiative decay equally probable [54]. The distance between molecules where FRET becomes a significant process is of the order of 5-10nm. Whilst luminescence concentration quenching does occur with luminescent materials, the mechanism does not necessarily have to be FRET, with molecules such as Lumogen F Red 305 having distance relations to quenching being related more to the power of -4, as opposed to the power of -6 like in the FRET expression. Whilst the authors who

presented this result suggest a mix between FRET and shielding of excited states changing interaction strengths as the underlying cause, a consensus has not yet arisen on it [194].

Organic luminophores, although having issues with low Stokes Shift and isotropic emission, still have their merits. They have near-unity PLQY, are available in a wide range of colours and are now more photostable [182]. They are also widely available, non-toxic and cheap.

Luminescence re-absorption and isotropic emission can be considered the major loss mechanism in LSC function. Light transport within a LSC is poor when these two loss mechanisms are substantial: each re-absorption occurrence provides a further probability of light being re-emitted outside of the TIR region (discussed below in subsection 2.3.3). Increasing the geometric ratio of a LSC by increasing the surface area would therefore decrease the probability of a luminescent photon reaching a solar cell on the LSC edge before its direction is randomised by a re-absorption/re-emission event. Thermodynamic modelling by Farrell & Yoshida of general LSC function demonstrated that a LSC coupled with a Shockley-Queisser solar cell with matching bandgap actually decreases the cell current density with increasing geometric concentration. [195]. The authors highlight luminophore alignment schemes to induce anisotropic luminescence favourably into the waveguide as the most promising approach to solving this problem. They demonstrate that a conventional LSC with isotropically emitting luminophores can only attain efficiencies of 10% with a geometric concentration ratio of $C_G = 5$ and 2% with $C_G = 30$. Introducing anisotropy to luminescence gives an operating limit of 30% for any geometric concentration ratio.

2.3.3 The waveguide

The waveguide material will have a refractive index greater than that of air. A LSC concentrates light by trapping luminescent light by total internal reflection (TIR) and waveguiding it to the edges. Refraction, and the angle for TIR is determined by Snell's law:

$$\frac{sin\theta_i}{sin\theta_t} = \frac{n_2}{n_1} \tag{2.7}$$

where n_1 is the incident refractive index, n_2 is the transmitted refractive index, θ_i is the incident light's angle to the incident plane's normal and θ_t is the resultant transmitted light's angle to the incident plane's normal. The effect of Snell's law is demonstrated in Figure 2.5. The critical angle θ_c is the threshold angle for TIR and occurs when $\theta_t = 90°$:

$$\theta_c = sin^{-1}\left(\frac{n_{air}}{n_{LSC}}\right) \tag{2.8}$$

The critical angle determines the escape cone loss from luminescent light. Assuming isotropic emission from a luminophore, one can determine the trapping efficiency μ_{TIR} from the escape cone μ_{escape}. Firstly the escape solid angle is calculated:

$$\Omega_{escape} = \int_0^{2\pi} d\phi \int_0^{\theta_c} sin\theta d\theta = 2\pi[1 - cos\theta_c] \tag{2.9}$$

Taking into account that this is the escape cone for one surface, the total escape cone is doubled. The escape loss μ_{TIR} is a ratio of the total escape cone divided by the total solid angle 4π:

$$\mu_{escape} = \frac{2 \cdot \Omega_{escape}}{\Omega_{total}} = 1 - cos\theta_c \tag{2.10}$$

The trapping efficiency μ_{TIR} is then:

$$\mu_{TIR} = 1 - \mu_{escape} = cos\theta_c = \sqrt{1 - \frac{1}{n_{LSC}^2}} \tag{2.11}$$

The escape cone loss is shown as process 3 in Figure 2.2. The difference in refractive indices between air and the LSC also give rise to partial reflection of incident light, and can be calculated using the Fresnel equations. Incident light from the sun contains two polarisation states, one normal to the plane of incidence (s-polarisation) and one parallel to it (p-polarisation). Fresnel reflection equations are different for s-polarised reflection R_s and p-polarised reflection R_p. The total reflectivity for unpolarised light is the average of the two polarisation reflectivities:

$$R_s = \left| \frac{n_1 cos\theta_i - n_2 cos\theta_t}{n_1 cos\theta_i + n_2 cos\theta_t} \right|^2 \tag{2.12}$$

$$R_p = \left| \frac{n_1 cos\theta_t - n_2 cos\theta_i}{n_1 cos\theta_t + n_2 cos\theta_i} \right|^2 \tag{2.13}$$

Substituting in Snell's law to replace θ_t with θ_i gives:

$$R_s = \left| \frac{n_1 cos\theta_i - n_2 \sqrt{1 - \left(\frac{n_1}{n_2} sin\theta_i\right)}}{n_1 cos\theta_i + n_2 \sqrt{1 - \left(\frac{n_1}{n_2} sin\theta_i\right)}} \right|^2 \tag{2.14}$$

$$R_p = \left| \frac{n_1 \sqrt{1 - \left(\frac{n_1}{n_2} sin\theta_i\right)} - n_2 cos\theta_i}{n_1 \sqrt{1 - \left(\frac{n_1}{n_2} sin\theta_i\right)} + n_2 cos\theta_i} \right|^2 \tag{2.15}$$

$$R_{total} = \frac{1}{2}(R_s + R_p) \tag{2.16}$$

There is a trade-off between incident reflectivity R_{total} and the trapping efficiency of a waveguide μ_{TIR}. This trade-off is shown in numberical form in Table 2.1 and in graphical form in Figure 2.6. A 100,000 photon raytrace simulation using pvtrace (introduced in section 3.1) was set up of a 0.15 x 0.15 x 0.04cm LSC with a 250μm thick Lumogen F Red 305 film at an absorption coefficient of

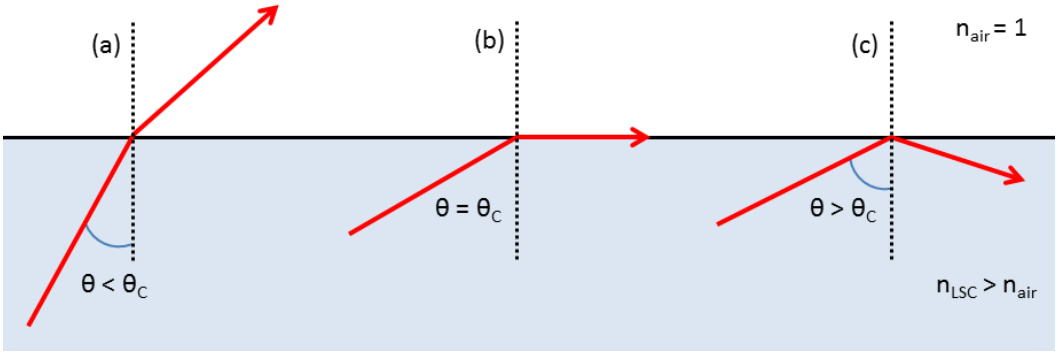

Figure 2.5: Visual representation of Snell's law. (a) light is refracted through a medium, (b) Total internal reflection (TIR) occurs at the critical angle θ_C, (c) an incident angle $\theta > \theta_C$ will cause light to be reflected by TIR back into the medium.

11,000m^{-1}. Varying the LSC refractive indices between $n = 1.5 - 1.8$ suggest that incident reflection plays a bigger part in LSC efficiency than escape cone losses from isotropic luminescent emitters. Results are shown in Table 2.2. Using the same light spectrum, efficiencies are lower for diffuse light conditions due to the increased reflectivity at higher angles of incidence. In reality, diffuse light is more blue in nature, and the lack of presence of infra-red photons in the spectrum elevate efficiency values. This is shown in the fourth column in Table 2.2.

Refractive Index	Incident Reflection	Trapping Efficiency
1.5	4.0%	75%
1.6	5.3%	78%
1.7	6.7%	81%
1.8	8.2%	83%

Table 2.1: Incident reflection and trapping efficiency of LSCs with different refractive indices

Looking back to Figure 2.2 and Equation 2.4, the loss mechanisms discussed have been the trapping efficiency μ_{TIR}, shown as process 3 and the Fresnel reflection, shown as process 2. The surface of a waveguide, unless highly polished, will not be perfectly smooth and so iregularities will induce some scattering of previously TIR trapped light out of the LSC. This is caused by the possibility of a photon hitting a surface imperfection at an angle of incidence of less than the critical angle, which would have not been the case if that point on the surface were perfectly

Refractive Index	Normal Incident Light	Diffuse incident light	Diffuse incident light & spectrum
1.5	5.3%	4.9%	8.7%
1.6	4.8%	4.3%	7.6%
1.7	4.1%	3.7%	6.7%
1.8	3.6%	3.3%	6.1%

Table 2.2: Comparing optical efficiency values for simulations on a Lumogen F Red 305 LSC with different refractive indices. The simulation used AM1.5 spectra with planar and diffuse (hemispherical) light conditions. The last column uses only the diffuse component of AM1.5 to demonstrate efficiency elevation by lack of infra-red photons.

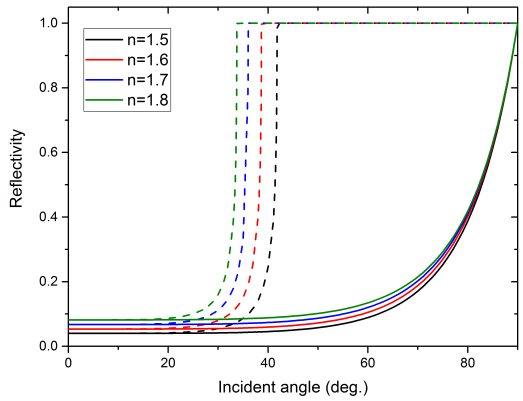

Figure 2.6: Fresnel reflection coefficients for an air-LSC interface (solid line) and LSC-air interface (dashed line) for varying refractive indices. Increasing the refractive index affects the critical angle θ_c more than it does the reflection coefficient at normal incidence.

smooth. Water moisture droplets contribute to surface non-uniformity and so can add to scattering. These are shown as process 8 in Figure 2.2. This is however not a major loss mechanism, with a clean, smooth polymethyl methacrylate (PMMA) surface reaching loss factors of only 0.0002 per reflection [196]. Impurities in the waveguide can also lead to scattering of light (process 7 in Figure 2.2).

The waveguide host material will also have an absorption coefficient, which will parasitically absorb luminescent light (process 5 in Figure 2.2). PMMA can reach absorption coefficients of the order of 0.1m^{-1}. An example transmission spectrum of a PMMA sheet is shown in Figure 2.7. Parasitic absorption and waveguide scattering only becomes significant in the large scale. In smaller scales like LSCs,

they get dominated by luminophore light re-absorption, which is primarily a short range effect [197]. PMMA and borosilicate glass are the most common waveguide materials, but other materials have been investigated as host materials such as polycarbonate (n ≈ 1.59) [198], polysiloxane [199, 200], perfluorinated polymer-based materials [201, 202] and various other types of glasses with varying refractive indices of n = 1.5-1.8 [203, 204, 198].

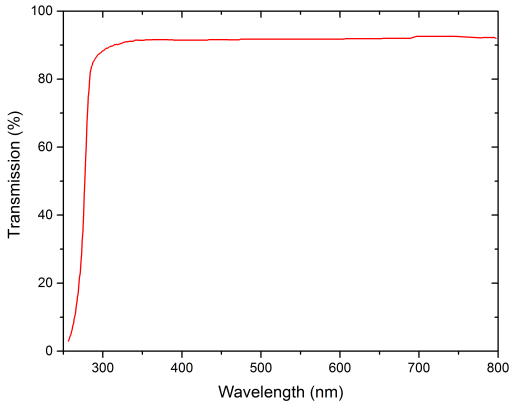

Figure 2.7: Transmission spectrum of a Clarex U.V. transmission filter, made out of high quality PMMA. Data taken from the Weatherall Ltd Clarex webpage [205].

2.4 Cylindrical LSC geometries

Initially addressed by Batchelder *et al.* [206, 207] as an alternative geometry to planar LSCs, cylindrical LSCs (CLSCs) offer better photon concentration than planar LSCs due to a greater geometrical concentration C_G. In this geometry, the luminescent edges are limited to the two ends of the cylinder therefore in comparing to planar geometries we shall also use just two emitting edges. The incident light collection area of both a square and cylindrical geometry LSC is its diameter multiplied by its length. This is highlighted as yellow in Figure 2.8. The photon concentration difference arises at the ends. The luminescent emission area for one end of the LSC is the circular area πr^2 whilst for the square its the square area $4r^2$. This means the geometrical advantage ratio of cylindrical to planar geometry is $\pi/4$. This value is highlighted as the red area in Figure 2.8. Due to the curved

surface of a cylinder, surface reflection of normal incident light sums up to 6.9% for the whole surface, almost double that of a planar surface. In having an array of cylinders, some of the light reflected off a cylinder can be transmitted into its neighbour. In this instance, surface reflection drops to 2.7% [208]

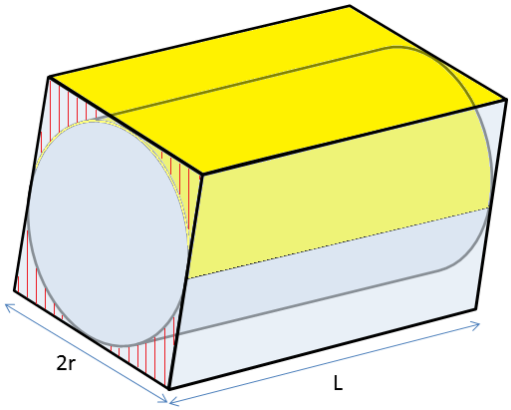

Figure 2.8: Cylinder geometry versus square geometry

CLSCs have experienced a small resurgence in the past decade when it was claimed that a CLSC can outperform a planar LSC of equal volume and collection area by a factor of 1 - 1.9 in terms of optical efficiency [208]. Since then CLSCs have been investigated, albeit not extensively, as standalone devices.

Colantuono *et al.* confirmed using raytracing techniques that CLSCs always outperform similarly sized planar LSCs in terms of photon concentration, especially in conditions of isotropic (diffuse) illumination [209]. Edelenbosch *et al.* first found that coated fibres have a higher photon concentration than homogeneously doped fibres [69]. This is due to luminescent light being emitted closer to the edge, which has a higher trapping efficiency. The trapping efficiency of a luminescent photon varies depends on the distance r from the centre of the cylinder. McIntosh *et al.* [208] derived an expression for the escape fraction as a function of distance from centre r. The trapping fraction, which is unity minus the escape fraction, for a cylinder of refractive index $n = 1.5$ is displayed graphically in Figure 2.9. The

trapping efficiency of a cylinder is worse than a planar geometry, which is 75%, unless the photon is emitted at the cylinder's edge.

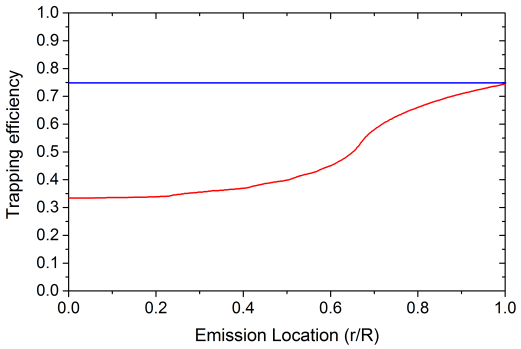

Figure 2.9: The trapping fraction from an infinite cylinder as a function of emission location r/R, shown in red, where r is the distance from the centre of the cylinder and R is the radius of the cylinder. The trapping efficiency of an infinite planar geometry is shown in blue. Data to make this graph is taken from McIntosh *et al.* [208]

Edelenbosch *et al.* further found that by taking into account the fact that luminophore self-absorption losses are a short range effect, the increase in photon concentration by increasing cylinder length is larger than the loss due to host material absorption and scattering. In effect this means that the effective concentration increase can be theoretically limitless.

Materials other than Lumogen F Red 305 have been used in CLSCs. Wu *et al.* use a lanthanide luminophore $Eu(TTA)_3Phen$, which experiences no re-absorption losses due to its greater than 200nm Stokes Shift. It was shown that it outperforms organic luminophores, in this case Rhodamine 6G, only when the geometric concentration C_G was over 75. The PLQY of both materials were not disclosed [210]. Correia *et al.* used the same $Eu(TTA)_3Phen$ luminophore, with a PLQY stated to be one of the highest reported so far in lanthanide based luminophores [211]. Both papers made the point of negligible re-absorption losses, underlining the need to use low light attenuation host material to keep up the transport efficiency of luminescent light.

Inman *et al.* made lead sulphide (PbS) QD CLSCs in both solid and hollow form [212]. These QD do suffer from re-absorption, however the interesting finding was that optical efficiency values for hollow CLSCs were double that for the solid CLSCs, caused by higher incident absorption and lower re-absorption losses. Looking at results from Wang *et al.* confirms that it is the hollow geometry alone that has these benefits [213]. In comparing modelling results from homogeneously doped and coated CLSCs, it was shown that re-absorption losses are higher in coated CLSCs. These losses are countered by the escape cone losses of a solid cylinder, meaning a cylindrical coated CLSC outperforms homogenously doped CLSCs. This agrees with modelling results by Edelenbosch *et al.* [69].

CLSC designs have morphed into fibre geometries, with small radii and long lengths. We can call these fibre LSCs (FLSCs). Banaei *et al.* designed a series of FLSCs for intercomparison [214]. These fibres were clear with doped centres. The most interesting shape is a square fibre, and its doped centre, with a semi-cylindrical top to focus light into the doped centre. With this configuration they produced an optical efficiency of $\mu_{opt} = 5.7\%$, albeit from a FLSC 2.5cm long.and 0.6mm in diameter. Extending the FLSC length to 10cm gave it an optical efficiency of $\mu_{opt} = 3.1\%$ [215]. Incident light on these FLSCs were normal to the fibre. It should be noted that the focussing characteristic of the tops of these fibres will not work for most of a day where incident light will not be normal the FLSCs. The authors however did propose further investigation for performance in diffuse light conditions.

For all the work mentioned, none measured the LSCs' performance in an array or in the outdoors. Only one cylindrical FLSC array has been investigated on in the outdoors. This FLSC array was part of a daylighting setup mentioned in subsection 1.2.1 with a room illumination output of 60Wm^{-2}, and was monitored for a whole month. This is also the only paper to investigate the performance of a

large scale FLSC array [66, 67].

2.5 Other solar uses for luminescent materials

Luminescent downshifting of incident light in algae photobioreactors to match the algae's peak absorption wavelengths has already been discussed in subsubsection 1.4.3.2.

There are two reports whereby a solar cell is embedded inside a luminescent plate [216, 217]. Yoon *et al.* use a micro silicon solar cell embedded in the luminescent layer of a coated LSC with a back mirror for the concept of a flexible LSC system. This solar cell absorbs light from all sides, therefore absorbs incident and luminescent light [216]. This is depicted in Figure 2.10a. The maximum improvement on the maximum power output was 3.2 times more than if the cell was just illuminated on the top surface.

Corrado *et al.* use a similar concept of embedding a solar cell within the luminescent layer, but instead the solar cell and luminescent layer are on the back surface of the waveguide [217]. This is depicted in Figure 2.10b. Variations on LSC size as well as PV number and orientation within the LSC were tried. The largest module built was 51 cm x 51cm, demonstrating true module-scale testing. The module was

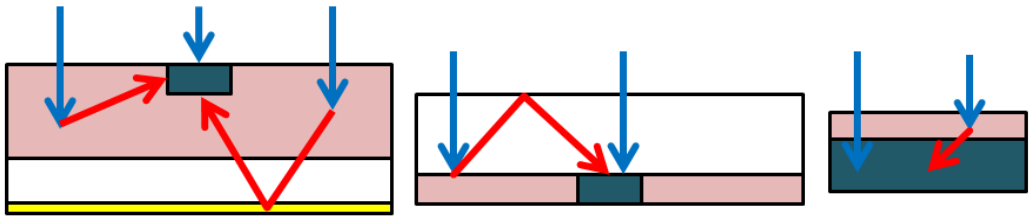

(a) (b) (c)

Figure 2.10: Different methods of using luminescence to improve solar cell performance. (a) A μmm silicon solar cell embedded into a luminescent layer with a specular mirror (yellow) under the substrate. The cell absorbs light from all surfaces. [216]; (b) Silicon solar cells embedded into a bottom luminescent layer. Only the top surface absorbs light [217]; (c) luminescent layer coated onto a solar cell

tested outdoors flat, and tilted towards the sun, where it was shown that tilting the module increases its relative efficiency by 6%. The best configuration of this design provided a lower cost per watt ($1.52/W) than using just standalone solar cells ($2.11/W).

A luminescent layer can be coated on the surface of a solar cell, downshifting incident light to more favourable wavelengths for the solar cell. This concept arose in tandem with the LSC in the 1970s and now this has been tried on a plethora of solar cell materials [218]. Not only does this luminescent down shifting layer have the ability to increase short circuit current in solar cells [219, 220], it is also seen as a way of making a solar cell more aesthetically pleasing as a way to better incorporate it into BIPV [221]. The major loss mechanisms that that have been identified in adding a luminescent downshifting to solar cell are reflection losses due to sub-optimal optical coupling between the solar cell and luminescent layer, light scattering due to surface roughness and light escape through the edges of the luminescent layer [181].

2.6 Conclusion

The luminescent solar concentrator (LSC) is a luminescent panel made of highly transparent glass or plastic, with homogeneously doped with, or coated with, luminescent materials. It is a light concentrating device that does not need to track the sun as it absorbs light isotropically, and the luminescent light can be matched to the uses of the LSC. Traditional figures of merit for the LSC are optical efficiency, which is the ratio of useful emissive photons and incident photons, and photon concentration, which is the ratio of useful photon flux and the incident photon flux.

The luminescent molecule, or luminophore, represents the major factor behind the LSC's performance. The ideal luminophore requires broad spectral absorption, high absorption coefficient, little or no overlap between its absorption and emis-

sion spectra to avoid re-absorption losses, high luminescent quantum yield. It must also be highly soluble in its host matrix material, its emission spectrum should be matched to the spectral response of the coupled photo-device, and it must be stable against degradation. It can degrade by damage caused by absorbing ultraviolet light as well as weathering caused by temperature fluctuations, wind, dirt and absorption of water over time. Current organic luminophores have high absorption coefficients, high luminescent quantum yields and stable. They suffer however from large spectral overlaps between their absorption and emission spectra and the emit light isotropically. This leads to significant optical losses as luminescent photons not within the angle range for total internal reflection escape out of the LSC top and bottom surfaces. For a waveguide of refractive index n=1.5, 25% of isotropically emitted luminescent light escapes due to this loss mechanism. This leads to fundamental optically efficiency limits of less than 10%. By adding anisotropy to luminophore light emission in order to ensure all luminescent light is emitted with in the total internal reflection angle range would raise this limit to 30%.

The most common waveguide materials are PMMA and borosilicate, and the refractive index of the LSCs can vary from n=1.5 to n=1.8.

Cylindrical geometries in LSCs provide a geometric alternative to flat plates. They can provide higher geometric concentration ratios, and whilst a cylinder array can provide less Fresnel surface reflection losses, trapping efficiencies are worse than planar geometries.

Other uses for luminescent materials include embedding solar cells inside LSCs, or coating them with a luminescent layer. This is to take advantage of luminescence downshifting, where incident sunlight is spectrally downshifted into a more suitable wavelength for the solar cell.

Chapter 3

Experimental and Computational Methods

This chapter discusses the experimental methods used for the fabrication of LSCs, the characterisation of LSCs and solar cells. Computational methods are presented, with the raytracer pvtrace introduced, and an expansion of is capabilities is presented.

3.1 Raytrace modelling

Pvtrace [163] is a Monte-Carlo raytracing model in Python2.7, written by Dr. Daniel Farrell [163]. It has been used to model a LSC using phycobilisomes as luminophores, with simulation results agreeing with experimental results on concentration ratios of varying LSC dimensions [222]. Krumer *et al.* have also matching results between pvtrace and experimental measurements of absorption through a luminescent medium [223]. Pvtrace has been used to demonstrate that nanorod luminophores experience less self-absorption losses than quantum dots [224].

The raytracer traces individual photon paths through the constructed geometry in a model environment, using Monte-Carlo processes to determine the outcome of

events at each intersection with an object's surface. In other words, probabilities of each physical process are compared to a randomly generated number to determine the outcome. Each interaction the photon has with its environment is logged in a database file using Structured Query Language (SQL), which is a programming language designed for managing data in a database management system[225].

3.1.1 Pvtrace algorithm

Incident photons are generated at a position with a direction determined by the nature of the light source. The wavelength is sampled from the input incident light spectrum. Original light sources include planar light sources and isotropic point sources.

At an interface with an object, the probability of Fresnel reflection is calculated for the given refractive indices and angle of incidence. This is compared to a random number to determine whether it is reflected or refracted. If it is reflected and has no more objects with which to intersect, the photon is stopped and its journey is logged. If it is refracted, Snell's law applied and the photon direction is updated. The next interface intersection point is found. The path length between these two intersection points is calculated. The absorption path length is also calculated using the Beer-Lambert law, dependent on the photon's wavelength and the object's optical coefficient at that wavelength. The two path lengths are compared to determine whether the photon is absorbed or if it hits the following interface. If the photon hits the following interface, the interface calculation starts again. If the photon is absorbed, based on the PLQY of the material, it is either re-emitted at a probabilistically determined redshifted wavelength, or lost non-radiatively. Re-emitted photons then follow the same interface calculations. An algorithm flow schematic is shown in Figure 3.1.

Every photon will undergo iterations of the same interface calculations until

it is lost non-radiatively or until it has escaped the objects in the model. At the end of its run, the photon has details logged such as the amount of times its been absorbed, how many interface interactions it has had, if it escaped the scene, from which object and which of its surfaces, and in which direction it escaped from. Datalogging is stored using SQL.

3.1.2 Parallelising pvtrace

Monte-Carlo raytrace modelling can be separated into a number of parallel sub-simulations due to each photon being an independent process with no interaction or communication with any other photons. This characteristic of a task is defined as an *Embarassingly Parallel* task [226]. Pvtrace in its current ability did not have parallelising capabilities, therefore only one logical core in a computer is used in a simulation. Most modern computers have at least four logical cores, meaning most of the available processing power is wasted. A significant amount of incident photons are needed in order to reduce the variability in simulation results for any given parameter space. Furthermore increasing the complexity of a LSC system increases the number of interface interactions and therefore simulation times increase. This can be a deciding factor in how many photons are used for a raytrace run.

ParallelPython (pp) is an open sourced parallelising module available for Python 2.7 [227]. This module was incorporated into pvtrace to establish parallelising capabilities. Shown diagramatically in Figure 3.2, the strategy is to split one simulation into various smaller sub-simulations. The resulting SQL files are merged into a master SQL file once all sub-simulations are finished. For a computer with large numbers of cores, the speed bottleneck becomes the read/write speed of the hard drive. RAMdisk software was purchased from Dataram [228]. This allows a chosen percentage of a computer's RAM to be used as a disk drive, albeit with superior read/write capabilities.

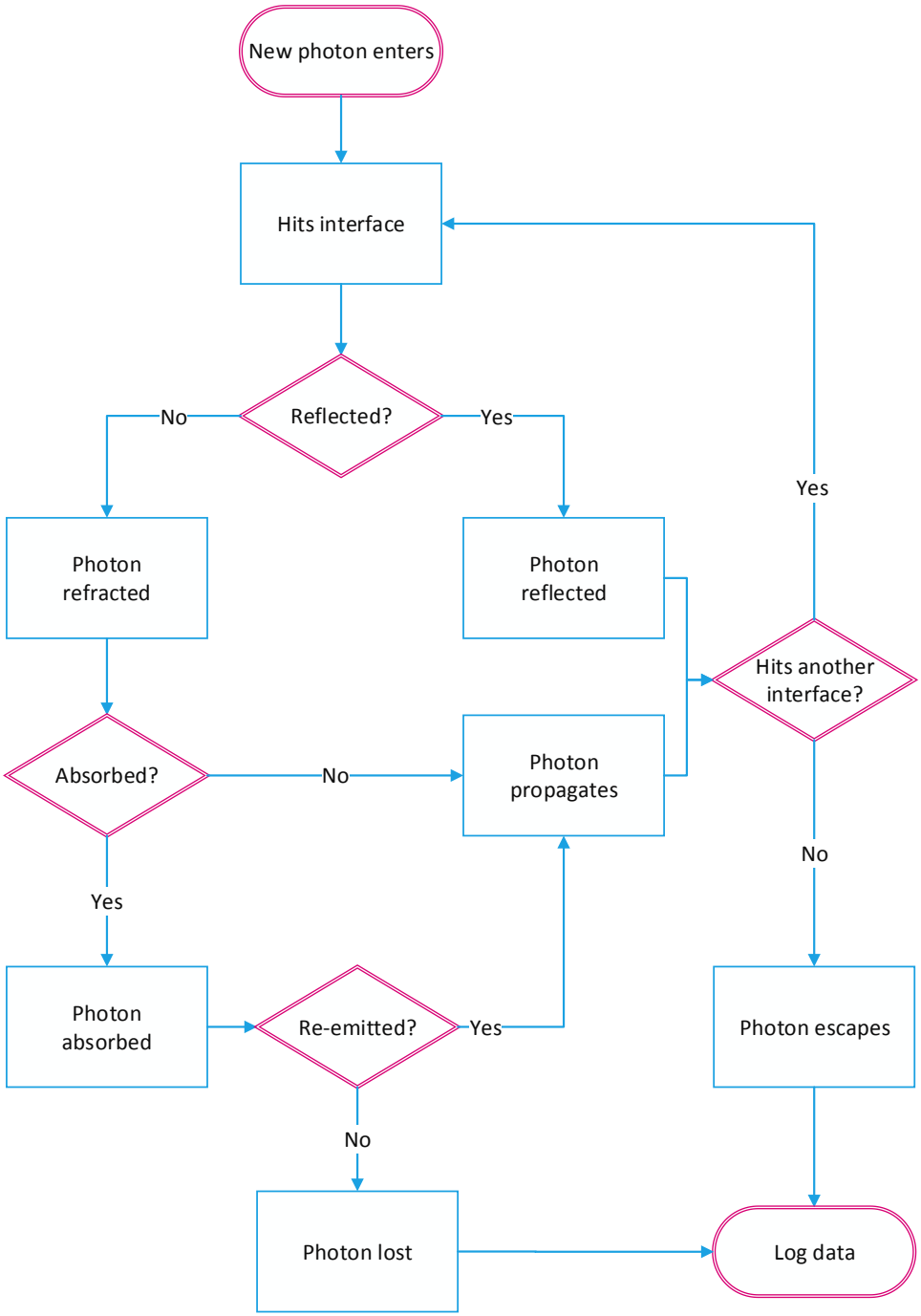

Figure 3.1: Algorithm flow diagram of a photon in pvtrace.

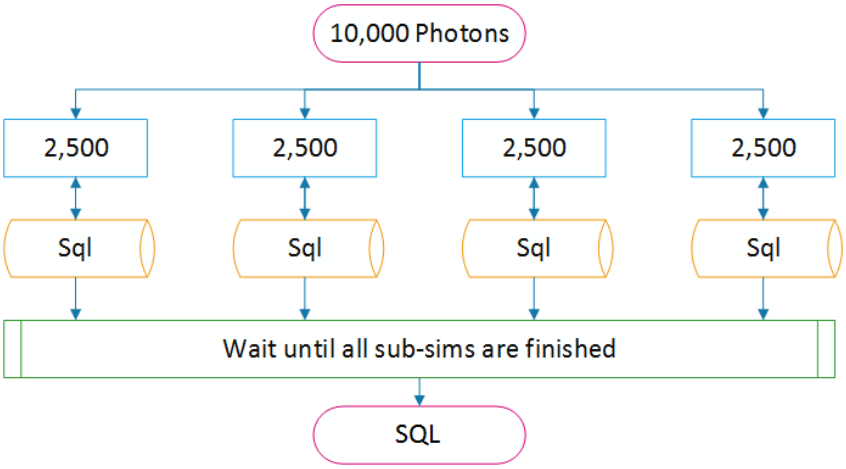

Figure 3.2: Parallelising strategy for pvtrace with a computer of four logical cores. A major 10,000 photon simulation gets split into four equal sub-simulations. Each SQL file can only be accessed by its own separate sub-simulation. Once all sub-simulations are finished and their SQL files are closed, the data gets compiled into one major SQL file

3.1.2.1 Simulation Benchmark Speeds

A summary of the benchmark speeds for a 16,000 photon simulation of a 20cm x 20cm x 0.5cm thin-film LSC with a back reflector and mirrors on 3 sides are shown below in Table 3.1. The computer used is a HP Z820 workstation with 16 logical cores. Using parallel-pvtrace on a RAMdisk shortened the benchmark simulation from 16 hours to 1 hour.

PVTrace iteration	duration
1 core hard drive	16h
8 core, hard drive	5h 56m
16 core, hard drive	4h 39m
16 core, RAMDisk	59m

Table 3.1: Simulation benchmark speeds. The final outcome of parallelisation has sped up PVTrace by 16 times.

3.1.3 Additions to pvtrace Geometry module

Additions were made to pvtrace in various modules in order to create the various models as shown in the results sections. Already existing modules and classes

will not be discussed here.

Simple Cone

The cone is used to model a reflecting cone used in the PEC reactor waveguide in subsection 5.1.1 and the Luminescent Solar Diffuser (LSD) in subsection 6.1.2. Resources used to create this geometry are by online by David Eberly [229] and by using the Graphics Gems book series [230, 231]. To define the cone, a vertex V and an axis ray is assigned, with the axis ray origin being V and unit vector D. An acute cone angle $\theta \in (0, \pi/2)$ is given. A point X is inside the cone when the angle between D and $X - V$ is in $[0, \theta]$. An infinite plane intersects the cone normal to the axis ray at a cone height H from the vertex, to be the cone's base. Containment of point X inside the cone, which includes a point on the cone surface, is defined by:

$$D.\frac{X-V}{|X-V|} \geq cos(\theta) \tag{3.1}$$

and includes determining the point X is within the cone height:

$$D \cdot (X - V) \leq H \tag{3.2}$$

Truncated Cone

This is used to model the unsuccessful creation of a LSD using truncated cones, discussed in subsubsection 6.1.2.1. The raytracing script to define a truncated cone is similar to that of a simple cone, except two infinite planes intersect, one for the base, and one for the top. This means the height constraint is defined as:

$$h \leq D \cdot (X - V) \leq H \tag{3.3}$$

Polygon Mesh

This uses the existing Polygon class, which defines a polygon as three or more points which are all in plane. Identifiers for the object revolve around determining firstly

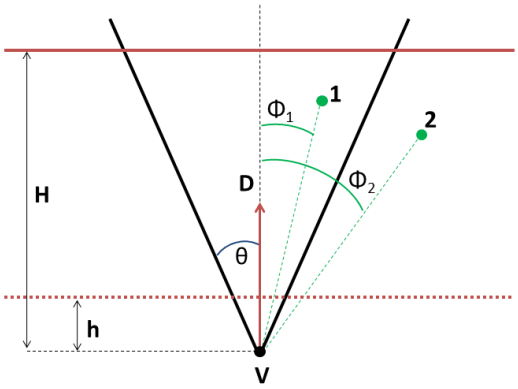

Figure 3.3: Pictorial representation of the Cone code. A vertex V is the cone point. The axis ray originates at V and has a unit vector D. The base is given by an infinite plane (solid red line) intersecting the cone normal to the unit vector D at a distance H away from the vertex. A truncated cone includes a second infinite plane (dotted red line). Point 1 is inside the cone as $\phi_1 < \theta$ and is between the point V and infinite plane, and point 2 is outside the cone as $\phi_2 > \theta$.

whether a photon is on the plane of the polygon, and secondly if it resides in the middle of the points. Being a 2-dimensional object, a photon cannot be contained within it.

The polygon mesh is used to model the successful creation of a LSD. A collection of polygons are created via a desired function. PolygonMesh does not check if the polygons form an enclosed mesh, so either the function should be of a self-contained nature, or if the mesh is created in parts it needs to be verified on the pvtrace visualiser. All the polygons are interpreted as one object. A ray is a point X with a unit vector U. Containment of a point X in the Polygon Mesh is determined by finding the number of Polygons in which the ray intersects with. If the number of intersected Polygons are odd, point X is inside the PolygonMesh, if it is even then it is outside.

This works in tandem with a new module, MeshGen (mesh generator), which contains the functions that create the polygon structure. This module is discussed in further details in subsection 6.1.2.

3.1.4 Additions to pvtrace LightSources module

SunPositionSource

The sun's zenithal and azimuthal are fed in. The north is set to [1,0,0] and the ground normal is set to [0,0,1]. The point of illumination is determined like the Planar source, choosing a point within an x-y parameter space by random number generation. Incident planar light is given a direction assigned by the inputted zenithal and azimuthal angles.

PlanarCircularSource

The same as the Planar light source, except the parameter space for the point of illumination is defined by a circle of centrepoint C and radius r. This is used to illuminate 3D circular LSD models.

HemiSource

A hemispherical light source to simulate diffuse light conditions. The ground normal is set to [0,0,1] and north is set to [1,0,0]. The point of illumination is defined as above. Incident photon directions are randomly generated within the limits of $0 \leq \theta \leq \pi/2$ for the zenithal angle and $0 \leq \phi \leq 2\pi$ for the azimuthal angle.

3.1.5 Additions to pvtrace Materials module

Algae

The Materials class is modified to include an Algae scattering parameter. The extinction and absorption spectrum of algae is fed into the Materials class. If the algae scattering parameter is False, it is business as usual for the Materials class and the algae is treated as a normal material absorptive material with zero luminescent quantum yield.

If the algae scattering parameter is True, then the extinction spectrum is fed into the Material absorption spectrum parameter. Thus the extinction coefficient in this

case determines whether a photon impinges on the algae. Scattering/absorption is then defined. The photon is decided as being absorbed if the following outcome is true:

$$n_{random} < \frac{\alpha_{abs}}{\alpha_{ext}} \tag{3.4}$$

where n_{random} is a randomly generated number between 0 and 1, α_{abs} is the absorption coefficient and α_{ext} is the extinction coefficient at the wavelength of the absorbed photon. If the above definition is False, the photon is scattered. The code treats the algae as an isotropic emitter and the photon experiences zero redshift.

3.1.6 Additions to pvtrace Trace module

ppstart

This enables pvtrace to be parallelised. The number of sub-simulations is determined either manually, or by automatic identification of the number of logical cores on the computer. The sub-simulations are started and when all are finished, all the SQL database files are merged into a larger one. The large combined SQL database includes all six log tables: Photon, Position, Direction, Polarisation, Surface_Normal and State. A loop is run through the list of sub-SQL files to copy and paste values from their six tables into the merged tables. The start class has been modified to accommodate ppstart functionality by assigning each sub-SQL file a number defined by its order in the parallelising start queue.

3.1.7 The new MeshGen module

This module is the part that generates the mesh from a parametric equation. The base logic is inspired from description of generating parametric surfaces from the "Mesh Generation with Python" page on the the website "The Little Grasshopper" [232].

MeshGen takes three main arguments: the function object that the latitudinal

coordinate resolution, the longitudinal coordinate resolution. The function builds a list of polygons which is then given to the PolygonMesh class and treated as one object.

Depending on the objective function, the mesh generation module will not produce a closed mesh – it might be necessary to manually add two polygons at either end to close the mesh. The PolygonMesh object does not care how many vertices its polygons have and can take a mixture. Current MeshGen definition code creates 3-vertex polygons.

The current MeshGen module only contains the plateau curve mesh to form a hyperboloid LSD, and the corresponding algae slice mesh that wraps around the hyperboloid LSD. The mesh is described in more detail in subsection 6.1.2.

3.1.8 Genetic algorithm

A genetic algorithm (GA) is a method of multi-parameter optimisation, which attempts to emulate simple models of genetic evolution over a set number of generations, ranking members of a population on their overall fitness which is described by a pre-defined fitness function. Each generation of a population experiences genetic selection, crossovers, and then mutation as a way to develop the fittest member [233]. The number of members in a population can be varied according to the number of parameters that need optimising.

3.2 Fabrication of LSCs

3.2.1 Thin film LSCs

Thin film LSCs (TFLSCs) are LSCs consisting of a transparent waveguide which coated with a highly doped luminescent layer consisting of a host matrix and luminophore. Solution-based processing is used to fabricate them. A lu-

minophore/host material/solvent mixture is created and then deposited onto a transparent waveguide substrate.

3.2.1.1 Luminescent solution

Standard glass vials from VWR are used for making solutions. They are first cleaned by sonication in acetone, degreased with isopropanol (IPA) and rinsed with de-ionised (DI) water before being left to dry.

Using a micro balance with 10^{-4} gram accuracy, the required quantity of host and luminophore material are added to the vial. The host material used in this thesis is polymethyl methacrylate (PMMA), which has a refractive index of 1.49. It is bought from Sigma Aldrich.

A solvent is added to the powder mixture. Chlorobenzene or toluene are suitable solvents, however they are flammable, acutely toxic, irritant and harmful to the environment. For this reason any handling of solvents must be done in a fume hood. Arms should be covered, and protective nitrile gloves used. Total dissolution can take 4-10 days, depending on the size of the vial and the molecular weight of the PMMA. Stirring with magnetic stirrers speeds up the dissolution process, as does homogeneously heating the vial.

3.2.1.2 Thin film coating

Blade coating is the preferred method of depositing a thin film on a substrate. A RK Control Coater from RK Printcoat Instruments was used. Substrates of up to 18cm x 18cm can be coated with this machine. The height of the blade is controlled with micrometer dials. Film thickness resolution is 1μm. This technique needs a large excess of luminescent solution for complete coating of a substrate, as demonstrated in Figure 3.4.

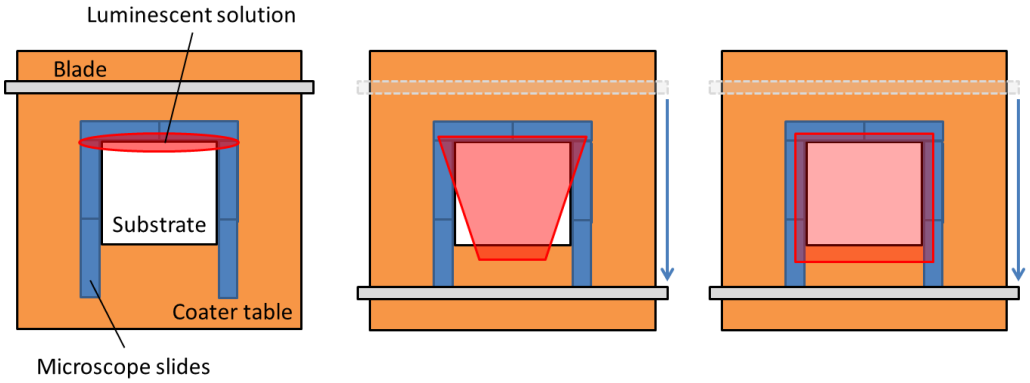

(a) Initial setup for coating (b) Partial thin film coating. (c) Full thin film coating

Figure 3.4: Blade coating luminescent solution onto a substrate. Microscope slides surround the substrate. A large amount of luminescent solution is deposited on the substrate edge nearest to the blade. Insufficient amounts of solution result in an incomplete coating of the substrate as demonstrated in (b). Complete coating is shown in (c).

Glass substrates are cleaned with acetone, IPA and DI water. The substrate edges are protected with protective adhesive tape and microscope slides are placed all around the substrate. PMMA substrates are not cleaned with solvents as they will dissolve and lose surface uniformity. An excess amount of luminescent solution is placed on and around the substrate edge closest to the blade. Insufficient amounts of solution result in an incomplete coating of the substrate, as demonstrated in Figure 3.4b. The corners of the substrate furthest from the blade's starting point can be left uncoated as the luminescent layer becomes more narrow as the blade passes over the substrate. This effect is more pronounced with more viscous solutions.

After coating the TFLSC is left in the fume hood overnight for the solvent to evaporate out of the thin film. The blade coater table and the blade are cleaned rapidly with chlorobenzene and acetone before the solution dries on them.

3.2.2 Fibre LSCs

Cylindrical, homogeneously doped PMMA/Lumogen F Red 305 FLSCs were fabricated at Nanoforce Ltd, which is based at Queen Mary University of London

(QMUL), with guidance from Dr. Emiliano Bilotti. The mix was melt-blended in a twin-screw micro-compounder (DSM Micro15). Fibres were drawn through a die in the solid state under tension by a rotating drum and air-cooled. The rotation of the drum determined the diameter of the fibres. The fibres were thin enough that air cooling was sufficient to cool them down to room temperature within tens of seconds. The setup meant that the maximum diameter of the fibres were limited to 1mm. Figure 3.5b shows the fibre manufacturing in action.

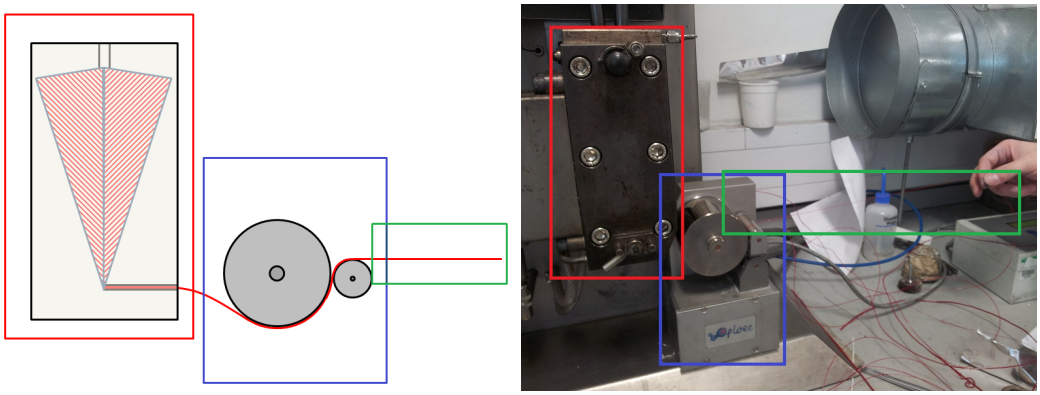

(a) Schematic (b) Photograph

Figure 3.5: Fibre extrusion at Nanoforce in Queen Mary University London, with the guidance of Dr. Emiliano Bilotti. PMMA and Lumogen dye was melt-blended in a DSM Micro15 twin-screw micro-compounder (red box). A rotating drum draws out fibres from the extruder exit hole (blue box). The rotation speed determines the diameter of the fibre. The fibre is then air-cooled (green box).

3.2.2.1 Difficulties in manufacturing larger fibres

Attempts were made to manufacture fibres of diameters larger than 1mm. A larger single-screw melt-compounder, Collin Teach-Line E20T, enables fibres of diameters of a few millimetres to be manufactured. The same PMMA as used in the micro-compounder was also used in the extruder.

First, fabricating pure PMMA fibres was attempted. The fibres came out brittle with many air pockets and extremely rough surfaces, as shown in Figure 3.6. A hypothesis was made that there was too much moisture in the PMMA, so the PMMA

powder was dessicated overnight in an oven. This aided in slightly removing air bubbles from the fibres, but the surface was still very rough. A further hypothesis was made in there being contaminants from the previous fibre extrusion that were interfering with the melt-blending of the PMMA, so a thorough clean of the system was undertaken. This too did not improve the surface roughness. Throughout these attempts, blending temperatures and blending/extrusion speeds were varied across a broad range.

The conclusion to this is that the PMMA used for mini-extrusion is not necessarily compatible with larger scale melt-compounding. Different polymers capable of being host material to Lumogen F Red 305 would have to be experimented with in the single-screw melt-compounder to determine the more compatible for the process. Time constraints prevented further investigation into this issue.

Figure 3.6: Fibres produced from the larger single-screw melt-compounder. The fibres were brittle, had air pockets within, and very rough surfaces.

3.3 LSC characterisation

A Steuernagel Lichttechnik solar simulator is used as an incident light source, with the lamp source being a metal halide HMI 575W/SEL XS bulb and a ho-

mogenising filter. An Ocean Optics HR4000 fibre spectrometer is used to measure the transmission and emission spectra of an LSC. The transmission spectrum of luminescent material is used to obtain the absorption spectrum, which is fed into the raytracer, pvtrace.

3.3.1 Luminophore absorption spectrum

The absorption A of a material is determined by:

$$A = 1 - T - R \tag{3.5}$$

where T is the transmission of a material and R is the reflectance. Transmission measurement can be used to obtain the absorption spectrum for luminescent material.

The spectrometer's fibre end is mounted facing into the solar simulator spectrometer. A similar substrate used for the LSC is placed in between the aperture and the fibre to measure the transmission spectrum of the substrate I_{sub}. The substrate is replaced with the LSC to obtain its transmission spectrum I_{LSC}. The transmission of the substrate is measured and subtracted to remove the absorption characteristics of the substrate. Comparing light intensities between a substrate and the LSC removes reflectance as both should have the same reflection characteristics.

The Beer-Lambert law is used to obtain the absorption spectrum of the luminescent material **??**:

$$T = \frac{I_{LSC}}{I_{sub}} = e^{-\alpha l} \tag{3.6}$$

where T is the transmission, I_{lum} is the light intensity of the light transmitted through the luminescent layer, I_{sub} is the incident light spectrum with the substrate, α is the absorption coefficient of units m^{-1} and l is the luminescent layer thickness.

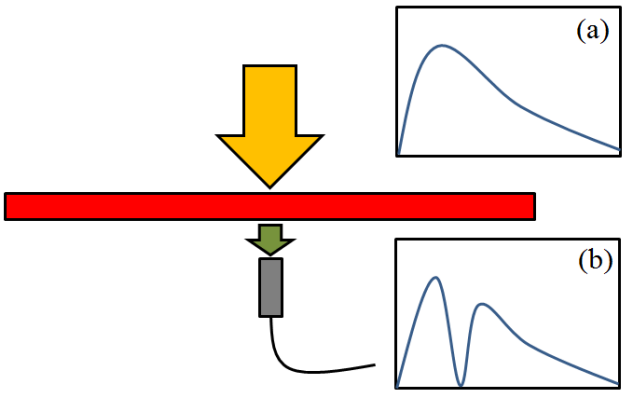

Figure 3.7: Measuring the transmission spectrum of a LSC. The transmission spectrum (b) is subtracted from the incident solar simulator spectrum (a) to obtain the absorption spectrum of the LSC.

The Beer-Lambert law is applied to every wavelength measured by the spectrometer to obtain an absorption spectrum. Obtaining solely an absorption spectrum for pvtrace means the absolute value of absorption is not necessary.

3.3.2 Luminophore emission spectrum

The light emitted at the edge of the LSC is redshifted from the original emission spectrum of the luminophore due to re-absorption and re-emission along the waveguide. Measuring the emission from the top surface of the LSC is needed to obtain an unaltered emission spectrum. A laser with a wavelength shorter than that of the luminophore's emission spectrum is used to excite a spot on the LSC surface. The fibre spectrometer is used to obtain the emission spectrum.

3.4 Solar cell photoluminescence

Under open-circuit conditions and when excited with light of an energy above the bandgap energy, a solar cell will become luminescent. Much like luminophores, incident light excites an electron in its electronic ground state into the conduction band. Electron-hole pairs are generated, and thermalise down to the lowest energy level available in the sample before recombining radiatively. A spectrometer monitors the emitted light spectrum. A schematic of the setup is shown in Fig-

ure 3.8. A Spectra Physics Millenia V laser, producing light of wavelength 523nm was used as the excitation source. A Princeton Instruments Acton 2500 was used as the monochromator. The laser light is optically chopped to give pulses of a given frequency. As such the photoluminescence from the sample pulses with that frequency. A lock-in amplifier receives the chopping frequency and locks onto the signal from the detector which pulses at that frequency. Continuous signals are considered noise and removed.

3.4.1 Top surface emission

The standard solar cell PL characterisation is made with top surface emission. The setup is shown below in Figure 3.8.

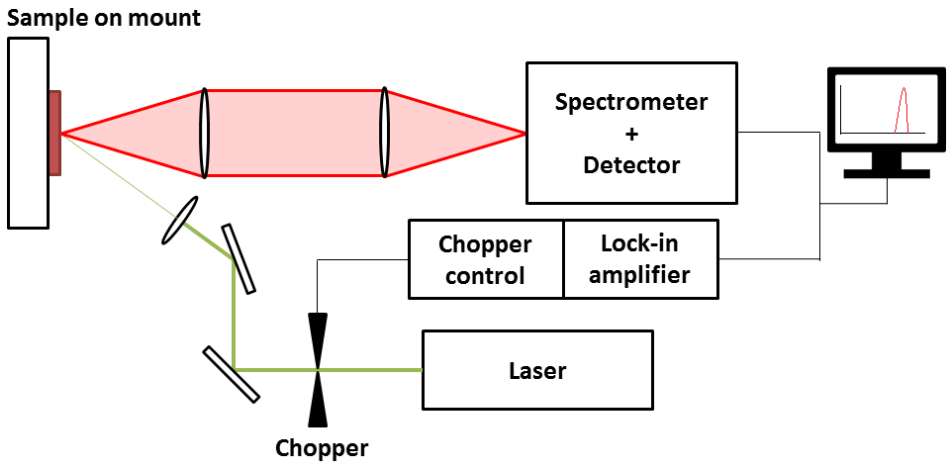

Figure 3.8: Schematic of a photoluminescence (PL) setup. 532m laser light excites the sample. Carriers are generated and then recombine radiatively to photoluminesce. This PL is detected by the spectrometer.

3.4.2 Edge emission

The intensity out of the edge of a quantum well solar cell is measured. Unchopped laser light is de-focussed with a lens to so that the whole top surface of a PL sample is illuminated. The profile of the illumination is Gaussian, with the beam width considered to be its full width half max. A CCD is placed where the

sample is to be, and an intensity profile of the beam is captured. The dimension of each pixel is known, thereby the physical width and spot area can be calculated. This is shown in Figure 3.9. Knowing the power of the laser, incident power density in Wm^{-2} is obtained.

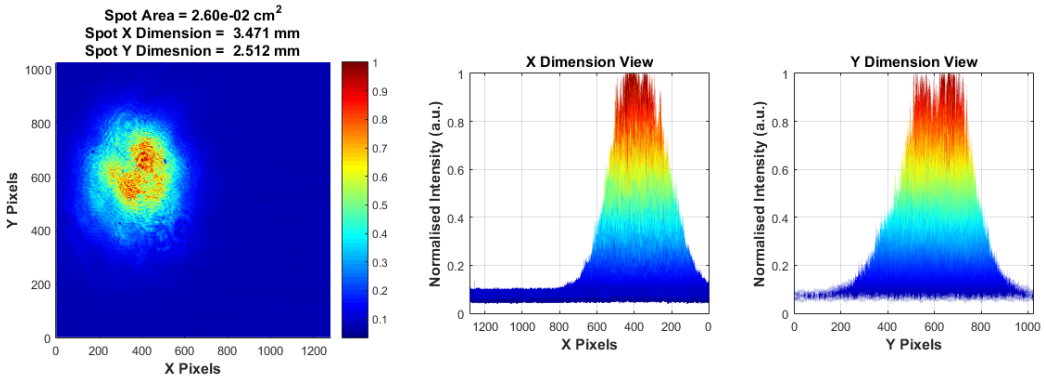

Figure 3.9: Calculating the illumination area of a de-focussed laser beam. The beam width is taken as the full width half max of the beam.

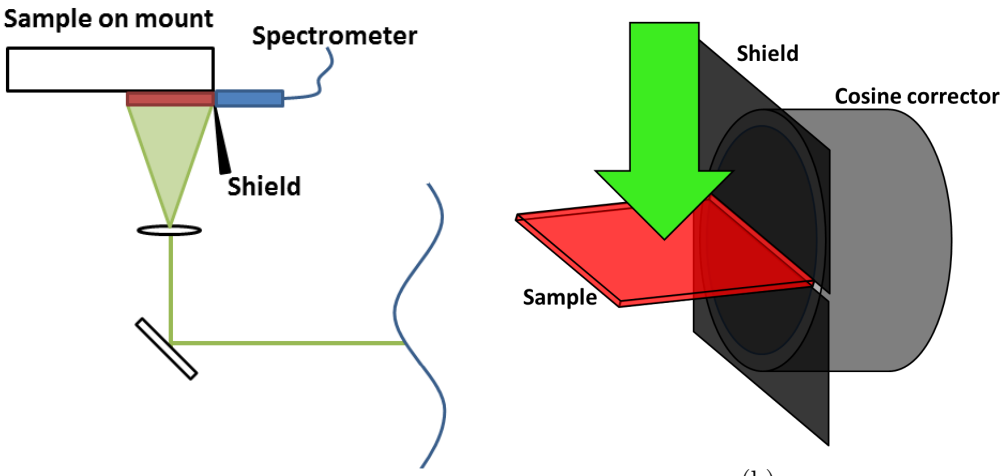

(a) (b)

Figure 3.10: Measuring the intensity of the edge emission of a solar cell under full surface illumination, with a calibrated spectrometer. The PL sample width and the cosine corrector aperture diameter are both 5mm. Black tape, acting as a light shield, covers the parts of the cosine corrector aperture not coupled to the PL sample edge. The setup is shown including the lens (a) and in a close-up of the sample coupled to the cosine corrector (b).

An Ocean Optics HR4000 fibre spectrometer is used. The fibre end has a cosine

corrector (CC), which is an optical diffuser that enables signal collection with a 180° field of view. The CC's aperture width is 5mm and the PL sample's width is 5mm. The sample edge is placed onto the middle of the CC aperture, and black tape is added to the rest of the aperture to shield it from incident and stray light. Light emission from the whole of the PL sample's edge is collected. Some PL from the top surface, exiting at near-right angles to the surface could potentially reach the fibre aperture, so great care was taken to a) have a perfectly straight shield and b) ensure a flush placement of the shield on the top surface on the sample. The setup is shown in Figure 3.10a.

The spectrometer was calibrated by Ocean Optics for spectral irradiance, giving a spectrum with units $\mu W cm^{-2} nm^{-1}$. This calibration was then corrected by Dr. Diego Alonso-Alvaréz at the 5th International Spectroradiometer and Broadband Intercomparison 2015 (Torrejón de Ardoz, Spain 17th-22nd May 2015).

3.5 Experimental high concentration illumination measurements

The following high concentration illumination experiment was undertaken at the Swiss PV Module Test Centre, at the University of Applied Sciences and Arts of Southern Switzerland (SUPSI). The setup and measurements were all made with Dr. Mauro Pravettoni.

3.5.1 Cone in a waveguide

3.5.1.1 Physical setup

The waveguide is placed vertically on a dedicated-made mount. An opaque shield covers the front of the waveguide bar an aperture in which to illuminate the cone. A backbar presses the waveguide into the shield for secure fixation. The spectrometer fibre, which has a cosine corrector on the end, is placed at the edge

and at the centre of the waveguide. The setup is shown in diagrammatic form in Figure 3.11 and in photographs in Figure 3.12.

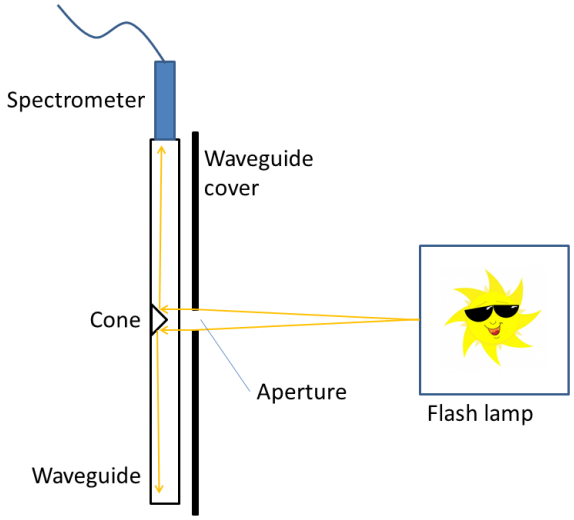

Figure 3.11: Schematic of high intensity illumination setup for a cone in a waveguide. A high intensity flash lamp illuminates the waveguide. An opaque shield covers the front of the waveguide apart from a small aperture for the cone. A spectrometer with a cosine corrector and calibrated for absolute irradiance spectral measurements is placed on the edge of the waveguide.

The spectrometer used is a three-channel Avantes Avaspec fibre optic spectrometer. Each channel is optimised for its spectral band: 400-750nm for channel 1, 600-1000nm for channel 2 and 950-1600nm for channel 3. The high intensity flash lamp used is a modified Pasan IIIa with a Xenon bulb. A full description of the flash lamp along with a detailed uncertainty analysis can be found elsewhere [234]. The flash is stable for 1ms. The illumination profile as a function of time is shown in Figure 3.13b. The illumination intensity is measured using a crystalline silicon solar cell which had been calibrated under IEC60904-1 Standard Testing Conditions less than a year before this experiment.

Up to 2000 suns at peak power can be achieved close to the flash source. A variation of concentration values were investigated, which were determined by the distance of the waveguide away from the flash lamp. Figure 3.13a shows inverse square proportionality between illumination power and distance away from the lamp. The

concentrations investigated were between 20 - 1741 suns.

The back and edges of the waveguide are exposed. Background noise has to be accounted for in all spectra. Measured spectra for the cone in waveguide is subtracted by the background spectra for the relevant illumination value.

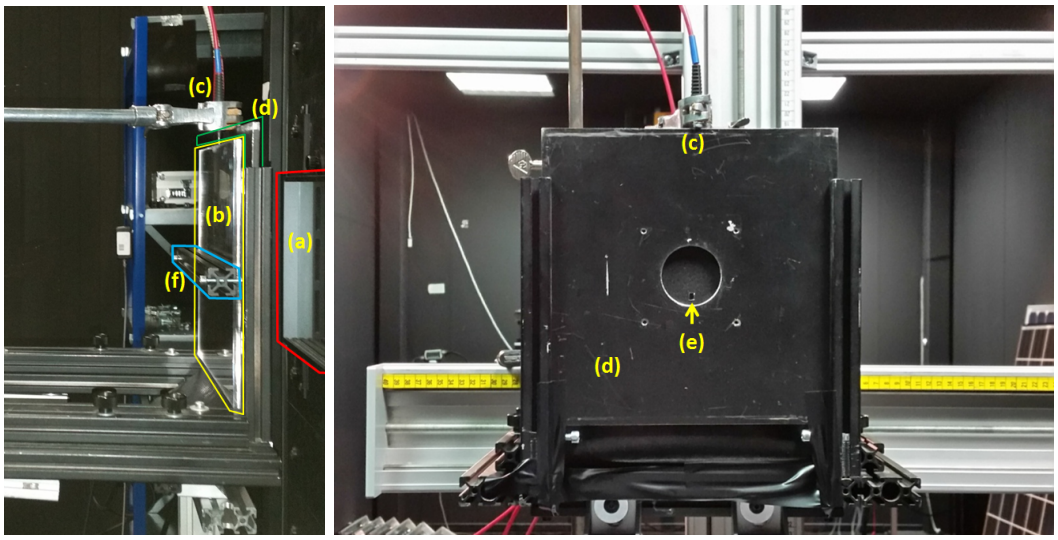

(a) Side (b) Front

Figure 3.12: Photograph of the high intensity illumination setup at SUPSI, Switzerland. The flash lamp (a) is highlighted in red. The waveguide (b), which is highlighted in yellow, has a calibrated spectrometer with a cosine corrector (c) on its edge. The front of the waveguide is covered by a shield (d), which is highlighted in green. It has a small aperture for the cone (e). The waveguide is held in place by a back bar (f), highlighted in blue, pressing it into the shield.

Location	Suns at max. power	Distance from lamp (m)	1/distance (m-2)
P5	1740.8	0.15	44.44
P4	909.6	0.21	22.68
P3	298	0.365	7.51
P2	117.7	0.57	3.08
P1	20	1.32	0.58

Table 3.2: The five distances away from the flash lamp and their respective power in suns. The $1/r^2$ relationship is shown graphically in Figure 3.13.

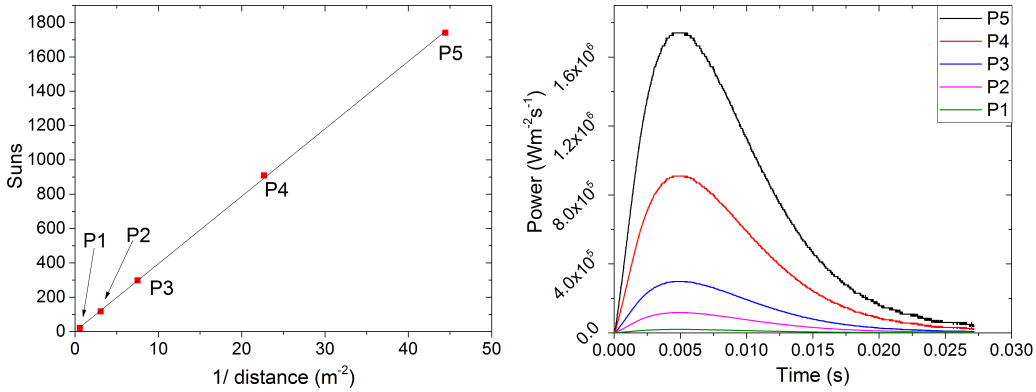

(a) Suns at max. power for each position. (b) Flash lamp power as a function of time.

Figure 3.13: Five positions away from the flash lamp are chosen. Max. power for each position shows inverse square relationship of light intensity and distance from light source. Peak power lasts for around 1ms.

3.5.1.2 Correcting spectrometer intensity values

The peak incident intensities given in Table 3.2 were calculated during the 1ms stable peak lifetime of the illumination pulse. The spectrometer could not be triggered with accurate timing to collect light only in this 1ms window.

The Avantes spectrometer was given a 50ms integration time, and is triggered just before the flash lamp is triggered. This is to ensure that all of the light from the 25ms flash is collected. The spectrometer assumes uniform illumination over time, and so gives an output of average spectral irradiance over the total integration time of 50ms (see Figure 3.14). The intensity values therefore given by the spectrometer are lower than they should be when the flash lamp at peak power. A scaling factor is needed for the spectrometer integrated intensity to obtain the real intensity value at peak flash.

One of the flash intensity vs time profiles from Figure 3.13b is used, and integrated over 25ms to give $Wm^{-2}(s^{-1})$. An arbitrary uniform profile with a lower intensity value than peak flash is created, and integrated over 50ms. An iterative solver is run that modifies the uniform value until the integration under the uniform

and the flash profile graphs match, so that both give equal values of Wm^{-2}. The scaling factor is the value needed to multiply the uniform value to obtain peak flash intensity, which for this particular setup was 4.527.

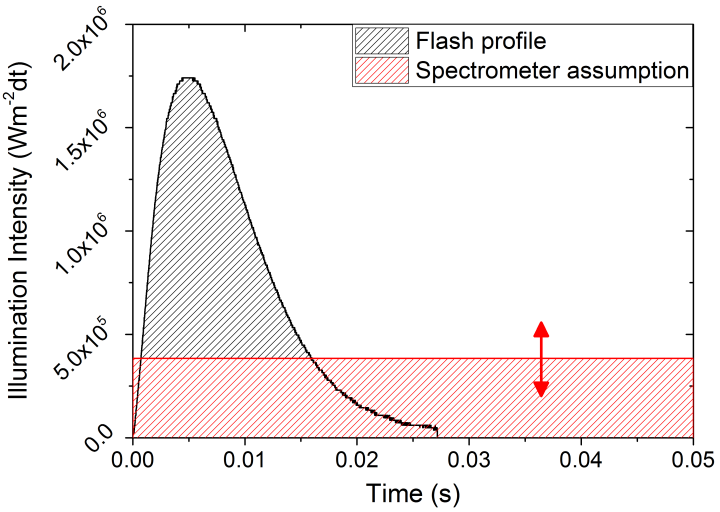

Figure 3.14: Flash lamp intensity and spectrometer assumed intensity vs time. The spectrometer assumes constant illumination over its integration time, which is double that of the flash duration. A scaling factor is needed on the spectrometer power value by matching the integration of both graphs (which gives intensity in Wm^2), in order to get the real intensity measured by the spectrometer at peak flash.

3.5.1.3 Calculating Watts in vs Watts out

The intensity in Wm^{-2} is known for incident illumination, and for the illumination impinging on the spectrometer. The area dependence must be removed so that an experimental efficiency value can be compared to a simulated efficiency value. Assuming uniform incident illumination, multiplying the intensity with the aperture area gives the incident power in Watts, W_{inc}.

The emission coming out of the waveguide edge is non-uniform, and depends on the type of waveguide-embedded reflective cone and whether the waveguide has reflectors along its edges. This is explained in more detail in subsection 5.1.1. The

spectrometer was not moved from its place in the centre of the waveguide. The assumptions made are for the spectrometer aperture to be a point exactly at the centre of the waveguide edge. The emission profile is integrated across the waveguide width, with the peak of the profile being the spectrometer intensity value, giving Wm^{-1}. Multiplying by the waveguide thickness gives the power out of the edge in Watts, W_{edge}. The power efficiency W_{edge}/W_{inc} can then be compared with results from the raytrace model in subsection 5.1.1.

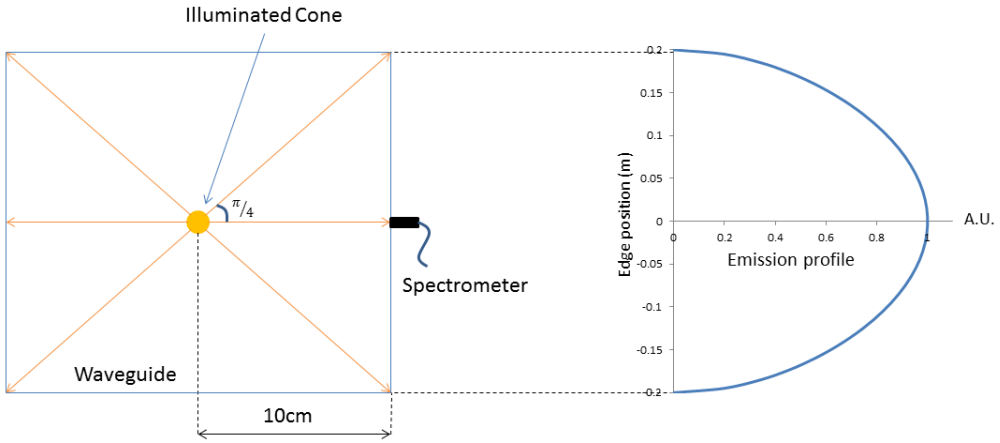

Figure 3.15: The emission out of the waveguide is non-uniform, and dependent on the emission profile of the cone, and on the existence of edge reflectors

3.5.2 Quantum well solar cell in a waveguide

3.5.2.1 Physical setup

The waveguide with a reflective cone is replaced with a waveguide with a square cavity, shaped to contain a quantum well solar (QWSC) cell sample. The setup is carried out as explained above in subsection 3.5.1. The cavity is flooded with index matching fluid (Cargille acrylic matching liquid, refractive index n=1.49 at 633nm) before embedding the QWSC. The same positions are used (P5 - P1) to measure photoluminescence (PL) from the waveguide edge.

As well as background light being able to enter the spectrometer aperture due to

the exposed back of the waveguide, scattered incident light off the top of the cavity also contributes to the total signal. The PL is isolated by subtracting the spectrum obtained when illuminating only the cavity to the spectrum obtained when a QWSC sample is in the cavity. This is described in further detail in subsubsection 5.2.4.1.

3.6 Conclusion

Thin-film luminescent solar concentrators are manufactured by blade-coating an excess of luminescent solution over the top of a transparent glass or polymer substrate. Fibre luminescent solar concentrators were manufactured at Nanforce Ltd by double-screw mini-extrusion. Attempts were made to make larger diameter fibres by single-screw extrusion, but the resulting fibres were brittle and had rough surfaces. A polymer that can be used in small scale mini-extrusion does not necessarily mean it is compatible for larger scale fibre manufacturing.

A fibre spectrometer is used to measure a non-redshifting emission spectrum of a LSC from the top surface. The absorption spectrum is obtained by subtracting the measured incident spectrum from the transmission spectrum of a LSC.

Photoluminescence spectroscopy is used to measured the luminescence of a solar cell when excited by a laser of photon energy above the cell's bandgap energy. The top surface emission is measured by a monochromator and photodiode. Edge emission is measured in absolute units of $\mu W cm^{-2} nm^{-1}$ by using a calibrated fibre spectrometer with a cosine corrector aperture in order to have a 180° field of view.

High concentration illumination experiments are undertaken at the Swiss PV Module Test Centre at SUPSI, Switzerland. A high intensity flash lamp is used, and the illumination intensity is determined by the distance of the sample away from the lamp. A waveguide containing either a reflective cone, or a quantum well solar cell (QWSC), is covered with a shield apart from an aperture over the cone or

QWSC. The light reaching the edge of the waveguide is measured by a 3-channel calibrated fibre spectrometer with a cosine corrector.

The raytracer used for modelling, pvtrace, is introduced, followed by a discussion on the expansion of its capabilities. Pvtrace is parallelised and a RAMdisk is used to cut simulations by 16 times when using a 16 core computer. New classes and a new module are constructed to simulate real world light conditions and new shapes. The module MeshGen is a mesh-making algorithm used to construct the luminescent solar diffuser.

Chapter 4

Cylindrical fibres and cylindrical LSC arrays

This chapter presents practical work made on fibre LSCs, and computational work on cylindrical LSCs. Using fibres manufactured at Nanoforce Ltd, the linear increase in photon concentration as a function of fibre length is demonstrated for lengths more suitable for large scale fibre arrays. Using pvtrace, a 2D demonstration of angle of incidence related light trapping is discussed, and a cylindrical LSC array is simulated with 3D real world light conditions for two separate days to discover whether this light trapping manifests as a performance boost. A significant part of this chapter has been published in paper DOI: 10.1364/OE.24.0A1188.

4.1 Determining a linear relationship with fibre length and light concentration

As discussed in subsubsection 2.3.2.3, reabsorption of luminescent light is a major loss mechanism in LSCs. Due to the fact that most re-absorption/re-emission events happen within the first few centimetres of a LSC, Edelenbosch *et al.* stated that in a cylindrical fibre LSC photon concentration has the ability to increase linearly with fibre length and waveguide surface defects and non-radiative host losses

becoming the major loss mechanism. They also stated, using results generated from pvtrace simulations, that the effective increase in photon concentration of a fibre LSC can be theoretically limitless [69]. Whilst 1.2m long fibre LSC arrays have been investigated in the literature [66, 67], a practical demonstration of these simulated results has not been attempted. The aim therefore is to confirm this prediction by measuring a fibre's photon concentration as a function of fibre length to determine whether the increase is linear.

4.1.1 Fibre details

Two different fibre LSCs are utilised: one made at Nanoforce Ltd, and a commercially acquired Lumogen Red F 305 fibre LSC from LasIRvis Optoelectronics Ltd. The Nanoforce fibres used have an uncertainty in their dye load concentration. Preliminary fibres were made at 2% concentration but then a 0.2% concentration dye/PMMA mix was added into the extruder hopper. After opening the extruder for post-manufacturing cleaning, it was seen that a lot of the Lumogen material had stuck to the extruder walls and screw. This would introduce inhomogeneity to the mixing as excess dye could detach from the extruder components and into the mixture. Furthermore the most radially-uniform fibres were made at a concentration slightly higher than the final 0.2%. This is seen by eye as the final fibres were more transparent than the more optimally manufactured fibres. The exact concentration was deemed to be unimportant as the objective of the chapter was merely to determine linear increase in photon concentration as a function of fibre length, not determine absolute photon concentration values.

Three fibres were manufactured with an estimated 0.5±0.25% dye load concentration. It is low enough to ensure minimal risk of luminophore agglomeration. This does not remove the risk of uneven spread of the dye within the host matrix during material mixing due to the reasons explained above. The fibres had average diameters of 0.64mm, 0.7mm and 1.12mm with lengths of up to 2metres. The fibres

suffer non-uniform variations that differ on average 0.18mm from the mean value across the length of a fibre. Variations in photon flux out of the fibre ends can occur due to the extent of fibre diameter inhomogeneity across its length, agglomeration of the luminescent material which can mitigated with a low dye load concentration, and the quality of polishing of the fibre ends.

4.1.2 Fibre measurements

To measure the light coming out of the FLSC ends, the fibres were coiled in a manner to avoid overlap, and therefore shading, under the Steuernagel Lichttechnik solar simulator. For the Nanoforce fibres, one end of a fibre, which was polished using Thorlabs polishing paper down to 0.3μm grain size, was clamped down by a fibre launcher and optically coupled to a silicon photovoltaic (PV) cell using index matching fluid (Cargille acrylic matching liquid, refractive index n=1.49 at 633nm), with the remaining area of the PV masked off as well as being enclosed in a light shield. The measurement being taken is the short circuit current J_{SC} of the silicon PV. Photon concentration C_γ is the ratio of outgoing to incident photon flux, and the incident photon flux stays the same throughout measurements, as such it will suffice to merely measure the increase in J_{SC} of the silicon PV as a function of fibre length. The experiment was destructive: Measurements started with long fibres, which were successively cut into shorter lengths.

The LasIRvis fibre was measured at a later point, when the Ocean Optics HR4000 spectrometer had been calibrated for absolute irradiance. For this reason the HR4000 was used to measure edge emission. The rest of the setup remained the same as the Nanoforce fibres. To keep fibre integrity, instead of cutting it down, it was taped over with black tape, as seen in Figure 4.2.

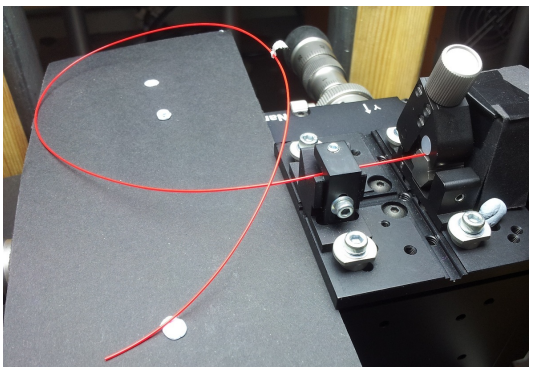

Figure 4.1: Fibre illuminated under a solar simulator. One end is fixed by a fibre launcher and enclosed in a light shield. A silicon solar cell is coupled onto the end using index matching fluid.

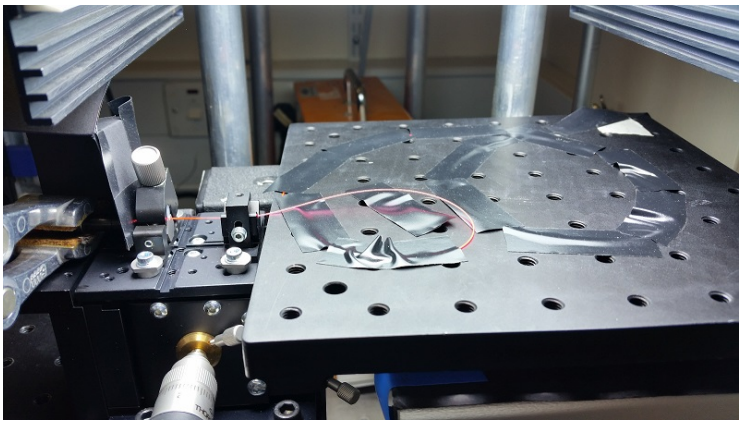

Figure 4.2: The LasIRvis fibre under the solar simulator. Rather than cutting the fibre down, it is taped off in 5cm increments of black tape.

4.1.3 Linear increase in photon concentration as a function of length

As shown by experimental data presented in Figure 4.3, photon concentration is seen to increase linearly as a function of fibre length for up to the manufactured lengths of 2 metres for the Nanoforce-manufactured fibres and up to 80cm for the the commercial fibre. This agrees with the simulation results (shown as the green plot in Figure 4.3) obtained by Edelenbosch *et al.* , whereby photon concentration increases linearly for long distances. [69].

The LasIRvis fibre was in reality 1.5metres long, however there was a double kink almost exactly in the middle of the fibre, which induced a scattering point

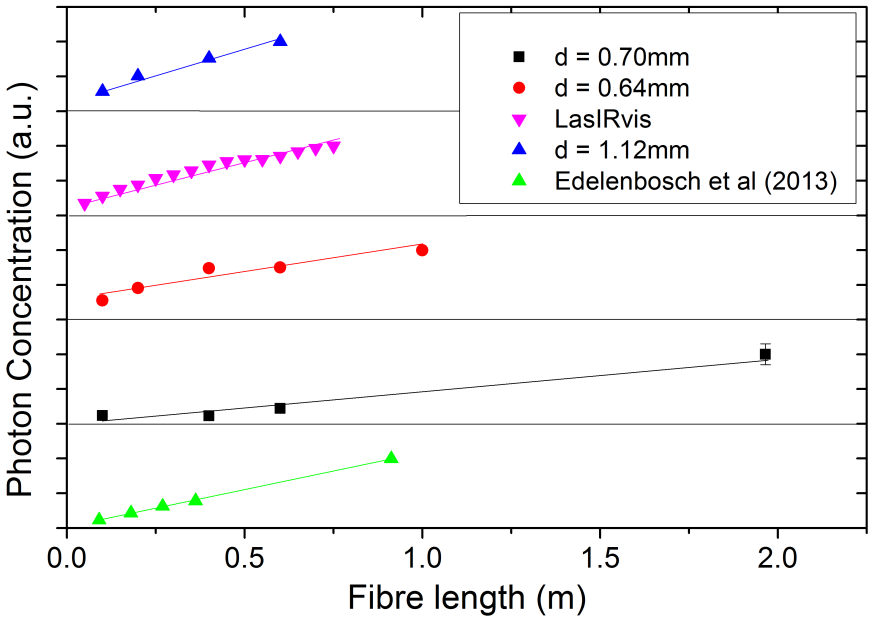

Figure 4.3: Experimental values of photon concentrations of fibres of differing lengths from three sample batches. Nanoforce fibre dye load concentrations are 0.5±0.25wt% with average diameters of 0.64mm, 0.7mm and 1.12mm. The LasIRvis fibre has a diameter of 0.5mm and has a dye load concentration less than that of the Nanoforce manufactured fibres. Photon concentration increases linearly with fibre length up to the 2 metres of manufactured fibre. This agrees with previous raytrace modelling [69]

for luminescence, as shown in Figure 4.4a. For this reason only the first 75cm of the fibre was included in Figure 4.3. Photon concentration for the full length of the fibre is shown in Figure 4.4b. The position of the kink is shown by the dashed line, and a change in the gradient of photon concentration increase is seen just after it. For this reason it can not be determined if this change in gradient is down to normal waveguide losses or reabsorption and reemission losses in the fibre, or down to this scattering point in the kink.

4.1.4 Short-distance redshifting of luminescence

Looking at both Figure 4.3 and Figure 4.4b, the photon concentration trendline does not continue to zero. This would suggest that the increase in photon concentration was larger and plateaued to the gradient observed for large fibre lengths. This could be explained by large initial losses of luminescent light due to multiple

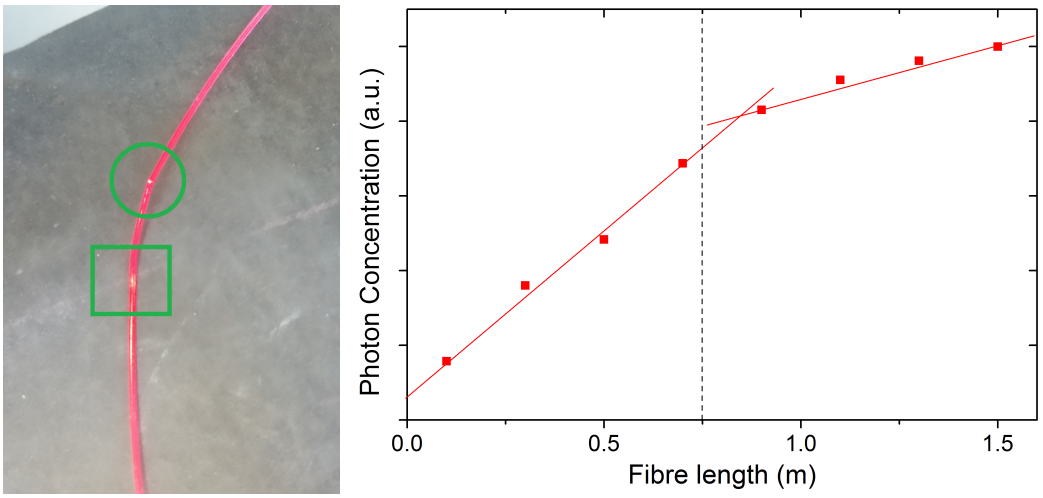

(a) Scattering point in the LasIRvis fibre

(b) Photon concentration of the LasIRvis as a function of the whole length of the 1.5 metre fibre.

Figure 4.4: Halfway down the LasIRvis fibre, there is a double kink shown by the green square and circle in 4.4a. The fibre structure has been compromised, as shown by the luminescence emission coming out of the kink highlighted by the green circle. For this reason the change in gradient of the linear concentration as shown in 4.4b that happens at exactly this point cannot be completely determined to be either by constant waveguide losses or the scattering point.

re-absorption and re-emission events.

The amount of re-absorption and re-emission can be determined by the level of redshifting experienced by luminescent light as it travels down a fibre. In order to determine this, the emission spectrum of a fibre end is measured with the HR4000 spectrometer whilst a 532nm laser excites various points away from the fibre end. As shown in Figure 4.5, when looking at emission spectrum as a function of excitation distance away from the measured fibre end, luminescence redshifting caused by re-absorption and re-emission occurs most significantly in the first centimetre of the fibre. The magnitude of the redshifting drastically decreases within the next couple of centimetres of the fibre. Even for a lower dye concentration such as in the LasIRvis fibre LSC, the same effect holds true, with very small redshifting occurring at longer distances.

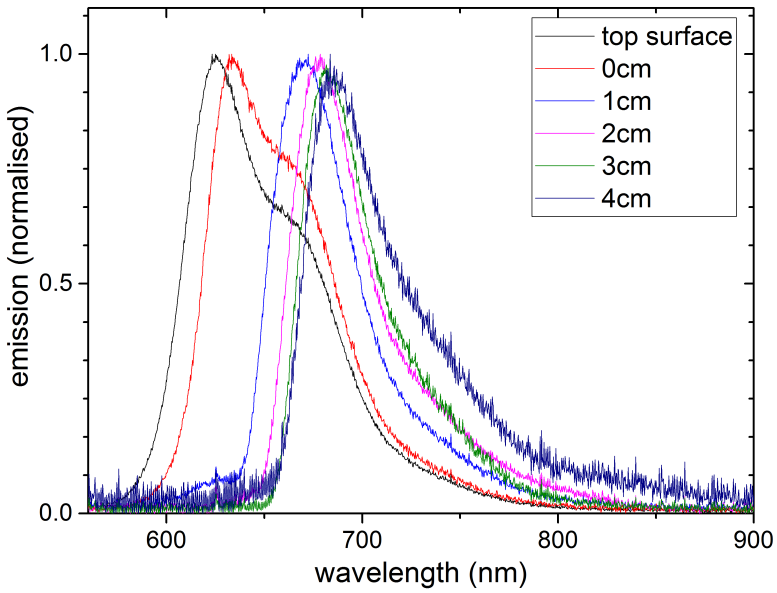

(a) Nanoforce fibre redshifting

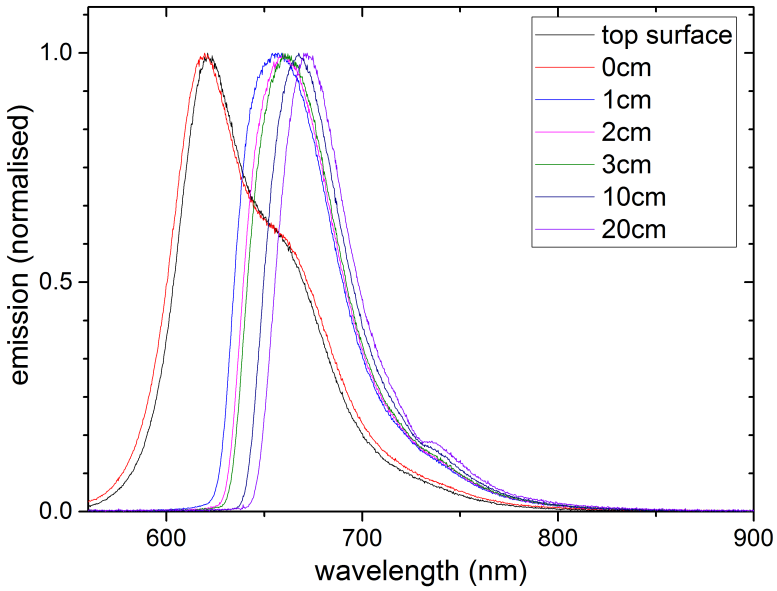

(b) LasIRvis fibre redshifting

Figure 4.5: Demonstrating the short distance effects of luminescence re-absorption and re-emission in fibres doped at high concentration. A spot on a fibre is excited by a 532nm laser. Distances shown are the excitation distance away from the measured end of the fibre. The non-redshifted top surface emission spectrum is shown for reference. The most significant re-absorption and re-emission occurs within the first 1cm of the fibre, as shown by the high redshift for both a Nanoforce-manufactured fibre (a), and a commercially bought Lumogen Red F 305 fibre from LasIRvis Optoelectronic Components Ltd (b).

4.2 Shading between cylinders

The nature of a non-flat surface of a cylinder means that it will be blocking light onto a neighbouring cylinder when the angle of incident is not perfectly normal to the cylinder array. A transparent cylinder, by its curved surface, focusses incident light roughly onto a point. It can be seen in Figure 4.6 that at lower non-zero angles of incidence, a cylinder will focus light away from its neighbour (Figure 4.6b), up until a certain threshold angle where it focuses light back into it Figure 4.6c).

To analyse the shading/focusing effects of cylinders on their neighbours, pvtrace is used to raytrace a cylinder cross-section. In this section it is used as a simple 2D model which is not wavelength specific, with fully transparent cylinders in order to demonstrate pathways of light as a function of angle of incidence. A refractive index of n=1.5 is used within the circles. In reference to the raytrace figures presented, we analyse the shading/focusing effects on the leftmost circle as a function of incident light angle of incidence.

Looking initially at a two cylinder system, a cylinder focuses all light away from its neighbour, meaning it is essentially opaque to its neighbour, at low angles of incidence. The angle threshold at which light starts to be redirected back into the cylinder's neighbour is 60°. As seen in Figure 4.6c, by 61°, the redirection of light is already significant. The rate of increase of redirected light decreases as the angle of incidence increases.

This redirection of light into the array is a form of light trapping. The path length of incident light through the LSC is increased, thereby giving it a greater probability of being absorbed by the luminescent material. Figure 4.7 visually demonstrates this light trapping effect. This is analogous to texturing surfaces in solar cells to increase scattering for greater absorption in the bulk material.

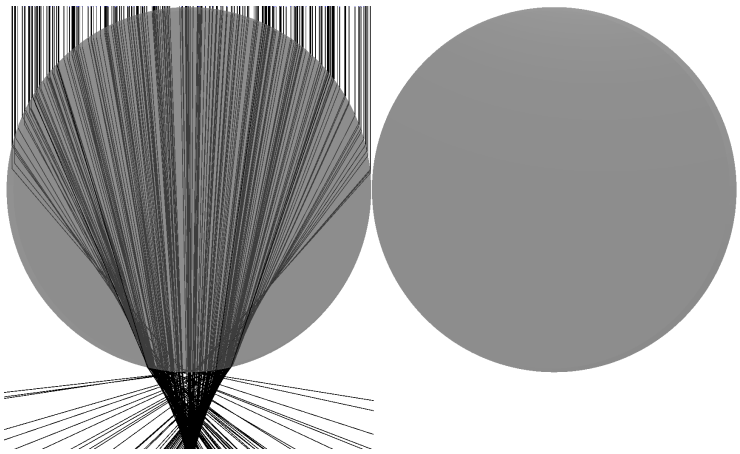

(a) 2 cylinders, 0° angle of incidence

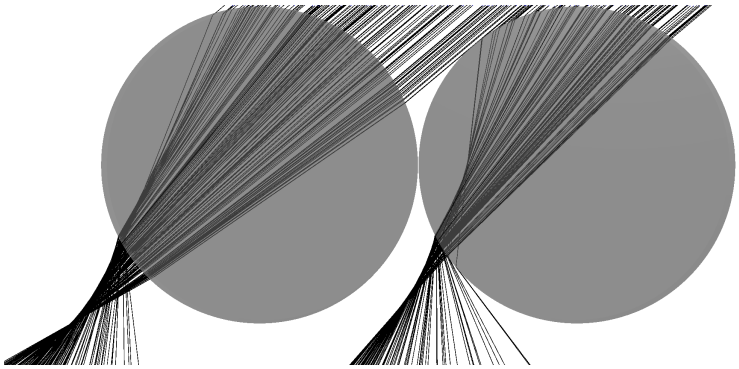

(b) 2 cylinders, 50° angle of incidence

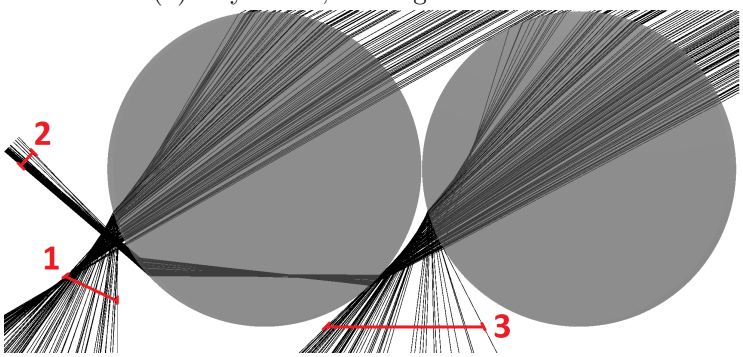

(c) 2 cylinders, 61° angle of incidence

Figure 4.6: Raytracing to determine the shading effects of one cylinder to another. Secondary effect ray traces are removed from figures for clarity. The focussing effect of a circle geometry can be seen, and at a non-zero angle of incidence, a cylinder will focus light away from its neighbour, thereby rendering it essentially opaque (4.6b). The threshold angle at which the shading circle starts to redirect light back into its neighbour is 60°, and at 61° this redirecting is already quite pronounced (4.6c). The three major paths of light through two circles are: 1) light incident on the desired circle passing through, 2) light being directed into the desired circle by its neighbor, and 3) neighbour directing light away from the desired circle.

With two neighbouring cylinders, i.e. a three-cylinder array, having a next nearest neighbour significantly changes the light redirecting behaviour past the 60° angle of incidence threshold. Whilst at angles of incidence of 0-60°, the shading effects are identical, at larger angles there is a two part light direction process. Between angles of incidence of 60-70°, light is redirected to the leftmost cylinder, with peak redirection at 70°. At angles larger than 70° however, the rightmost cylinder diverts incident light that would have been redirected into the leftmost cylinder, away from it. This is shown pictorially as process 5 in Figure 4.8.

Expanding up to a more realistic analysis of a large number of neighbouring cylinders, as shown in Figure 4.9, there is the same positive effect of incident light redirecting into a cylinder's neighbour within the 60-70° angle range, however after this secondary 70° threshold, the amount of light being diverted from the array altogether increases significantly.

The net positive geometrical effect with cylinders, where light is redirected back into the cylinder array by neighbouring cylinders, only occurs in a fine angle range of 60-70°. This geometrical effect should be seen in cylindrical arrays, where its performance should be boosted when the zenithal angle of the Sun on the array is within this 60-70° angle range.

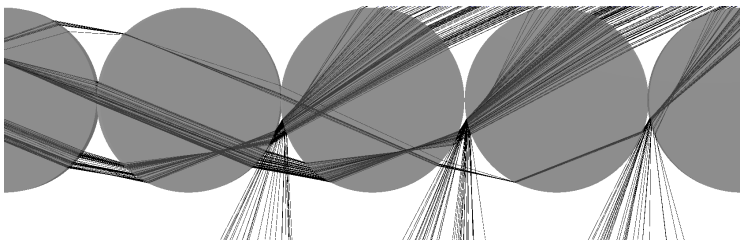

(a) Circular array, 65° angle of incidence

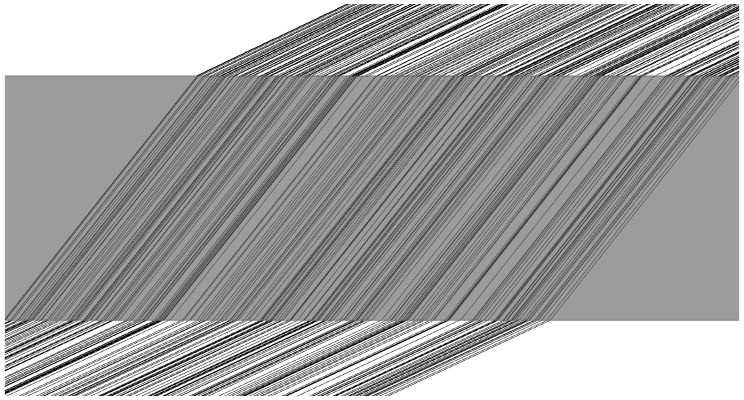

(b) Planar geometry, 65° angle of incidence

Figure 4.7: Demonstrating the light trapping effect of a circular array against planar geometry, with incident light coming in at 65°. The path length of incident light is increased through the LSC, thereby giving it a greater probability of absorption. Secondary effect ray traces are removed from figures for clarity.

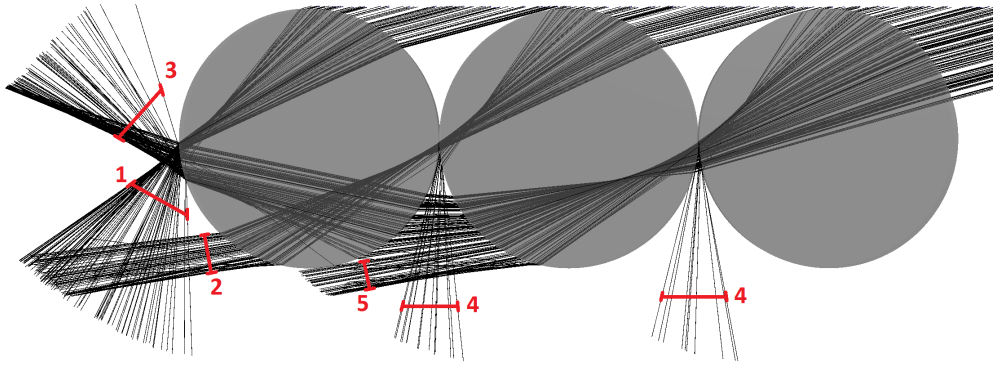

Figure 4.8: Two circles shading the left (desired) circle with incident light at an angle of 75°. Secondary effect ray traces are removed from figures for clarity. The five main paths of light through the system are: 1) incident light passing directly through the desired circle, 2) light redirected into the desired circle by its nearest neighbour, 3) light redirected into the desired circle from its next nearest neighbour, via its nearest neighbour, 4) light diverted away from a circle's neighbour, and 5) light from the next nearest neighbour, being redirected into the nearest neighbour but then missing the desired circle. Light path 5 is responsible for the decrease in number of photons reaching the desired circle at angles of incidence greater than 70°.

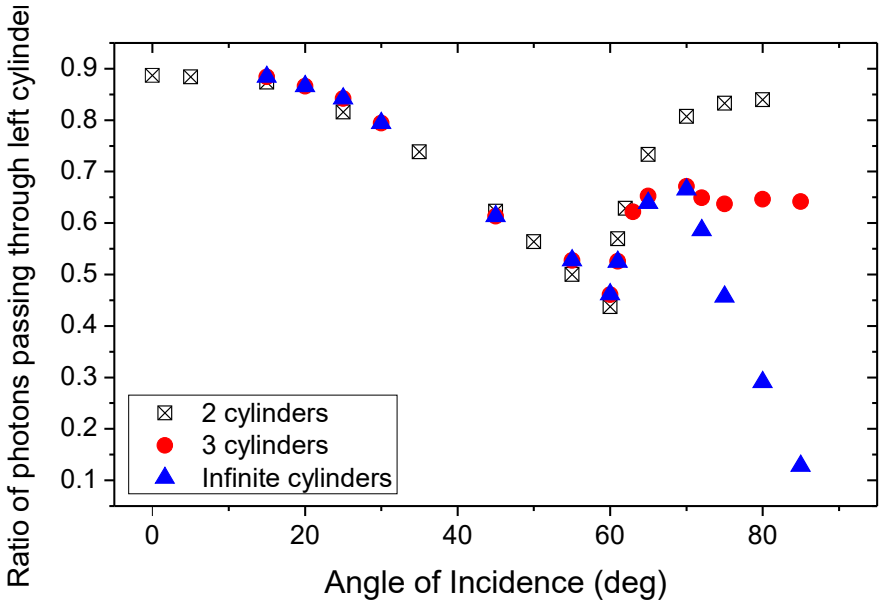

Figure 4.9: Ratio of light entering the left circle to incident light with increasing angles of incidence, with 2 circles, 3 circles and an infinite array of circles, in order to demonstrate shading/light redirection effects. Secondary effect ray traces are removed from figures for clarity. There are two threshold angles, the first being at 60° when light which was initially focused away from the left circle, is then being redirected back into it. The second threshold angle applies to three circles or more, at 70°, when light gets focussed away again from the left circle, which is caused by shading and redirection effects of subsequent circles.

4.3 Analysis of cylinder geometry effects on LSC performance in simulated London clear sky light conditions

A real world light condition model on pvtrace is constructed in order to determine whether this angle-dependent light trapping can cause efficiency boosts in cylindrical LSC arrays. SunPositionSource and HemiSource functions were added into pvtrace for these simulations. Four days in 2014 were chosen to demonstrate this effect: 10th March, 10th April, 10th May and the summer solstice 21st June.

4.3.1 Pvtrace model setup

The model requires data input for the lighting conditions on an LSC fibre area, namely spectral and angular data for both the direct and diffuse spectral component of incident light from a given time, global position and date. The diffuse component is treated as a hemispherical and isotropic light source on the area. For the direct component, the azimuth and zenith angle of incidence is fed in to give a vector property to a planar light source. Version 2.9.5 of the Simple Model of Atmospheric Radiative Transfer of Sunshine (SMARTS) [8], developed by Dr. Christian Gueymard, is used to obtain spectral data. The limiting factor of the software is that spectral data given is on the assumption that it is clear sky weather conditions. The Sun's angle of incidence is symmetric on either side of the Sun's solar peak position, which is around midday for the chosen simulated days. For this reason only morning hours needed to be investigated.

A horizontal ten-cylinder LSC array was aligned North-South so that the hypothesized performance boosts can be shown over the course of a day due to the Sun's path across the sky. Each cylinder had a diameter of 1cm and a length of 40cm. Perfect specular mirrors were added to the long sides of the array. The cylinders themselves were modelled as a PMMA host matrix, of refractive index n=1.46, homogeneously doped with BASF's Lumogen F Red 305 luminescent material. The whole cylinder's absorption coefficient is set to $9000m^{-1}$ at its absorption peak wavelength of 576nm. This corresponds to a dye load concentration of around 1.6%. The cylinder surfaces are modelled as being perfectly smooth. Square rod LSCs were simulated in tandem as a reference to the performance of planar geometries.

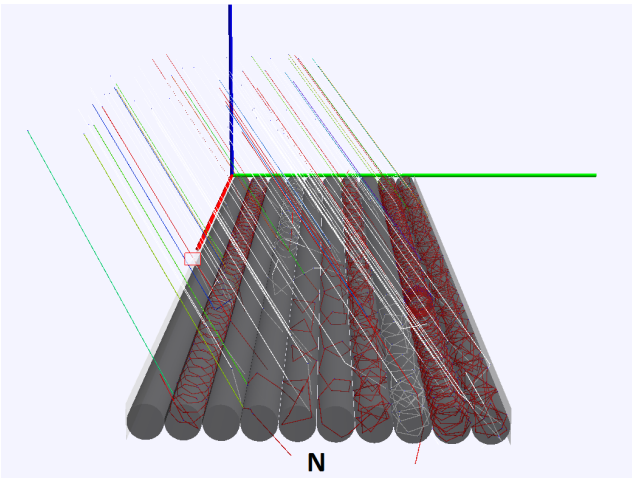

(a) Direct component simulation. North direction shown

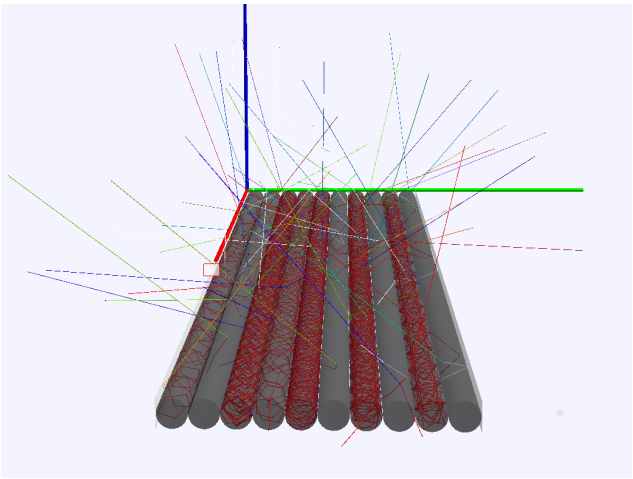

(b) Diffuse component simulation

Figure 4.10: A mid-simulation snapshot of (a) the direct and (b) the diffuse component of light illuminating a cylindrical LSC array. North is [1,0,0], and is shown in (a). The direct light vector is determined by the position of the Sun. The diffuse component is modelled as a hemispherical light source. The spectra for both components of light is obtained from the SMARTS software [8].

Simulations for the direct and diffuse light components were done independently for each given time interval of the day. Each simulation modelled an illumination of 100,000 photons onto the array. The optical efficiency μ_{opt} of the array is obtained for both direct and diffuse components. These values are weighted by their respective photon flux ratios at that specific time. For example on 10th May 2014, the components of direct and diffuse light contributed 0.85 and 0.15 at 0700h, and

0.91 and 0.09 at solar noon respectively.

The location under investigation was London, UK (Lat: 51.5°, Long: -0.13°). Suitable days are needed to demonstrate this light trapping effect, with the criteria being that the Sun's zenithal angle is within the light trapping range for a significant amount of the sunrise-noon period. Furthermore, the peak light trapping time should be where the effect would be most visible with an efficiency peak that would stick out in comparison to the planar efficiency profile during the morning. The four aforementioned days were chosen to show light trapping at the beginning and also in the middle of the sunrise-noon period. The peak light trapping angle is halfway through the morning for both 10 March and 10 April, with the Sun's zenithal angle to be within the light trapping region between 0830h - 1000h. For 10 May, the light trapping angle range is between the earlier times of 0730 - 0900h, and for the Summer solstice (21st June), the light trapping angle is between 0700h - 0900h.

4.3.2 Results

Simulations on these four days demonstrate the advantage of having a cylindrical LSC array compared to an planar geometry LSC. Efficiencies as a function of time of day are shown for cylindrical arrays on the right, and planar arrays on the left, in Fig. 4.11. There is a visible boost in LSC efficiencies for cylindrical arrays in comparison with planar arrays in the time periods when the angle of incidence of sunlight is within the light redirection range (see Figure 4.12). At 70°, where the redirection effect is at its strongest, cylindrical geometry efficiencies are 5% - 10.7% relatively higher than that of planar geometries. Due to lower surface Fresnel reflection losses, diffuse light is more impactful in the cylindrical array than in the planar array.

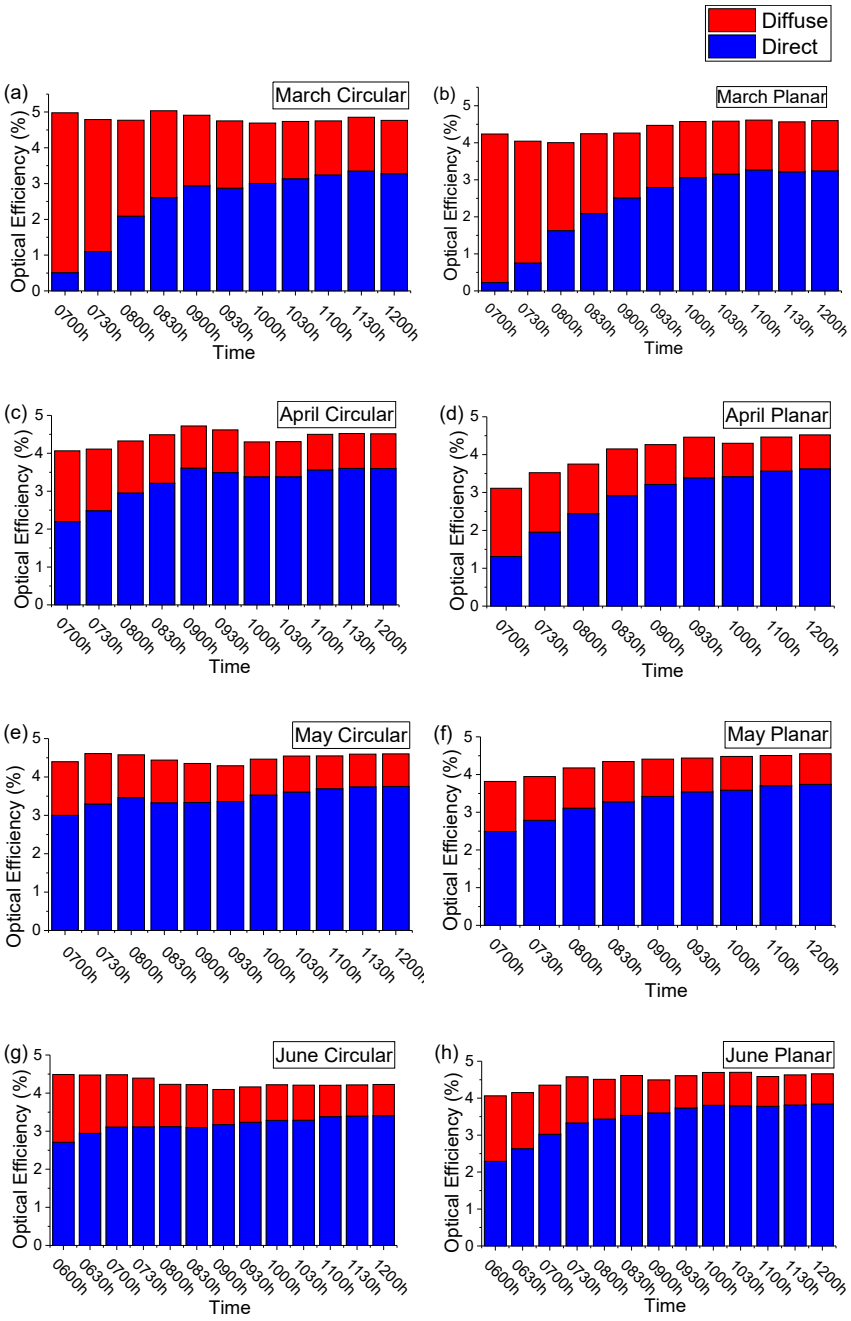

Figure 4.11: Comparing the efficiencies of circular (left) and planar (right) rod LSC arrays, for the 10th March, 10th April, 10th May between 0700h - 1200h and 21st June 2014 between 0600h - 1200h. For each time segment, the red top sections show the contribution of the diffuse component of the incident light, and the blue bottom sections show the contribution of the direct component of the incident light. Circular geometries outperform square geometries up until 1000h for 10th March, 1000h for 10th April, 0830h for10th May and 0800h for 21st June 2014. This is due to increased efficiency values for the direct component of incident light, which can be attributed to its angle of incidence being within the "light redirection" range as explained in section 4.2.

4.3.3 10th March 2014

Efficiencies are shown for the cylindrical rod array in Figure 4.11(a) and the planar array in Figure 4.11(b). The cylindrical array has a higher total efficiency than the planar array for the whole day, however the efficiency difference between the two geometries is highest in the morning before 0930h. The planar array increases in efficiency, with a plateauing of this increase, from sunrise until noon. When the time of day is linked to the zenithal angle of the Sun, as done so in Figure 4.12(a), it can be seen that this peak is due to the light redirection effect of cylindrical geometries, where the profile of the array's efficiencies matches that of the ratio of incident photons coming into a left hand cylinder as described in section 4.2 when overlaying the time of day with its respective solar zenithal angle. Peak redirection in the cylindrical array is at 0900h, which can be seen by an efficiency peak of the direct light component both in Figure 4.11(a) and in Figure 4.12(a). The cylindrical array's efficiency is relatively 7% higher than that of the planar array at that time.

4.3.4 10th April 2014

Efficiencies are shown for the cylindrical rod array in Figure 4.11(c) and for the planar rod array in Figure 4.11(d). Overall the cylindrical array outperforms the square array closer to sunrise, but the efficiencies of both are similar closer to noon. The planar array increases in efficiency, with a plateauing of this increase, from sunrise until noon. The efficiency of the cylindrical array however experiences a peak at 0900h, whereby its efficiency is greater even compared to noon. The array's peak performance is at the maximum redirection angle, beating its performance at noon, which is the peak performance time for planar geometries. At peak redirection time, 0900h, the cylindrical array's efficiency is relatively 10.7% higher than that of the planar array.

4.3.5 10th May 2014

Efficiencies are shown for the cylindrical rod array in Figure 4.11(e) and for the planar rod array in Figure 4.11(f). Much like the other investigated days, the cylindrical array outperforms the square array closer to sunrise, but the efficiencies of both are similar closer to noon. An efficiency peak is seen at the peak redirection angle at 0800h. By overlaying the solar zenithal angle with the shading/redirection profile and the efficiency profile as a function of time of day, it is seen that the redirection effect angle range matches the efficiency boost at the start of the day. At peak redirection time, 0800h, the cylindrical array's efficiency is relatively 9.7% higher than that of the planar array.

4.3.6 21st June 2014

Efficiencies are shown for the cylindrical rod array in Figure 4.11(g) and for the planar rod array in Figure 4.11(h). For the Summer solstice, peak redirection happens at 0700h. Whilst the efficiency peak due to the direct component is easily seen in Figure 4.12(d), it is more hidden when taking into account the weighting ratio between the direct and diffuse component at that time, as seen in Figure 4.11(g). The redirection effect is still seen when compared to efficiencies for the planar array, with a relatively flat efficiency profile throughout the day. Whilst the cylindrical array has higher efficiencies within the redirection angle range, once the Sun is out of this angle range after 0700h, the planar geometry has higher efficiency values. The cylindrical array's efficiency is relatively 5% higher than the planar array at 0600h. The planar array's efficiency at 1030h however is relatively 5.5% higher than that of the cylindrical array. This is due to the sun being at its highest point of the year, almost at normal incidence to the LSC. Fresnel reflections are at a minimum, which allow to demonstrate the planar geometry's superior waveguiding of luminescent light.

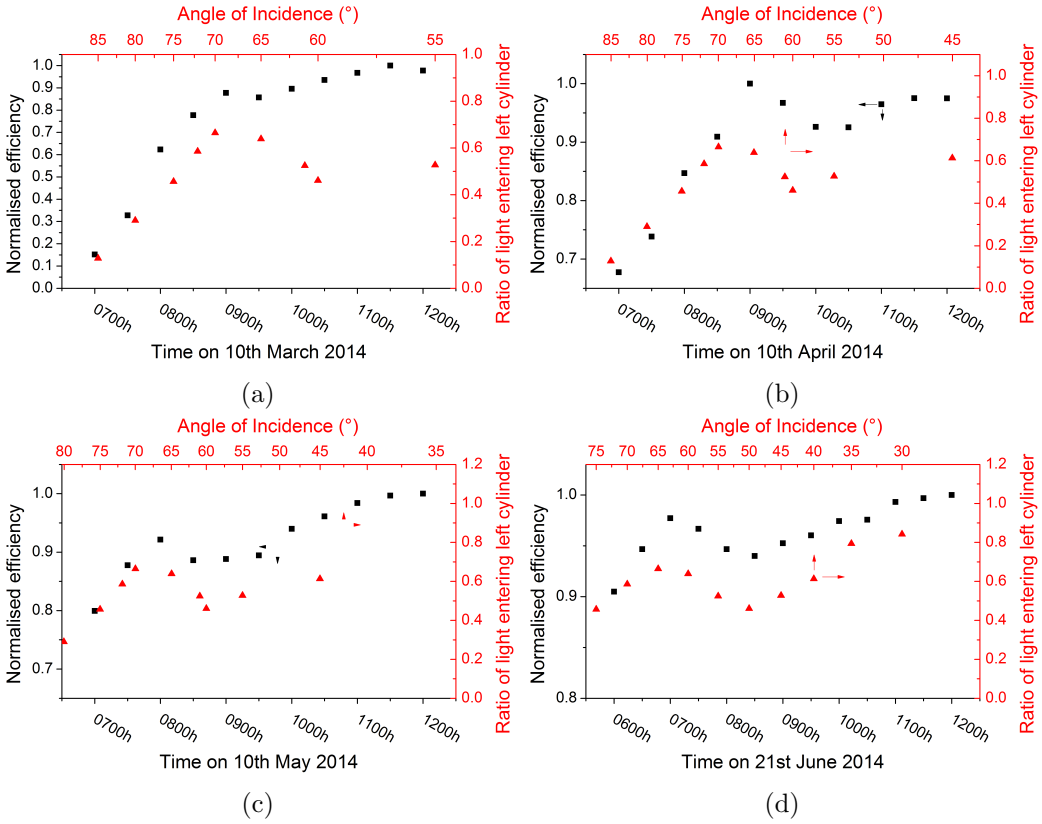

Figure 4.12: Normalised efficiency values for the circular array at different times of the day vs the ratio of incident photons directed into a cylinder from the Sun and the cylinder's neighbours (triangle). Graphs for (a) 10th March, (b) 10th April, (c) 10th May and (d) 21st June 2014. The angle of incidence is matched to the time of day. The efficiency increase/decrease behaviour matches that of the ratio of photons entering a given cylinder relative to the light's angle of incidence, confirming the impact geometric effects have on a cylindrical array.

4.3.7 Discussion on angle-dependent light trapping

The redirection angle range shifts in timing and duration over the course of the year. For London, the four days mentioned were investigated in the knowledge that for a quarter to a third of the day, the Sun's incident angle on the array would be in this range of interest, in order to more effectively demonstrate the geometrical effect. For the Winter solstice, the Sun is so low in the sky that its zenithal angle never enters the redirection range. This relationship between time of year and Sun's angle of incidence being within the redirection range is also dependent on the global latitude of the LSC's location. This efficiency boost by light trapping is yet to be

confirmed experimentally.

This efficiency boosting geometric effect of cylinders in an array could be used to optimise LSC arrays in the field, by way of manipulating its orientation and cardinal alignment. This process would be analogous to that of finding the optimal angle for a photovoltaic module given its location and desired maximum performance time/season envelope. This effect introduces an extra consideration when embodying cylindrical LSCs (CLSCs) into a building façade. Light trapping in vertically aligned CLSCs would be sensitive to the azimuthal direction in which the building façade is facing, and the azimuth of incident sunlight. Horizontally aligned CLSCs would be sensitive to the zenithal component of incident sunlight.

As was shown for LSC performance on 10th April 2014, correct cardinal alignment and tilt could give an array two maximum performance points during the day, which is a characteristic not seen in planar geometry LSCs.

In addition to this geometric effect, the geometric concentration of a cylindrical fibre array is greater than to a planar array that covers the same module area by a ratio of $\pi/4$, due to the differences in fibre end areas.

The investigation performed here was on a single layer of thick cylindrical and square fibres of 1cm. It is unknown whether the geometrical boosts seen here would carry on for subsequent layers of cylinders in a multi-layered LSC array.

4.4 Conclusion

Homogeneously doped cylindrical fibre LSCs were manufactured. Measurements show a linear increase in photon concentration as a function of fibre length for fibres in the length range of 0.1m - 2m. Re-absorption and re-emission of luminescent light occurs most significantly in the initial few centimetres of a fibre, which means for the

majority of the length of a fibre LSC, the major loss mechanisms are waveguide surface imperfections and host material non radiative absorption. This short distance re-absorption and re-emission effect was demonstrated by measuring the redshift of luminescence across the fibre, with the largest redshifting occurring within the first 2 centimetres of a highly doped luminescent fibre.

2D raytracing of the shading effects of circles onto their neighbours showed that a circle deviates all incident light away from its neighbour when the angle of incidence is in the angle range of 0° - 60°. After this threshold angle, the circle starts to redirect incident light into its neighbour up until a second threshold angle of 70°, when light starts to once again get deviated away from the circle's neighbour. This can be seen as a form of incident light trapping within an LSC. A hypothesis was put forward that this geometric effect can be used to boost the performance of a cylindrical LSC array when the angle of incidence of the sun on such an array was within this redirection range.

Using SMARTS software for spectral and sun position data, pvtrace was used to calculate the optical efficiencies of a horizontally placed, North-South aligned cylindrical LSC array in simulated clear sky light conditions for 10th March, 10th April, 10th May and 21st June 2014 in London, UK. Overall the cylindrical array outperforms the planar array, but efficiencies for both geometries become more equal closer to solar noon, where the incident light angle of incidence is closer to normal. More importantly, the cylindrical LSC array experiences an efficiency boost for the times of the day where the sun's incident zenithal angle is within the redirection range of 60° - 70°, an effect not seen in planar geometry LSCs with identical simulation conditions. At 70°, where the redirection effect is at its peak, this efficiency boost means that cylindrical rod efficiencies reach a value 5%-10.7% higher than that of planar rods. On 10th April 2014, the cylindrical array experiences two performance peaks, one of them being due to light redirection.

This efficiency boost could be seen as a practical way to improve a cylindrical LSC array's performance in the field, aligning both its tilt and cardinal direction to give it an efficiency boost in desired time or seasonal periods. Whilst this efficiency boost is relatively small in absolute numbers for isotropically emitting luminescent layers, it will be significant once there are highly anisotropically emitting luminescent layers.

If a new buildling has a cylindrical LSC façade, calculations can be made to determine its orientation in order to provide efficiency boosts during times when maximising solar generation is needed most.

Chapter 5

A water splitting reactor with novel optics

This chapter investigates the optical system to illuminate the double-illuminated photoelectrochemical (PEC) reactor. The first optical system in the discussion is using a reflective cone embedded inside of a waveguide. The reflective cone receives concentrated light by way of a Fresnel lens. An investigation is performed on quantum well solar cells and whether the photoluminescence intensity emitted by one is sufficient to power one of the photo-electrodes. The reflective cone / Fresnel optics is tested outdoors on a fully functioning PEC reactor.

5.1 Direct concentration using a Fresnel lens and a reflective cone

A triple junction photo-cathode is used in the double-illuminated PEC reactor and so require full spectrum illumination. Direct light waveguiding is therefore necessary. The optical system proposed, shown pictorially in Figure 5.1, is comprised of a reflective cone embedded within a waveguide which is coupled to the PEC reactor. Incident direct light is concentrated by a Fresnel lens onto the reflective cone, which then reflects it into the waveguide, which in turns keeps light trapped

by total internal reflection (TIR).

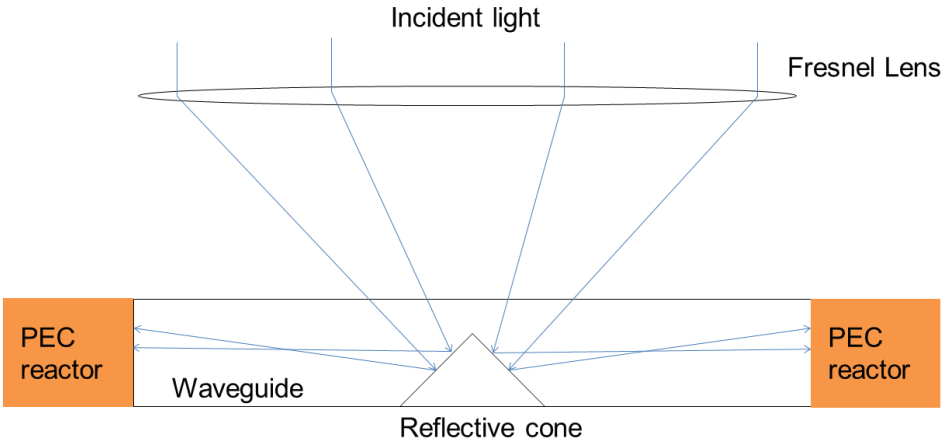

Figure 5.1: A Fresnel lens concentrates direct light onto a reflective cone which is embedded within the waveguide. The cone reflects this light into the waveguide, which is then transported into the PEC reactor.

5.1.1 Optical model of a cone in waveguide

An ideal optical setup would involve a cone with a reflectivity of 1, with all light reflected off the cone being totally internally trapped within the waveguide. This is depicted in Figure 5.1. An imperfect cone would have a reflectivity of less than 1, but also have a non-perfect surface, causing scattering that would mean light is reflected isotropically. A surface that reflects light isotropically is called a Lambertian surface. The two limits for cone reflection would be fully specular to fully Lambertian. This is demonstrated in Figure 5.2.

Assuming normal incident light and a cone with a slope of $\pi/4$, light trapping within the waveguide for a full specular, perfectly reflected cone would be 100%. Measuring light trapping for a Lambertian cone in a waveguide involves calculating isotropic light trapping using boundary angle conditions of the cone. The trapping solid angle of the cone would be from the critical angle of the top surface of the waveguide, to the solid angle of the cone with respect to the top surface:

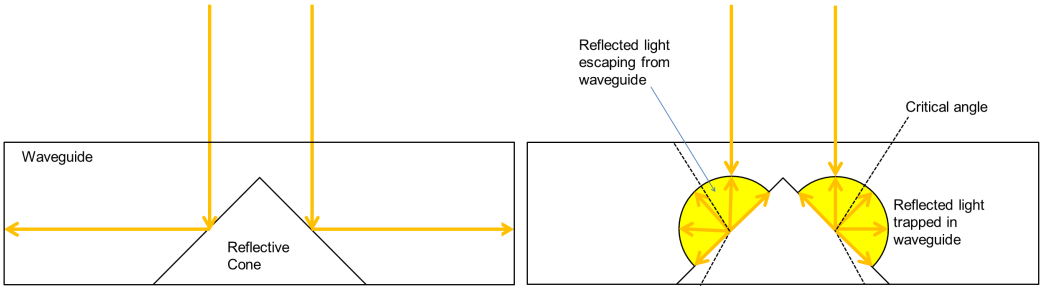

(a) (b)

Figure 5.2: A reflective cone of slope $\pi/4$ with the two limits of reflection time: fully specular (a) and fully Lambertian (b). The schematics are looking at the x-z plane of the waveguide. With light at normal incidence, a fully specular cone traps all light within the waveguide. The trapping solid angle of the cone, which is demonstrated in (b) as the filled in parts of the emission profile, would be from the critical angle of the top surface to the angle of the cone, which in this case is $3\pi/4$. This gives a trapping efficiency of 72.6%

$$\Omega_{trap} = \int_0^{2\pi} d\phi \int_{\theta_c}^{3\pi/4} sin\theta d\theta = 9.126 \tag{5.1}$$

The trapping efficiency is the trapping solid angle divided by the total solid angle 4π:

$$\mu_{trap} = \frac{\Omega_{trap}}{4\pi} = 0.726 \tag{5.2}$$

Aside from the trapping efficiency of the cone, other loss mechanisms exist in the cone-waveguide setup: Fresnel reflection losses on the top surface and within the waveguide for trapped light escaping the edges, and parasitic absorption loss in the waveguide. The cone also acts as a scattering centre for trapped light.

A pvtrace model was set up with a waveguide of dimensions 0.2 x 0.2 x 0.005 m. The waveguide is made of PMMA, which has a refractive index of $n = 1.49$ and an absorption coefficient of $\alpha = 0.3m^{-1}$. Incident light was normal to the waveguide and only illuminated the area of the reflective cone, which is in the middle of the waveguide. Each run used 100,000 incident photons and all four edges being considered for emission capture. The reflective cones in this simulation have unity

reflectivity. Table 5.1 shows the figures for edge emission and photons lost due to parasitic absorption with in the waveguide.

	Fully Specular	Fully Lambertian
Edge photons	89.4%	52.7%
Edge photons on each edge	22.4%	13.1%
Photons parasitically lost	6.4%	16.6%

Table 5.1: Pvtrace simulation of a reflective cone inside a waveguide of dimensions 0.2 x 0.2 x 0.005 m. All four edges are considered for emission capture.

	Fully Specular	Fully Lambertian
Edge photons	49.6%	25.0%
Photons parasitically lost	40.2%	31.5%
Improvement to single edge emission	121%	54%

Table 5.2: Pvtrace simulation of a reflective cone inside a waveguide of dimensions 0.2 x 0.2 x 0.005 m. Three edges are covered in reflective material, and only one edge is considered for emission capture.

In reality, a standalone PEC with a waveguide will have reflectors on the three sides not in contact with any device. The same simulation was made with three specular reflectors of reflectivity $r = 0.95$, imitating commercially available high quality reflective material. Results are shown in Table 5.1. Significantly more photons are parasitically lost, mainly due to the increase in the pathlength of trapped light within the waveguide. The amount of photons exiting the edge in use doubles for the fully specular cone, and increases by 90% for the fully Lambertian cone.

The emission profile across the length of the edge was determined by placing logging segments across it. The emission profiles for the waveguide with and without attached reflectors is shown in Figure 5.3. The specular cone provided a more homogeneous emission profile, following a $\sqrt{cos(\theta)}$ behaviour, compared to the Lambertian cone which has an emission profile that follows a $cos(\theta)$ behaviour. Adding reflectors to three of the waveguide sides homogenises the emission profile of the Lambertian cone. The emission profile no longer becomes a simple cosine

behaviour. Matlab's curve fitting function was used to obtain an emission profile. The fitting functions and parameters are shown in Appendix A for both the specular and Lambertian reflecting cone. These functions are shown as the green lines in Figure 5.3b.

These simulations involved unity reflectivity of the cones. In reality it will be less than unity. Initial experiments on this optical design involved a roughly drilled hollow cone. A perfectly smooth hollow cone would have still caused 100% waveguide trapping due to total internal reflection, but the roughness will have a) induced loss of reflectivity due to transmission and b) caused the cone to behave more like a Lambertian reflective cone.

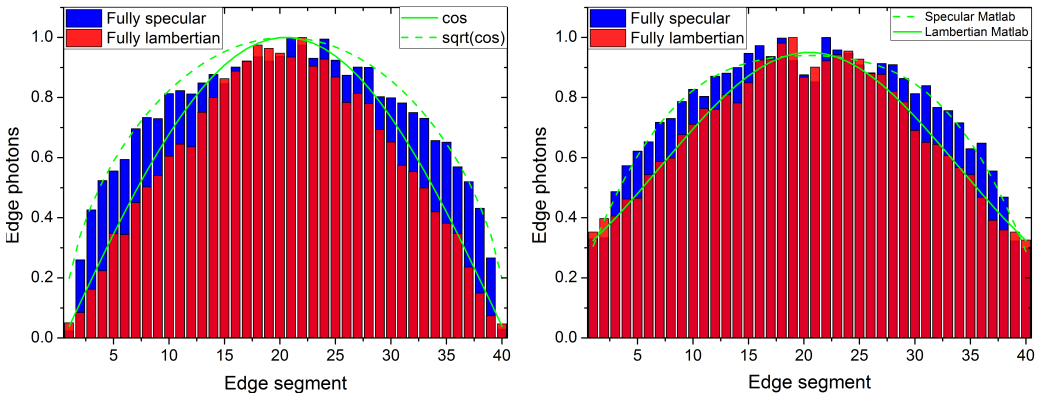

(a) Without reflectors (b) With reflectors

Figure 5.3: Emission profile of the edge of the waveguide (a) without reflectors and (b) with reflectors of reflectivity $r = 0.95$ on the three unused edges.

5.1.2 Experimental high concentration illumination on a cone in a waveguide

A 20cm x 20cm x 0.5cm Clarex UV Transmission PMMA plate was purchased from Weatherall UK Ltd [205]. It has a refractive index of $n = 1.49$ and a stated transmission of 90%. A cone of slope angle 45° and diameter of 3mm was drilled into the middle of the plate by the Solid State Physics technicians. It was left hollow

and without any reflective material coupled onto it. The cone was left unpolished as it was deemed too difficult to do so, and so there were fine, visible striations on the cone due to the drill bit. This means that the cone is not a perfectly specular reflector. The setup described in section 3.5 is used to measured edge intensities at high concentration illumination. The reflective material used on the waveguide edge is aluminium sheets with an adhesive side.

Light coming out of the waveguide edge was measured with and without reflectors on three of the waveguide edges. As shown in Figure 5.4, there is greater irradiance when reflectors are placed on the waveguide edge. Integrating the spectrum with respect to wavelength gives intensity values of Wm^{-2}, which are shown in Table 5.3.

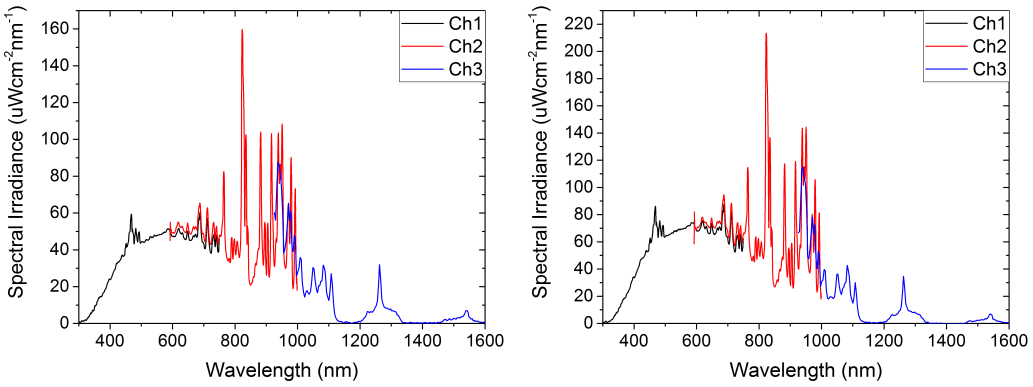

(a) Bare waveguide (b) Waveguide with reflectors on three edges

Figure 5.4: Spectral irradiance of a reflective cone in a waveguide for at position P5, with incident illumination of 1741 Suns.

One would expect the intensity increase in edge emission to be the same for each incident intensity, seeing as the waveguide setup does not change. This is not the case, with an intensity increase between the two wavguides being in the range of 32.6% - 90.8%. Whilst spectrometer detector saturation could explain the higher intensity values having less of a performance increase, the spectrometer was never in its saturation region. A major factor in this could be scattering from the

measurement room. It was a large room built for characterising commercial PV modules. Whilst every wall surface is coloured black, there was still a lot of equipment, including the scaffolding holding this experimental setup, which can scatter incident light. Different distances from the flash lamp would cause a difference in the scattering profile of the setup surroundings, and therefore the amount of stray light entering the spectrometer.

Incident Suns	Without reflectors (Wm^{-2})	With reflectors (Wm^{-2})	Intensity Increase
1741	154.8	205.2	32.6%
907	116.1	162.6	40.8%
298	47.7	91.0	90.8%
118	23.6	40.3	70.7%
20	4.0	6.7	66.3%

Table 5.3: Edge intensity for a cone in a waveguide, without and with reflectors on three of the waveguide edges. Improvement by using reflectors is given on the right hand column.

The spectrometer fibre was not moved from its central position. This means that the emission profile across the edge is not known. Simulation results in subsection 5.1.1 show that the emission profile across the waveguide edge can change depending on whether the cone reflects in a specular or Lambertian manner, as well as whether the waveguide edges are bare or are coupled to reflectors. Both specular and Lambertian emission profile assumptions will be used to integrate the measured illumination value across the waveguide edge to determine the discrepancy between the experimental and simulated values ratios of light in vs light out.

Incident Suns	Specular		Lambertian	
	Bare (%)	Reflector (%)	Bare (%)	Reflector (%)
1741	0.96	1.27	0.80	1.15
907	1.38	1.92	1.15	1.74
298	1.73	3.29	1.44	2.97
118	2.16	3.69	1.81	3.33
20	2.16	3.61	1.80	3.26

Table 5.4: The optical efficiency (Watts out vs Watts in) for the cone in a waveguide.

The optical efficiency (Watts out vs Watts in) for all scenarios is low, being an order of magnitude worse than simulated values. The efficiency ranges for from 0.96% - 2.16% for a specular cone and 0.8% - 1.81% for a Lambertian cone in a bare waveguide. These efficiencies are greater when the waveguide edges are covered in reflectors, with the range rising to 1.27% - 3.69% for a specular cone and 1.15% - 3.33% for a Lambertian cone. All results are presented in Table 5.4. Significant amount of incident light could have been lost by scattering down through the cone and out of the back of the waveguide. This could have been solved by adding reflective material to the inside of the cone.

The improvement to single edge optical efficiency by adding edge reflectors is shown in Table 5.5. Simulation results show that for a cone of specular reflection behaviour, adding reflectors to the waveguide edges improves edge optical efficiency by 121%, and for a cone of Lambertian behaviour, this improvement is by 54%. Experimental results demonstrate improvements of optical efficiency by 24.4% - 47.5% assuming specular cone reflection, or 30.1% - 51.4% assuming Lambertian cone reflection.

Regardless of reflection assumption on the manufactured cone, the experimental improvement to waveguide efficiency by adding reflectors is less than the simulated improvement for a Lambertian cone. Imperfect coupling of the reflectors to the waveguide edge, as well as a reflectivity lower than the simulated value of $r = 0.95$ could have affected this improvement. Further improvement to the experimental technique would be to measure the edge emission across various points on the waveguide guide to establish an emission profile and verify agreement with the simulated emission profile.

As mentioned above, the cone was drilled into the waveguide, and had a non-uniform surface caused by drilling striations. This coupled with edge emission

improvement values closer to the simulated Lambertian cone values point towards it being more Lambertian. A next step is to manufacture a more perfect cone, and to line it with reflective material.

Incident Suns	Improvement to edge emission (%)	
	Specular	Lambertian
1741	24.4	30.1
907	28.5	33.8
298	47.5	51.4
118	41.3	45.7
20	40.2	44.7

Table 5.5: Comparing the improvement to edge emission when adding edge reflectors. Simulated improvements to edge emission is 121% for a fully specular cone, and 54% for a fully Lambertian cone. The improvements shown suggest the cone is mostly reflecting incident light in a Lambertian manner.

5.1.3 Outdoor measurements on a fully functioning PEC reactor with the cone in a waveguide concentrating optics

The work in this subsection is part of the total work on the PEC reactor performance that was presented by Dr. Anna Hankin at the SolarFuels16 conference in Berlin, Germany.

The PEC reactor with a hematite photo-anode and triple-junction InGaP/GaAs /Ge photo-cathode was placed on a trolley mount. Coupled into the two reactor windows was a 15cm x 15cm x 0.4cm waveguide with cones drilled into the centre. The cones, which were drilled in by the technicians in the Chemical Engineering department, had much finer striations. Each cone had incident light concentrated on it by a Fresnel lens. The lenses were purchased from Edmund Optics, and had an active concentrating area of diameter 6 inches. Each waveguide had white Polytetrafluoroethylene (PTFE) reflectors, with a reflectivity of $r = 0.7$, on the three edges not coupled into the reactor. The mount could be tilted so that the setup could be aligned with the sun. The setup is shown in Figure 5.5.

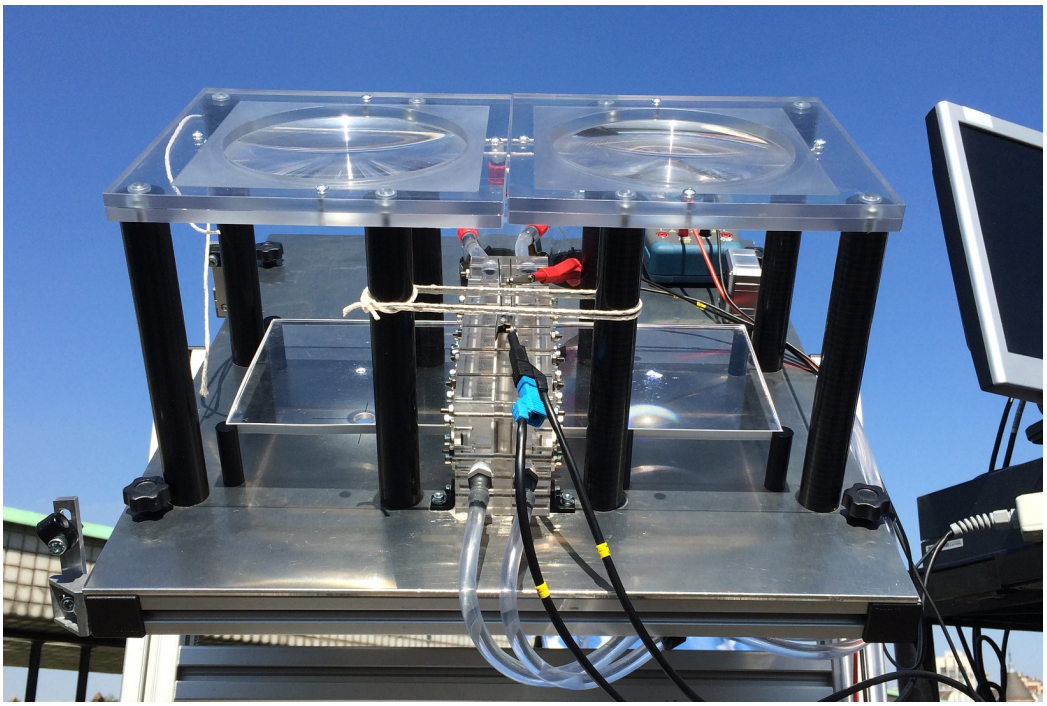

Figure 5.5: A fully functioning PEC reactor with Fresnel lens/cone concentrating optics on the Level 8 balcony of Blackett Laboratory. The setup was orientated towards the sun. There was a slight misalignment with the right hand Fresnel lens and cone, which is causing a significant amount of light to be transmitted through the waveguide. The crocodile clip wires measure the photocurrent through the reactor. Electrolyte is pumped through the reactor to extract and collect hydrogen and oxygen.

The PEC reactor was run during the summer of 2016 on days with clear sky weather conditions. The calibrated Ocean Optics HR4000 fibre spectrometer, with a cosine corrector, was used to measure incident sunlight to determine the power density of incident light. It was also used to measure the power density of light coming out of the waveguide edge. The emission profile of the waveguide edge is shown in Figure 5.6 on four separate occasions during the measurement days: three with edge reflectors, and one without. Because the mount was stationary, the emission profile across the waveguide was continually changing due to the movement of the sun causing a gradual misalignment with the optics. This is manifested in Figure 5.6 as a slight curve skew to one side.

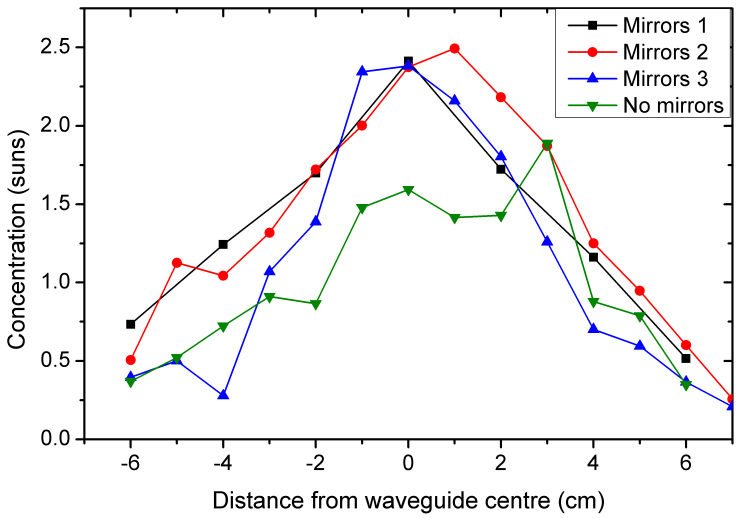

Figure 5.6: The power density of light across the edge of a waveguide with an embedded reflective cone, with and without edge mirrors. The profile is more similar to that of a waveguide with a lambertian reflective cone (Figure 5.3). The increase in power density is around 50% when adding reflectors around the waveguide, also in agreement with pvtrace modelling (Table 5.2).

The concentration of incident light at the middle of the waveguide edge is around 1.5x with a bare waveguide, and around 2.5x concentration when the edges of the waveguide had reflectors. It was shown in Table 5.2 that the increase in edge emission by adding reflectors would be 121% with a specular cone and 54% with a Lambertian cone. Furthermore, comparing the profile shape of Figure 5.3 with that of the simulated profiles in Figure 5.3, the experimental profile shape is most similar to that of a Lambertian reflecting cone. Thus, this confirms that the striation imperfections on the drilled cone would lead it to behave more Lambertian than specular.

The geometric concentration ratio of the optics is the active concentrating area of the Fresnel lenses over the waveguide edge area. With a lens diameter of 15.24cm, this makes the geometric concentration ratio of $C_G = 20.3$. The best efficiencies for this optical system are 49.6% and 25% for a specular and Lambertian reflective cone respectively, making the best possible photon concentration of $C_\gamma = 10.1$ and $C_\gamma = 5.1$ respectively.

Considering the reflective cone has been determined to be Lambertian in nature and was measured to have a concentration of $C_\gamma = 2.5$, it means the setup can be improved by a factor of 4. This would be done by using more perfect reflective material around the waveguide edge, and by using a perfectly smooth specular reflective cone.

The profile of light across the waveguide edge would ideally be uniform. This cannot happen with optics that revolve around having a reflective cone. The next iteration of the optics would facilitate having a uniform illumination profile across the photo-electrodes by using a linear Fresnel lens concentrating light onto a reflective wedge in a waveguide. This is shown diagrammatically in Figure 5.7. Coincidentally it would also be easier to cut and polish this straight surface, enabling a faster trajectory towards the theoretical maximum optical efficiency.

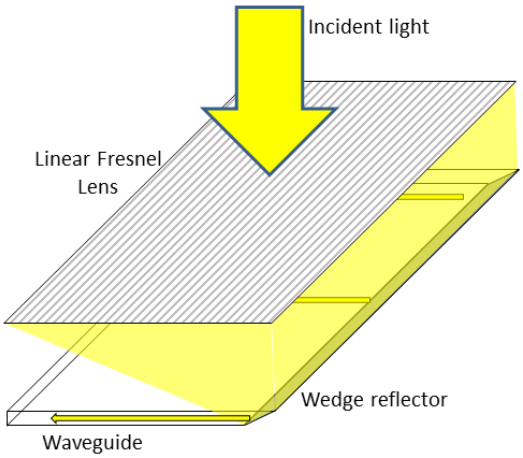

Figure 5.7: The next iteration of the PEC reactor optics would be to use a linear Fresnel lens concentrating light onto a reflective wedge. This would provide a uniform illumination distribution across the photo-electrodes.

5.2 Using a quantum well solar cell as light source

5.2.1 Introduction

An introduction to quantum well solar cells (QWSCs) has been given above in subsubsection 1.3.2.2. At illumination intensities greater than 200 suns, electron / electron-hole recombination is dominated by radiative processes [101, 102, 103]. In essence, at high concentration, QWSCs can be viewed as luminescent devices.

The concept is that a QWSC can generate electricity through normal concentrator PV (CPV) operation, and that its photoluminescence (a light stream viewed as a loss in traditional CPV) is used alongside diffuse light (also viewed as a loss in traditional CPV) to power a water splitting reactor, thus having a module that can generate hydrogen and electricity simultaneously.

The potential of using a QWSC as a luminescent centre was first suggested by Prof. Emer. Keith Barnham. It would be embedded in a waveguide, so that at illumination concentrations of greater than 200 suns, the photoluminescence (PL) emitted can be trapped by total internal reflection and transported to the waveguide edge. The QWSC would replace the cone, and the waveguide would be coated with Lumogen F Violet 570 (LV570) . This optical design forms the basis of a conference proceedings at the 42nd IEEE Photovoltaic Specialist Conference 2015. This design is shown in Figure 5.8. The PL from the QWSC is waveguided to one edge, and luminescent light to the other, where both light streams of differing wavelengths illuminate separate photo-electrodes. Quantum well solar cells are used over other high efficiency solar cells for three reasons: 1) Their radiative efficiency can be established simply from measurements of quantum efficiency and dark current [235], 2) The radiative recombination takes place at the bottom of the quantum well, therefore the PL wavelength is below the bulk absorption edge [105]. This means the bulk of the QWSC is can be largely transparent to the PL. 3) The

wavelength of the PL can be engineered by modifying the quantum well depth [103].

The premise is that the wavelength of the LSC and QWSC emission can be manipulated to match that of the photo-electrode absorption wavelength range. The emission spectra of both an example QWSC and of LV570, and the reflectivity spectra of the wavelength selective mirrors, are shown in Figure 5.9. The QWSC would have anti-reflection coating on its edges, to encourage PL edge emission.

Dr. James Connolly from the Nanophotonics Technology Centre at the Universidad Politecnica de Valencia, Spain, used SOL [236, 237], a dark current solar cell model that can model a QWSC's absorption spectrum and radiative efficiency, to contribute to the QWSC modelling side of this investigation.

In the following investigation, the material of the photo-electrodes will not be discussed, but will be assumed as such: the photo-anode would absorb blue light emitted from the LV570, and the photo-cathode would absorb infra-red light from the QWSC photoluminescence.

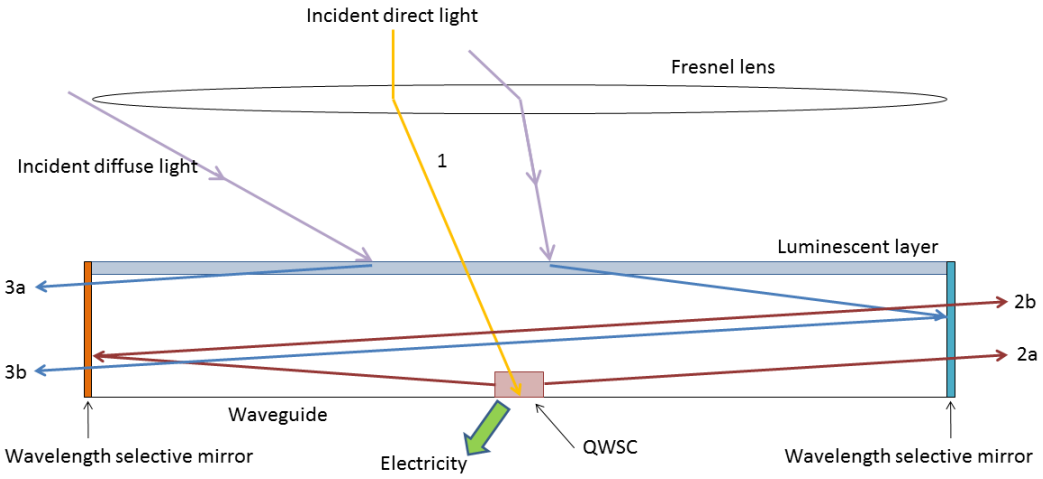

Figure 5.8: A summary of the hybrid QWSC/LSC optics. 1) Direct light is concentrated onto the QWSC. 2) The QWSC photoluminescence is waveguided to one side of the waveguide, either directly (a) or via reflection from a wavelength specific mirror (b). 3) Diffuse light is absorbed by the luminescent layer and waveguide to the opposing edge either directly (a) or via a wavelength selective mirror (b).

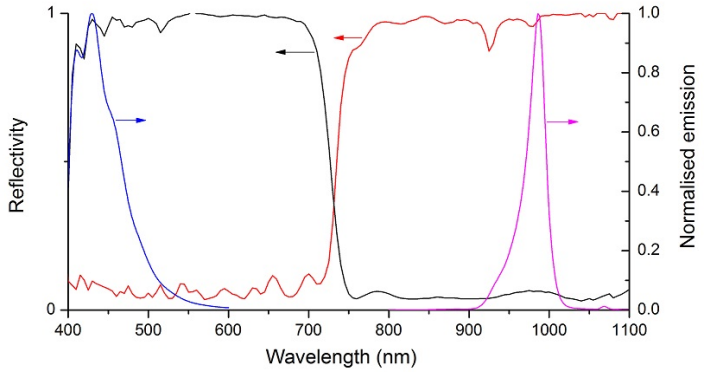

Figure 5.9: Reflectivity of the cold (black) and hot (red) mirror as a function of wavelength at 0° angle of incidence. The LSC emitted light (blue) gets transmitted by the hot mirror and reflected by the cold mirror, whereas the opposite happens for the QWSC photoluminescence (magenta).

5.2.2 Balancing the photon streams from the LSC and the quantum well solar cell

The starting point of the system, to determine the needed optical performance of a QWSC, is to use ASTM G-173 illumination conditions and 500x concentration. Both photon streams must to be equal in intensity as the current through each photo-electrode must be equal. The waveguide dimensions are 20cm x 20cm x 0.5cm.

The luminescent layer uses Lumogen F Violet 570. The luminescent quantum yield is assumed to be 85%, the absorption coefficient is $9000m^{-1}$ and the film thickness is $200\mu m$. Using pvtrace and using diffuse light conditions, the optical efficiency is 2%, giving a photon output of $1.9\text{x}10^{17}\text{s}^{-1}$. This is the necessary photon density needed from the QWSC.

Photoluminescence sample QT1604 was used for these calculations. It was manufactured by metalorganic vapour phase epitaxy (MOVPE) at the EPSRC National Centre for III-V Technologies at Sheffield. It consists of 22 strain-balanced GaAsP/InGaAs quantum wells in a p-i-n structure. It has an AlGaAs window

below the p-doped GaAs emitter layer that can produce some limited transverse waveguiding due to its low refractive index relative to the bulk material. The edges of the PL sample were anti-reflection coated. The cell's quantum efficiency is shown in Figure 1.10, and the full structure can be found in Appendix D.

Dr. James Connolly used SOL to calculate the necessary waveguiding efficiency needed for ASTM G-173, 500x concentration light conditions when the QWSC is at maximum power point.

The model was run for a QWSC running with low and high series resistance scenarios, caused by the electronic contacts. Table 5.6 shows the modelling results. The waveguide efficiency for both QWSC and waveguide together has to be 56% or 29% for the high and low resistance scenarios respectively. This includes the losses caused from absorption of PL within the bulk, trapped light caused by the large refractive index difference between the QWSC ($n \approx 3.5$) and the waveguide ($n = 1.49$), and escape cone losses due to the emission of PL from the QWSC into the waveguide.

Solar cells are designed to contain light. The questions that arise from these results are: how close is a standard QWSC's waveguiding capability compared to the needing waveguiding performance, and if so, can it display LSC-like characteristics?

5.2.3 Experimental determination of concept feasibility by laser illumination

The objective is to determine the waveguiding efficiency of a non-metallised PL sample QT1604 of dimensions 5 x 5 x 0.5mm. Some values calculated by SOL, as well as experimental measurements of power density, are combined to obtain this waveguide efficiency.

	High resistance	Low resistance
J_{SC} at 500x concentration (Am^{-2})	$1.28x10^5$	$1.28x10^5$
Series resistance (Ω)	0.22	0.03
Voltage at MPP (V)	0.998	1.016
J_{rad} at Vmpp (Am^{-2})	1103.25	2119
I_{rad} (A)	$5.41x10^{-2}$	$1.04x10^{-2}$
Max. Photon count (s^{-1})	$3.38x10^{17}$	$6.49x10^{17}$
Desired LSC + QWSC waveguide efficiency (%)	56	29
Edge output (s^{-1})	$1.9x10^{17}$	$1.9x10^{17}$

Table 5.6: Calculating the necessary waveguiding efficiency of QT1604 when illuminated at ASTM G-173, 500x concentration illumination to obtain a PL photon flux of $1.9x10^{17}s^{-1}$. These calculations were made by Dr. James Connolly at the Universidad Politecnica de Valencia, Spain using the SOL modelling software [236, 235].

The radiative efficiency of the QWSC, which is the proportion of recombination that is radiatively dominated, can be determined by fits to the quantum efficiency and dark current on SOL. The radiative efficiency η_{rad} is expressed as:

$$\eta_{rad} = \frac{J_{rad}}{J_{rad} + J_{SRH}} \tag{5.3}$$

where J_{rad} is the radiative recombination current and J_{SRH} is the Shockley-Reed-Hall non-radiative recombination current contribution. The quantum efficiency of QT1604 has been presented previously in Figure 1.10, and the radiative efficiency as a function of device voltage bias is shown in Figure 5.10 as the red line.

The benefits of using a non-metallised PL sample as that it functions under open-circuit voltage V_{OC}, so it does not suffer series resistance losses, which is the cause of the dark current density to plateau at high device bias in Figure 5.10. Under V_{OC} conditions, the current J_V in the cell is zero, therefore the short circuit current J_{SC} equals the dark current J_D due to the expression:

$$J_V = J_{SC} - J_D \tag{5.4}$$

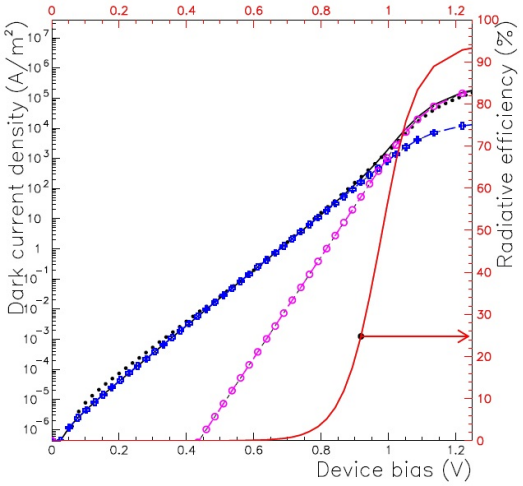

Figure 5.10: Measured (black dots) and fitted (black line) dark IV curve of QT1604. The radiative contribution to recombination (magenta) is a prediction based on the quantum well absorption obtained from the quantum efficiency fit in Figure 1.10. The non-radiative Shockley-Reed-Hall contribution (blue) is seen to dominate at low device bias, but at high device bias, which is related to high concentration, radiative recombination dominates. This data was provided by Dr. James Connolly using the SOL modelling software [236, 235].

The short circuit current J_{SC} is expressed as [107] :

$$J_{\mathrm{SC}} = q\left(\eta_{QE}\frac{P_{opt}}{h\nu}\right) \tag{5.5}$$

where P_{opt} is the incident optical power density and η_{QE} is the quantum efficiency.

The incident power density is known, as explained in subsection 3.4.2. A Millenia V laser, with a wavelength of $\lambda = 532nm$, is used to provide incident light. Using Equation 5.5 and the assumption of $J_D = J_{SC}$ at V_{OC} gives a dark current value J_V. The radiative efficiency η_{rad} is found by referencing Figure 5.10 and the radiative current J_{rad} is found by:

$$J_{rad} = J_{SC} \cdot \eta_{rad} \tag{5.6}$$

The total radiative current I_{rad} is J_{rad} multiplied by the PL sample's top surface area. The total photon count of luminescent light is the total current divided by

the electronic charge q. This number will be ratioed by the measured photon count to produce a waveguide efficiency.

Using the method described in subsection 3.4.2, the spectral irradiance $F(\lambda)$ of QT1604's edge PL was taken. The spectrum was converted from spectral irradiance ($\mu W cm^{-2} nm^{-1}$) into photon flux ($m^{-2} s^{-1}$) by using the expression below and then integrating over the spectrum:

$$\Phi_\lambda = \frac{F(\lambda)}{q \cdot h\nu}\Delta\lambda = \frac{F(\lambda)}{q \cdot (1.24/\lambda(\mu m))}\Delta\lambda \tag{5.7}$$

Using the more sensitive PL measuring setup as described in subsection 3.4.1, the PL peak shape is measured. This enables one to see from an absolute irradiance spectrum what is PL and what is noise. In order to calculate the integrated edge PL photon flux spectrum to obtain a total photon flux, a Gaussian profile was fit onto the spectrum. Knowing that there is no PL signal from 1000nm onwards, all data points can be determined to be noise and so can be removed from the Gaussian peak fitting software. Matlab[238] was used to fit a two-Gaussian profile and integrate the edge PL photon flux spectrum to obtain a total photon flux. The fit is shown in Figure 5.11, including the data points determined to be noise. This photon flux is multiplied by the area of the four edges on the sample to give a photon count. The table outlining the calculations and the waveguide efficiency is given in Table 5.7.

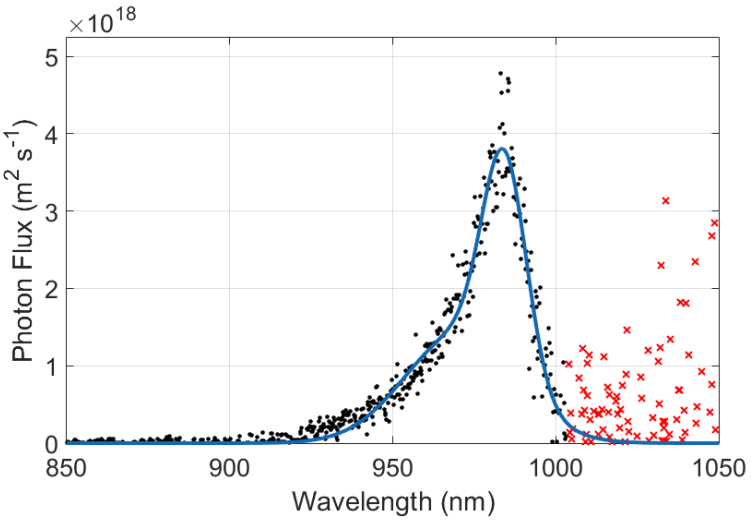

Figure 5.11: Spectral irradiance from the edge of PL sample QT1604 when illuminated. The PL spectrum was determined by a measurement using the setup in subsection 3.4.1, thereby providing evidence that the data points past 1000nm were noise. Matlab was used to fit a two-Gaussian peak to the data (blue line) and integrated to obtain a power density value coming out of a single edge.

Incident power density (Wm^{-2})	1.53×10^5
Device quantum efficiency η_{EQE}	0.92
Dark current J_D (Am^{-2})	6.03×10^4
Radiative efficiency η_{rad}	0.79
Radiative current J_{rad} (Am^{-2})	4.76×10^4
Total radiative current I_{rad} (A)	1.19
Maximum photon count (s^{-1})	7.43×10^{18}
Measured photon count (s^{-1})	1.1×10^{15}
Waveguide efficiency (%)	0.0147

Table 5.7: Measuring PL sample QT1604. With the calculation proces shown above, the final waveguide efficiency for the sample is given as 0.0147%.

The measured waveguide efficiency of the PL sample QT1604 was 0.0147%: three orders of magnitude less than the needed value to validate the concept of using the PL from a QWSC for secondary processes. There are some reasons for highly non-ideal waveguiding in this particular sample. Firstly, the base and substrate of the sample comprises of n-doped GaAs, where free carrier absorption is around $\alpha \approx 300m^{-1}$ [239]. Using Beer-Lambert absorption, across the length of the sample this corresponds to 77% absorption of the PL. Light caused by radiative recombination can be trapped within the sample due to its high refractive index of $n = 3.5$.

The spectrometer aperture was not optically coupled to the sample edge, therefore the air/semiconductor interface provided an escape cone angle of only 16.6°. High absorption within the bulk material and light trapping due to a high refractive index cause for massive PL loss.

5.2.4 High concentration full spectrum light into a QWSC embedded in a waveguide

5.2.4.1 Experimental setup

This experiment was undertaken at SUPSI, using the same equipment and setup as in section 3.5. The waveguide with a reflective cone was replaced with a waveguide with a square cavity, in which the QWSC can be embedded. The cavity is flooded with index matching fluid (Cargille acrylic matching liquid, refractive index n=1.49 at 633nm) before embedding the QWSC. The same positions are used (P5 - P1) to measure photoluminescence (PL) from the waveguide edge.

Isolating PL from the incident light spectrum

There is significant scattered incident light relative to the PL of the QWSC due to the cavity in the waveguide, which reaches the spectrometer. An irradiance spectrum were taken with the waveguide without an embedded QWSC, as shown by the schematic in Figure 5.12a. The irradiance spectrum taken with an embedded QWSC, as shown by the schematic in Figure 5.12b, is subtracted by the waveguide spectrum to obtain one with less noise. This is shown in Figure 5.13. This is then fed into Matlab, and its curve fitting software was used to fit a Gaussian to the photoluminescence peak. Outlying data points can be removed using the software, as demonstrated in Figure 5.14, to improve the fitting accuracy. The Gaussian peak produced from the software is integrated to obtain the intensity of the PL at the waveguide edge.

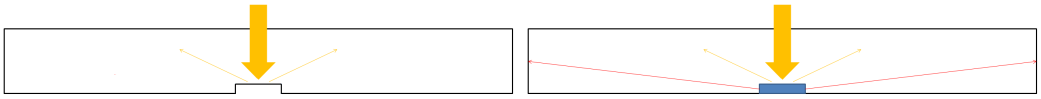

(a) Scattered light (b) Scattered and PL light

Figure 5.12: Two measurements are taken. Firstly background and scattering light is measured (a). This is subtracted from the light obtained when a PL sample is present (b).

Calculating Watts in vs Watts out

In order to obtain the Watts out of the whole edge for the PL, this value is multiplied by a scaling factor and integrated spatially according to the emission profile at the edge. This process is explained in subsection 3.5.1.

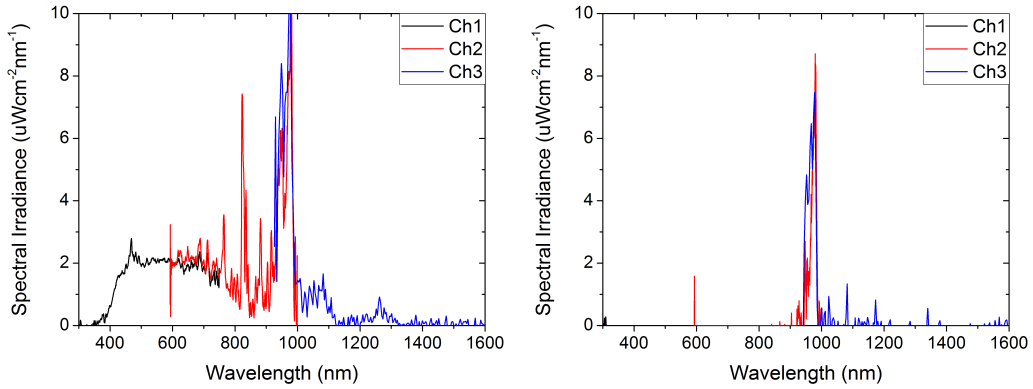

(a) Raw spectrum (b) Isolated PL spectrum

Figure 5.13: The raw spectrum obtained by the Avantes spectrometer for QWSC sample QT1604 at position P5 (1740 Suns). The spectrometer has three channels, each optimised for their spectral band (400-750nm for channel 1, 600-1000nm for channel 2 and 950-1600nm for channel 3). The scattered waveguide light spectrum is subtracted to obtain an isolated PL spectrum, shown in (b)

5.2.4.2 Results

A waveguide of dimensions 20 x 20 x 0.5cm had a 3 x 3 x 0.5mm cavity drilled into the middle. The cavity was flooded with index matching fluid before inserting the sample. The same illuminations were used as the cone in the waveguide: 1741, 907, 298, 118 and 20 Suns. The measured spectra are shown in Appendix C. There was no discernible PL measured for 20 Suns illumination.

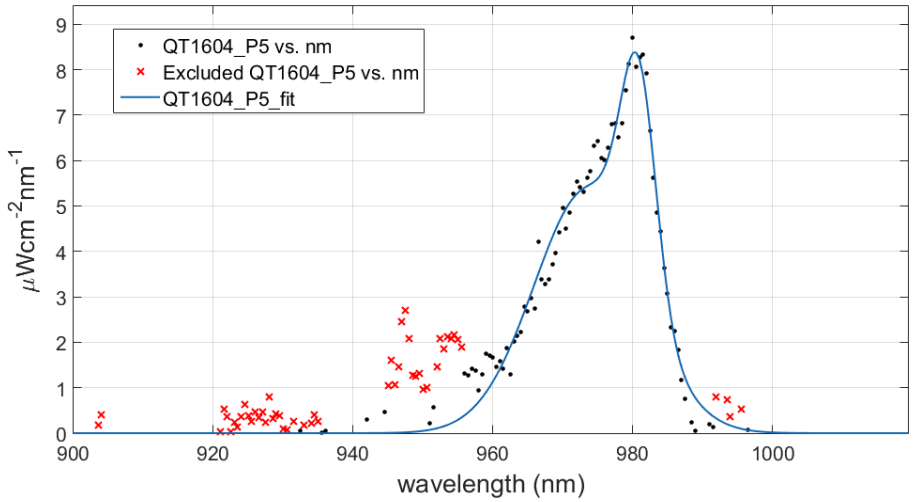

Figure 5.14: Matlab curve fitting function onto the isolated PL peak. Like Figure 5.11, the PL peak shape is known, meaning data points which do not correspond to the peak at 980nm can be considered noise. They are removed from the fitting algorithm (shown by the red crosses).

The waveguide had reflectors on three of its edges, and the PL sample is assumed to be an isotropic light source. The integrated PL values in Wm^{-2} and the Watts out vs Watts in ratio is given in Table 5.8. The optical efficiency of the QWSC/waveguide system is of the order of 10^{-2} %, with a power density at the waveguide edge of the order of 1 Watt. This is again orders of magnitude less than is needed for any realistic use of PL.

Incident Suns	PL power density at waveguide edge (Wm^{-2})	Watts out vs Watts in (%)
1741	1.31	0.007
907	1.21	0.013
298	0.47	0.015
118	0.14	0.011

Table 5.8: Integrated power density, and the optical efficiency (Watts out vs Watts in) for QT1604 under high concentration illumination

5.3 Conclusion

This chapter introduced the double-illuminated photoelectrochemical (PEC) reactor for solar hydrogen production. The novel aspect of the reactor is that both electrodes are photo-active and are both illuminated independently. The reactor windows are normal to incident light, giving an opportunity to use waveguiding optics to provide these light streams.

A triple-junction photo-cathode is used in the PEC reactor, which requires full spectrum illumination. Direct concentration of incident light is possible by embedding a reflective cone inside a waveguide, and using a Fresnel lens to concentrate direct sunlight onto the cone. This light will be reflected into the waveguide, where it is trapped due to total internal reflection and waveguided to the photo-electrodes.

Pvtrace was used to model a reflective cone embedded in a waveguide. The cone was modelled as a specular and Lambertian reflector, and the incident light was modelled at normal incidence. In a real optical system, one edge of the waveguide will be coupled into the PEC reactor and the other three edges have reflective material on the edges. The optical efficiency of the one photoactive edge of the waveguide increases from 22.4% to 49.6% when a waveguide with a specular reflective cone has reflector edges. For a waveguide with a Lambertian reflective cone, the optical efficiency rises from 13.1% to 25%.

The performance cone in a waveguide was measured experimentally at high concentration illumination. The cone was drilled into a PMMA waveguide with a slope of 45°. It was an imperfect cone with striations across the wall, and had no reflective material underneath it so that the only reflection would be caused by the waveguide/air refractive index difference. Because of this, the optically efficiency of the system was an order of magnitude less than that given by the pvtrace model. The increase in edge intensity when reflectors were added to the other three edges

of the waveguide suggest that the cone is more Lambertian in nature.

A full demonstration PEC reactor with reflective cone / Fresnel lens optics was build and tested outdoors. The middle of the waveguide edge produced 1.5x and 2.5x concentration, without and with edge reflectors respectively. The profile of the light across the waveguide edge confirms that the drilled cone was behaving in a Lambertian manner. 2.5x concentration out of the waveguide edge means there is a factor of 4 improvement to be made. This can be achieved by using a smooth, specular reflecting cone as well as using better edge reflectors. The illumination profile across the waveguide should ideally be uniform, therefore the next iteration of the optics would be to use a linear Fresnel lens concentrating light onto a reflective wedge.

A concept was proposed that a quantum well solar cell (QWSC) can be used as a luminescent centre within a waveguide, thereby being an alternative to a reflective cone. The aim is for the photoluminescence (PL) exiting from a QWSC to have equal intensity to the light emitted at the edge of a traditional thin-film UV-absorbing, blue-emitting LSC. This would be to allow the QWSC, which is illuminated by concentrated direct light, to simultaneously a) generate electricity and b) act as a luminescent centre as at high concentration levels, recombination losses are dominated by radiative processes. The top of the waveguide would be coated in Lumogen F Violet 570 to absorb diffuse light as a conventional LSC. Using calculations from the modelling software SOL, it was found that in order to balance these two light intensities, 29% - 56% of the PL produced would need to be waveguided out of the QWSC and onto the waveguide edge. Practical measurements of edge PL of a typical QWSC with uniform illumination of laser light gives a waveguide efficiency three orders of magnitude less than is needed as given by SOL. Further measurements were made of high concentration, full spectrum illumination on a QWSC embedded in a waveguide. The optical efficiency of the system was 0.007%

- 0.015%, again being three orders of magnitude less than what is needed to match LSC light emission.

These measurements were all done with the QWSC at open-circuit voltage, meaning all charge carriers recombine. With the QWSC at its maximum power point and generating electricity, the amount of photons generated through radiative recombination will be much less. The main improvements that can be made to the QWSC are a) removing its substrate and b) optimising the QWSC to photoluminesce preferentially sideways through its edges. Furthermore the QWSC was initially chosen as a luminescent centre because the photo-cathode of the reactor was to be Copper-indium-gallium-selenide (CIGS). This was determined to be unsuitable for photoelectrochemical operation, and once it was replaced with a triple-junction structure which needs full-spectrum illumination, the QWSC could not be used.

Chapter 6

Optical Funnel for Algae Raceway Ponds

Algae raceway ponds are the cheapest method of large scale algae farming for biofuel production. They are not without their limitations, one of them being the fact that water maximally saturated with algae has an absorption coefficient of the order of $100m^{-1}$. This means that only the top few centimetres of a pond, with depths of 20-40cm, are actually effective in algae growth. In this chapter, a retrofitting optical funnel is introduced as a novel solution to increase the "effective depth" of these ponds by providing constant illumination throughout the depth of the pond. This would increase algae growth rates, and therefore, total biofuel production. PVtrace is upgraded to include mesh geometries. A mesh design metric is used in conjunction with a genetic algorithm, developed by Tom Wilson in the QPV group, to firstly demonstrate its ability as an effective light diffuser, and secondly to demonstrate the ability for design optimisation for various scenarios such as illumination conditions and different algae species.

6.1 Designing the optimisable luminescent solar diffuser for light distribution in a raceway pond

A recent review of raceway ponds presented investigation trends in many aspects of its design, however as pointed out in the previous section, there is a complete lack of investigation regarding innovative optics for raceway ponds. Discussions on raceway optics revolve solely around the trade-offs in pond depths with biomass production [128].

As discussed previously in subsection 1.4.4, the main issues regarding optics in raceway ponds are that the high optical density of algae mean that only the first few centimetres from the surface of the pond receive sufficient light to grow. As was shown pictorially in Figure 1.16, the algae absorb above and beyond the light energy ($\sim$100 Wm^{-2}) that is needed, preventing algae below it to harvest the light, whilst at the same time damaging itself and releasing the excess energy as heat, thereby increasing the evaporation rate of water in the pond. With algae residing in dark optical zones for extended periods of time, biomass growth is stunted. An ideal illumination profile should be constant, at a lower intensity, throughout the pond depth.

This chapter proposes the idea that luminescent materials can be used in conjunction with novel optical design to create a luminescent solar diffuser (LSD) to increase uniformity of illumination across the depth of a raceway pond. The concept can be seen as utilising an LSC loss mechanism, top/bottom emission loss, into a useful attribute.

The concept of manipulating optical transport in algae raceway ponds is truly novel. The author developed the design and the necessary tools in pvtrace to build the optical model of the first ever raceway pond optical system.

6.1.1 Concept

The objective of the luminescent light diffuser (LSD) is to capture incident sunlight from the surface of the pond, and redistribute it evenly across the depth of a raceway pond, thereby giving a uniform illumination profile across the depth of a raceway pond. Being a standalone device, it can be retrofitted to any existing raceway pond. This would increase the algae growth rates by:

- Spectral conversion of less efficiently used short-wavelength incident light into that of a more usable wavelength,
- Preventing excess illumination onto the first few centimetres of the pond, thereby decreasing photosynthetic machinery damage and thermal emission. This in turn decreases evaporative losses in the pond,
- Reducing the volume of the dark optical zone by waveguiding the excess light from the top surface into the deeper sections. This effectively increases the illumination area/volume ratio of the pond.

The diffuser is a solid transparent optical funnel, made of a cheap transparent material such as polymethyl methacrylate (PMMA). The top surface of the diffuser is coated with a thin, highly-doped luminescent layer which absorbs all incident light. Some of the luminescent light is lost by emission out on the upper volume of the pond. The remaining light travels down inside the optical diffuser and exits into the algae culture at a deeper depth. The bottom of the diffuser has a reflective cone to direct light outwards into the algae culture. This is demonstrated in Figure 6.1. The lower refractive index between the LSD/algae culture (1.5:1.3) interface compared to the LSD/air (1.5:1.0) interface encourages light to diffuse into the algae culture. The LSD can either be circular, in which many standalone devices can be arranged in an array as shown in Figure 6.2a, or can be a linear 2D funnel that stretches along the length of the raceway pond, as shown in Figure 6.2b

The LSD can be modelled on pvtrace, and its design can be optimised according to various environmental parameters, such as the depth of the raceway pond into

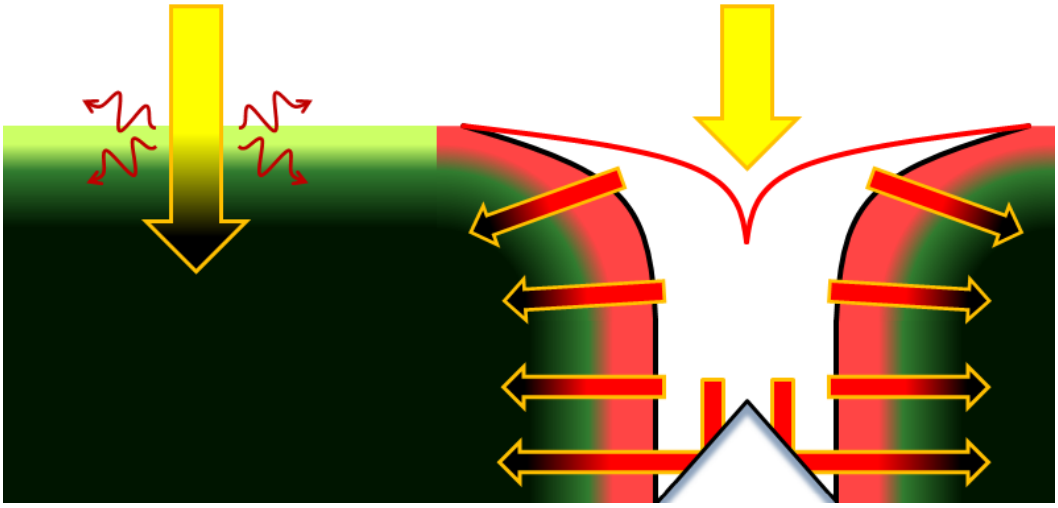

Figure 6.1: Schematic for retrofitting conventional raceway ponds with a luminescent solar diffuser (LSD, right), to mitigate the low penetration of incident light into an algae pond (left). This is looking at a cross section of a raceway pond. The LSD is a solid clear funnel (shown white), with the top surface coated with luminescent material (shown red). At the bottom of the funnel there is a reflecting cone. The top surface rest on the surface of the pond. The LSD is used as light distributor, taking light from the top surface, spectrally converting it into a more useful wavelength for algae, before diffusing it throughout the depth of the pond.

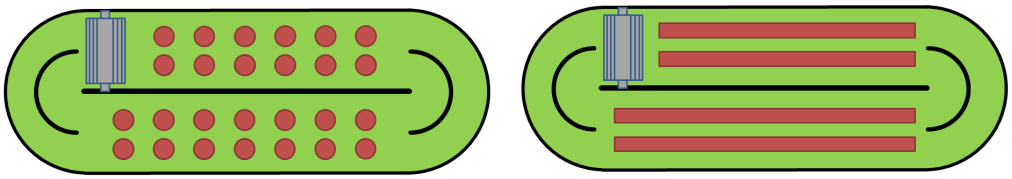

(a) Standalone circular LSDs arranged in an array in a raceway pond

(b) A linear pond-length LSD

Figure 6.2: Two ways in which a luminescent solar diffuser could be incorporated into a raceway pond, as many standalone circular devices (a) or a linear array (b). The view is looking at raceway ponds from above.

which it will be fitting, or the species of algae, of which their absorption densities at peak saturation can differ by an order of magnitude.

A set of design parameters and their respective limits are fed into a genetic algorithm in order to find the optimal shape for the LSD in which to produce a constant illumination profile across the depth of the pond.

6.1.2 Model construction on pvtrace

6.1.2.1 The LSD

The circular LSD was initially constructed using many slices of truncated cones to form a hyperboloid structure and a cylinder as the base, as shown in Figure 6.3a. This method of construction was quickly dismissed due to the extended simulation time needed to calculate Fresnel relations for the light ray at each slice interface.

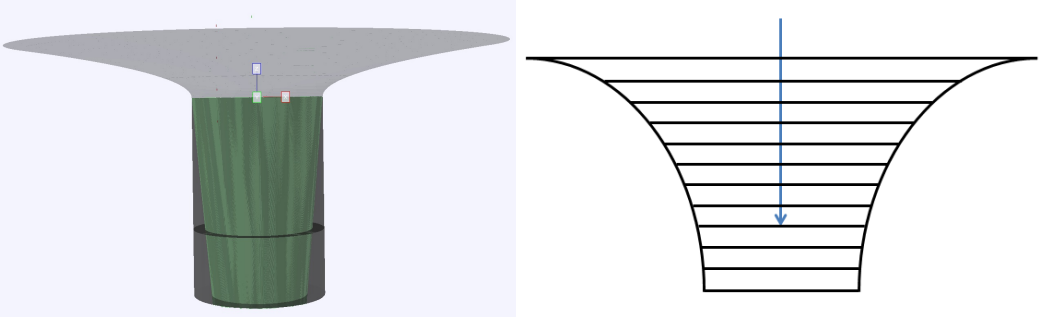

(a) Pvtrace visualisation of an LSD created with truncated cone slices

(b) Diagram of a light ray passing through many interfaces within the LSD.

Figure 6.3: Initial construction of the LSD using slices of truncated cones. This was a time consuming construction, due to a single pass of light requiring many Fresnel relation calculations as it passes through continuous slice interfaces.

The second construction strategy used was to create a mesh grid, using the already-existing Polygon class in pvtrace and the added PolygonMesh class and MeshGen module. The benefit of using a mesh is in the greater flexibility of generating more complex geometries such as the linear LSD array. The LSD design is symmetric both in 3D and 2D which simplifies the mesh construction as it can be designed around an axis and rotated in 3D, or reflected in 2D.

For the 3D mesh geometry, a parametric equation is defined. The base point is plotted first respective to an axis and rotated around it for a full 2π rotation. The next point is plotted along the axis, and rotated again by 2π. Each slice has a N number of points. This keeps going until all points are placed and a mesh "dot-to-dot" is generated, with rotational resolution N and vertical resolution M. All the points are appended to a list so that it contains $N \times M$ points. The first two

points of the bottom slice are chosen along with the first point of the upper slice up to create the first polygon. In the list this corresponds to $[n_0, n_1, n_N]$. Next, the first two points on the upper slice and the second point on the bottom slice is chosen, corresponding to $[n_N, n_{N+1}, n_1]$. This then carries round for 2π and moves up one slices. This is shown in Figure 6.4.

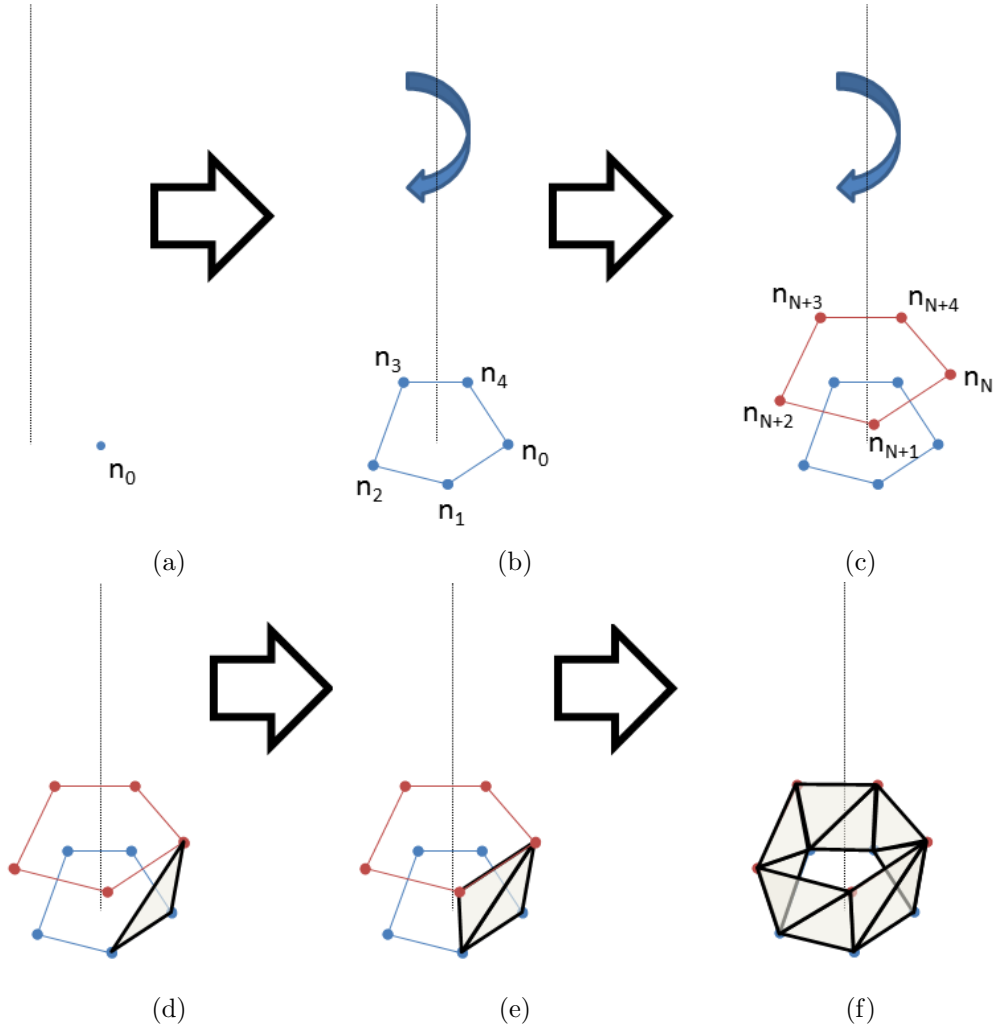

Figure 6.4: Three dimensional mesh construction of a LSD. Only the first two layers of potentially many are shown. A vertex away from an axis is made (a), and it is rotated around by 2π, with the number of vertices in the rotation determined by the resolution of the mesh (b). A second layer of vertices is rotated round at a distance above the other slice again determined by the dimensions and resolution of the mesh (c). All the vertices are appending to a list as they are created. To make polygons, an iteration is carried out where firstly vertices $[n_0, n_1, n_N]$ are used as polygon points (d). Secondly, vertices $[n_N, n_{N+1}, n_1]$ are used (e). This continues round until the final vertex n_{NM} when all polygons are made (f)

For the 2D mesh geometry, an array of points are plotted along an axis according to a shape function. The array of points are then mirrored against the axis. The top and bottom layers are created like in the 3D mesh. Whilst the linear LSD array geometry can be simplified to 2D raytracing due to uniformity in the pond-length axis, the main benefit of modelling in 2D is the decrease in simulation time. This becomes important in subsection 6.1.5.

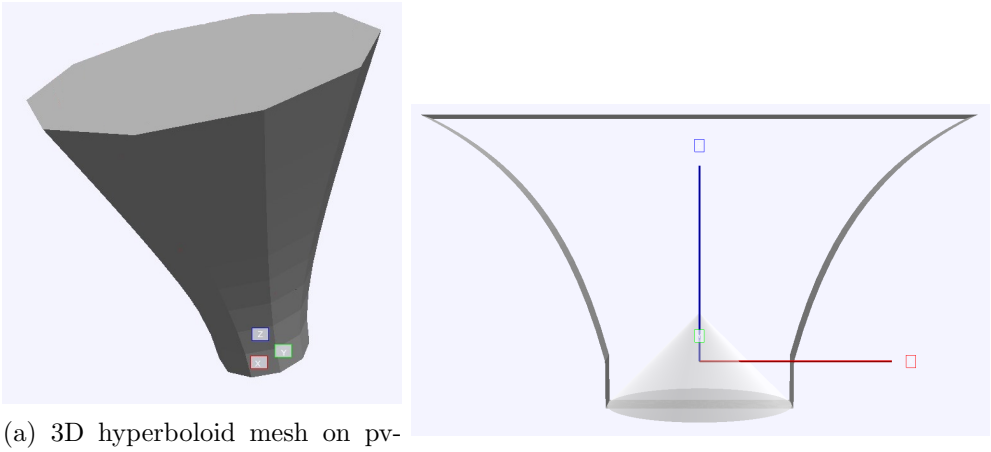

(a) 3D hyperboloid mesh on pvtrace

(b) 2D hypboloid mesh on pvtrace

Figure 6.5: Two- and three- dimensional hyperboloid meshes on pvtrace. The mesh generator utilises pvtrace's Polygon class to form a shape. The reflective cone can be seen in the 2D hyperboloid.

6.1.2.2 The Algae

The single-celled algae *Chlorella Vulgaris* (*C. Vulgaris*) was used as the species from which its optical properties were taken. The mass cultivation of microalgae was pioneered in the early 1950s with this species [240], it was one of the first species to be used in raceway ponds [241], and it is still used as an example species for economic modelling of algae farms [131].

The LSD is surrounded with a volume of algae culture, with a refractive index of water, and algae absorption spectrum and coefficient data taken from Hannis (2013) [125], shown in Figure 1.14. The algae volume follows the LSD shape function. It is constructed in the same manner as the LSD. It is split into various layers, the

number of layers being independent of the vertical resolution of the LSD. Each layer is given an identification so that pvtrace can log into which layer a photon has been absorbed. The pvtrace visualisation of the LSD and the algae layers are seen in Figure 6.6.

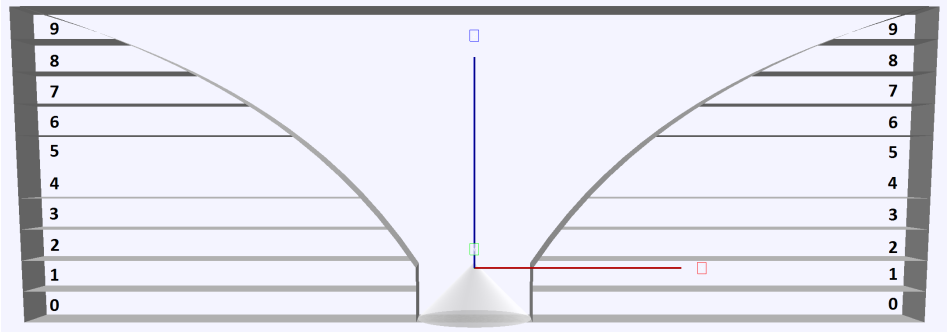

Figure 6.6: Layers of algae culture surrounding a 2-dimensional LSD. In this case the culture is split into 10 different layers.

6.1.2.3 Simplifications and assumptions

Light absorption from water: The absorption coefficient of water is $0.01m^{-1}$ at 400nm, and rises to $1m^{-1}$ at 800nm [242]. It is therefore assumed negligible in comparison to the algae's absorption coefficient of $100m^{-1}$.

Scattering: Berberoglu *et al.* (2006) investigated the effect of scattering in photobioreactor design [243]. When it comes to modelling light transport within a reactor, they concluded that scattering is unimportant when the scattering makes up less than 50% of the total light extinction, and is in the forward direction. However as scattering becomes the dominant form of light extinction, it does become important and furthermore, the difference between scattering mechanisms (isotropic/anisotropic, etc) become more pronounced in models. As seen in Figure 1.14, scattering is the majority cause of light extinction.

Scattering characteristics are dependent on a myriad of factors. Shape and morphology of the species plays a large, and unpredictable role. It has been shown

that two algae species with similar shapes produced a different scattering patterns, whilst two other species with different shapes (cylinder and sphere) had similar scattering patterns [244]. Aspects of morphology that affect scattering patterns can be whether the algae has a cell membrane or wall, or the existence of, and variations in, gas vacuoles [244, 245, 246]. The location and size of the cell core, a.k.a. the cell's inner machinery [247], as well as the cell size [248], play a part in scattering. On top of all this, the scattering pattern can also be wavelength-dependent [249].

All in all, simple scattering profiles like Mie scattering, which assume spherical, homogeous particles, are not good approximations for algae scattering [245, 249, 250].

Because the objective of this chapter is merely to demonstrate the capability of the LSD to be optimisable, the accuracy of the algae scattering characteristics is not a priority. On top of the modelling minefield that is algae scatter patterns, adding scattering as a property of the LSD simulations also increases simulation times, which is explained in more detail in subsection 6.1.5. For these reasons, scattering will be ignored and the peak absorption coefficient value for the algae will take the peak extinction coefficient value.

Optically perfect and clean surfaces: Pvtrace assumes optically perfect surfaces. A further assumption is that the LSD surfaces will always be clean. In reality, a considerable amount of algae can stick onto a reactor surface [142]. This changes the optical density of the algae culture towards more dense, as algae stuck on the LSD surface is of a much higher concentration than in the water.

6.1.3 Design parameters and shape function

The LSD design parameters are limited to the specification of the raceway pond into which it will be inserted. Initial design parameters for the LSD are:

- The height of the LSD, H,
- The radius of the top of the LSD, R_{top},
- The radius of the base of the LSD, R_{base},
- The curvature of the funnel section, K,
- The height ratio between the funnel section and the straight section, r_{height},
- The angle ϕ, and therefore also the height, of the reflective cone. This is because its radius is fixed to that of R_{base}.

A secondary design revolves around the top surface of the LSD to have its own curvature and height ratio. This brings it more in line with the design shown in Figure 6.1. For there will be two height ratios, an outer one which is the height ratio between the funnel and the straight section, and an inner one which is the height ratio between the centre of the top surface and the base of the LSD. There are two curvature values, again an outer and an inner value. This is shown in Figure 6.7b.

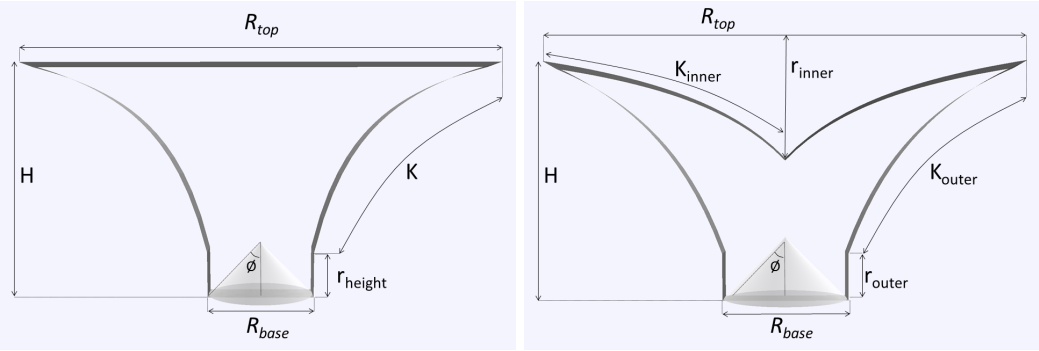

(a) A four-parameter LSD (b) A six-parameter LSD

Figure 6.7: The different parameters of a four- and six-parameter LSD design. A four-parameter LSD has: the height H, the top radius R_{top}, the base radius R_{base}, the height ratio between the funnel and the straight sections r_{height}, the curvature of the funnel section K and the angle of the reflective cone ϕ. A six-parameter LSD has: the height H, the top radius R_{top}, the base radius R_{base}, the height ratio between the funnel and the straight sections r_{outer}, the height ratio between the top surface and the base of the LSD r_{inner}, the curvature of the outer funnel section K_{outer}, the curvature of the inner funnel section K_{inner} and the angle of the reflective cone ϕ

The function of curvature for the funnel is a plateau curve, whereby:

$$y = \frac{x}{K + x} \tag{6.1}$$

where K is the curvature value. The variations which K can have on the curve function are demonstrated in Figure 6.8.

Some parameters will stay fixed. The height of the LSD will depend on the depth of the raceway pond into which it is fitted. For the rest of the thesis, this height will be fixed at 30cm. The angle of the reflective cone will stay at 45° and the radius stays fixed at the LSD base radius. The optical density of the algae will also be fixed at 100m^{-1}. This brings down the number of variable parameters to either four: R_{top}, R_{base}, K and r_{height}, or six: R_{top}, R_{base}, K_{inner}, K_{outer}, r_{inner} and r_{outer}.

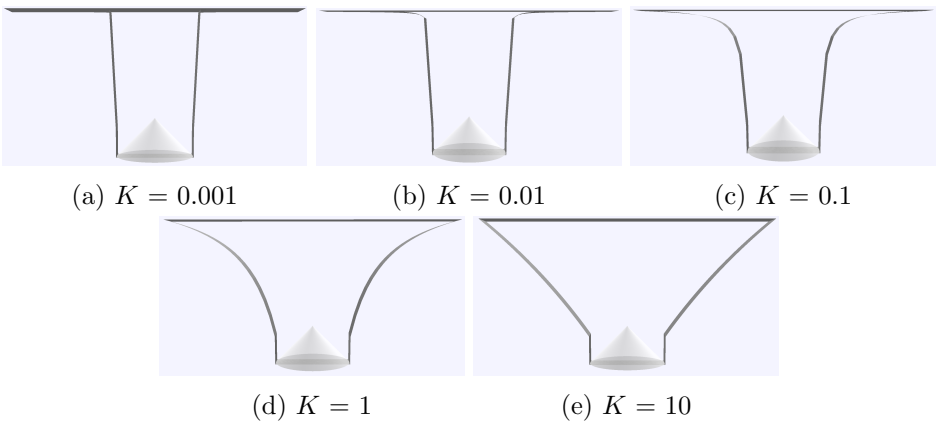

(a) $K = 0.001$ (b) $K = 0.01$ (c) $K = 0.1$

(d) $K = 1$ (e) $K = 10$

Figure 6.8: Funnel curvatures determined by the curvature constant K in Equation 6.1.

6.1.4 LSD figure of merit

The LSD's objective is to provide uniform illumination across the depth of a pond. This goes hand in hand with a uniform light absorption profile in the algae culture. Therefore, as a function of pond depth, the profile of light absorbed is a straight line. This is shown as the blue line in Figure 1.16.

We can therefore say that the function for perfect illumination $f_{illumination}$ is:

$$f_{perfect} = \frac{P_{incident}}{L_{pond}} = constant \tag{6.2}$$

where $P_{incident}$ is the incident light intensity and L_{pond} is the pond depth. The figure of merit is a root-mean-square (RMS) goodness-of-fit parameter, χ^2_{RMS}:

$$\chi^2_{RMS} \equiv \sum \left[\frac{y_i - y(x_i)}{N_{layers}} \right]^2 \tag{6.3}$$

where y_i is the measured value from the simulation, $y(x_i)$ is the ideal value and N_{layers} is the number of algae layers in the simulation. $y(x_i)$ and $f_{perfect}$ are expressions of the same idea of constant, ideal illumination. Using RMS also penalises heavier deviations from the ideal. The objective for LSD optimisation is to get χ^2_{RMS} as close as possible to zero.

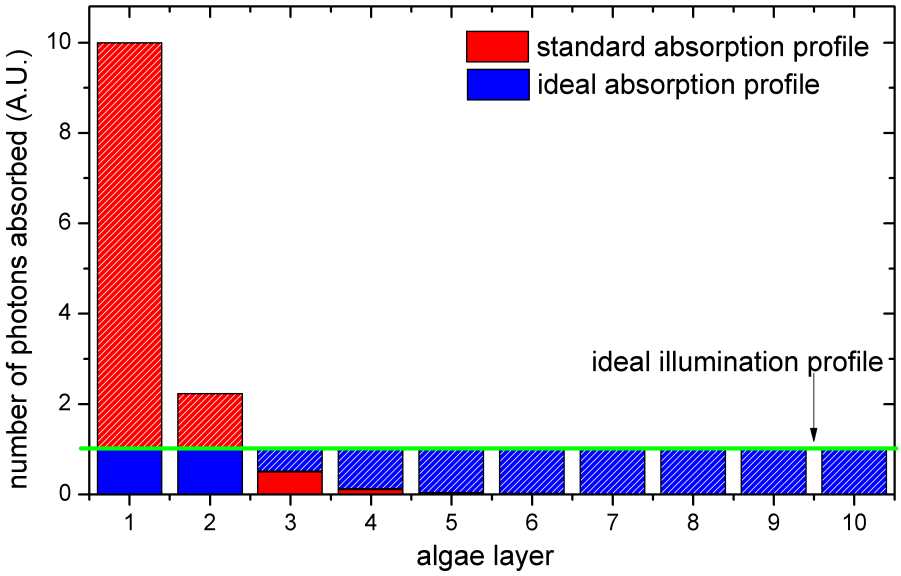

Figure 6.9: Graphical representation of determining goodness of fit on pvtrace using an example Beer-Lambert illumination profile (red histogram). The algae layer numbers correspond to the layers in the simulation. Algae layer 1 is the top, and 10 is the bottom. The ideal illumination profile is shown as the green line, which is the total number of photons absorbed in the system divided by the number of algae layers. The hashed areas of the bins indicate the number of photons that deviate away from the ideal number of photons absorbed (blue histogram). Equation 6.3 is used to then give a goodness of fit number.

6.1.5 Practical application of the genetic algorithm to the LSD

The greater the population size, the greater the probability that the initial state of the population contains the chromosome that gives optimum fitness and the faster the generations will take to convergence on a solution. A greater population size however, means that the whole optimisation code will take longer to complete. Furthermore, after a certain population size, it actually takes more generations for an optimum solution to be found [251]. The size of population scales with the number of optimisable parameters. Optimum fitness values for 4 optimisable parameters start to converge at around 20 generations. Further generations achieve only minor refinements to the optimal parameters.

The GA in itself takes a matter of seconds to run the optimising process between generations. Each member however is a separate pvtrace simulation. A 2D simulation run of 10,000 photons where the algae is assumed to be non-scattering takes around 30 minutes on a Ramdisk-enabled, 16-core HP Z820 computer. This means for a run of 20 generations using a population of 50 members, a total run takes around 20 days. A 2D simulation with algae scattering properties increases the run time to 53 days. A 3D simulation run time would take half a year and this increases up to almost a year if algae scattering is included. Once the LSD is proved in the field, and the concept merits further modelling to improve design optimisation, a faster raytracer should be used along with a more powerful computing setup, like a computing cluster. Pvtrace is currently used because a) it is free and b) time constraints prevented re-writing a newer faster raytracer.

The most viable option is to run the genetic algorithm with a 2D, non-scattering algae model to find the optimal parameters. An LSD with semi-optimal parameters was run for scenarios of 2D and 3D, with scattering and non-scattering behaviour in algae. For simplicity, Mie (isotropic) scattering was used as the scattering mechanism. The light absorption profiles for the four scenarios are shown in Figure 6.10,

with the χ^2_{RMS} figure of merit and percentage of incident light absorbed in Table 6.1.

The genetic algorithm uses the 2D, no scatter scenario. Whilst the the 3D no-scatter scenario has a significantly higher χ^2_{RMS} value (56%), the absorption profile across the funnel depth is the most similar. Both scattering scenarios had very different absorption profiles, both to the 2D non-scatter scenario, but also to each other. Most importantly, significantly less light was logged as absorbed in total. This is attributed to light being scattered out of algae back into the environment.

The reality is that the amount of light actually absorbed and used for photosynthesis is somewhere between the no-scatter and the Mie-scatter scenarios. This remains an area of doubt without a reliable scattering model for an algae species.

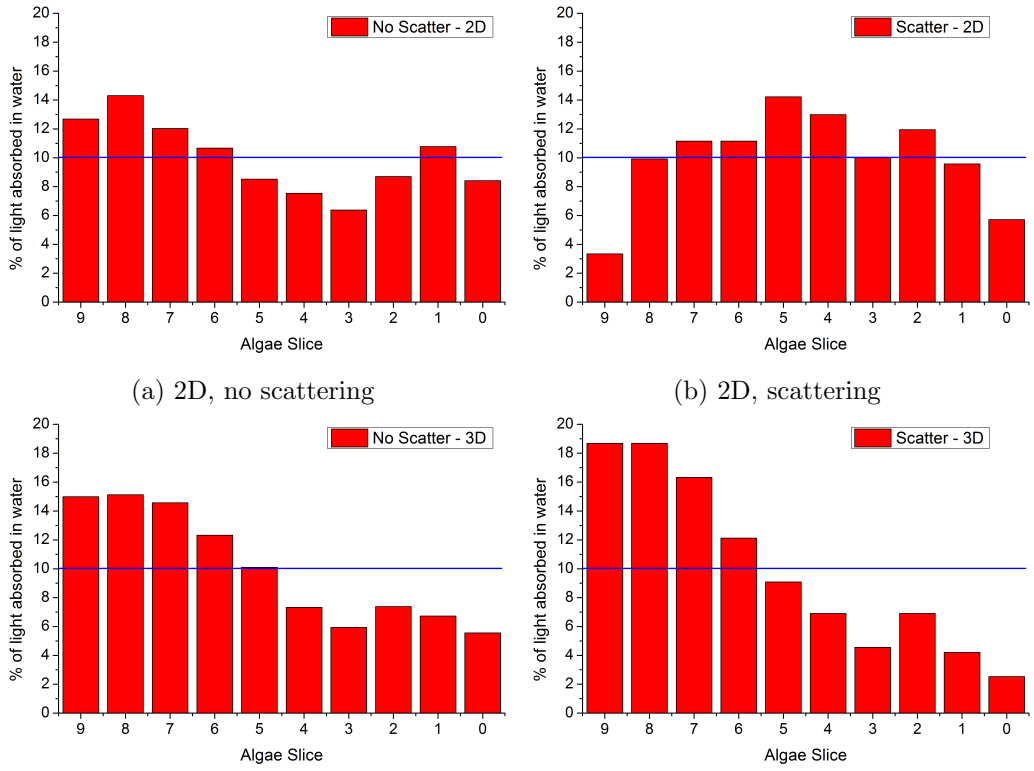

(a) 2D, no scattering

(b) 2D, scattering

(c) 3D, rotationally symmetric, no scattering

(d) 3D, rotationally symmetric, scattering

Figure 6.10: Testing the similarity in results between 2D and rotationally symmetric 3D designs, as well as including or not including light scattering as an algae property. The 2D, non-scattering scenario was is partially-optimised. The blue line indicates the optimal absorption profile.

	χ^2_{RMS}		% Light absorbed	
	2D	3D	2D	3D
No Scattering	2.38	3.73	68	71
Scattering	3.10	5.79	16	13

Table 6.1: Figure of merit for an LSD of equal parameters run for 2D, 3D, scattering and non-scattering behaviour scenarios.

6.2 Results

6.2.1 Model conditions

The top surface of the LSD is coated with a highly-doped Lumogen Red F 305 luminescent layer. The main body of the LSD is clear PMMA, with a homogeneous absorption coefficient of $0.3m^{-1}$. The angle of the reflective cone is set to 45° and its diameter is that of the LSD base width. The total height is fixed at 30cm and the algae density is fixed at 120m^{-1}. Ten algae layers are used to calculate the figure of merit χ^2_{RMS}. The direct and component photon flux spectra of ASTM G-173 are used for planar and diffuse light sources respectively. These spectra are cut off at $\lambda > 800nm$ due to algae's absorption limit.

A population of 50 members was used, and 20 generations were run for the genetic algorithm.

Without a LSD, the χ^2_{RMS} value for pure algae is 25.1, and 90% of incident light is absorbed. The 10% of light not absorbed is due to surface Fresnel reflection, and light with a wavelength close to 800nm, where the optical depth is not high, propagates through the volume.

6.2.2 A 2D, four-parameter LSD with C. Vulgaris

The initial LSD design involved only 4 parameters, with a flat top part as shown in Figure 6.7a. The parameter limits are defined in Table 6.2.

The results are shown below. The parameters for planar and diffuse light conditions are very similar, however the figure of merit χ^2_{RMS} and percentage of light absorbed differes between the two. The χ^2_{RMS} values are not perfect values of zero, with non-perfect values of $\chi^2_{RMS} = 2.10$ and $\chi^2_{RMS} = 2.98$ for planar and diffuse conditions respectively. For this reason, a more complex, 6 parameter model was constructed, with the parameters described in subsection 6.1.3, and the results shown below in subsection 6.2.3. The benefit to this result however is that the design is suited for both planar and diffuse light sources. This is less of a case in the optimal 6 parameter model.

	Minimum	Maximum
Base radius	0	0.1
Top radius	0.1	0.5
Height ratio	0	1
Curvature	0.001	10

Table 6.2: Physical parameter limits for the four parameters of the LSD

	Planar	Diffuse
Base radius	0.10	0.10
Top radius	0.309	0.336
Height ratio	0.206	0.206
Curvature	2.751	2.897
χ^2_{RMS}	2.10	2.98
Total light absorbed	71.5% %	59.6 %

Table 6.3: Optimal parameter limits for a four parameters LSD, and their respective χ^2_{RMS} and total light absorbed by the algae

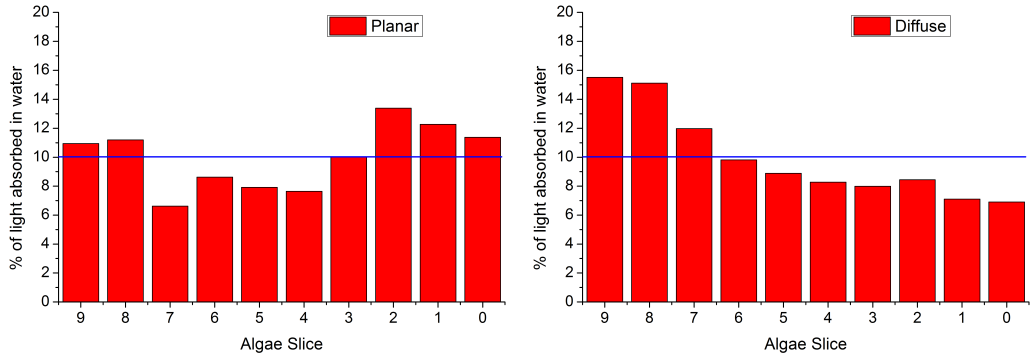

(a) Planar (b) Diffuse

Figure 6.11: Absorption profile of algae for planar and diffuse (isotropic) light conditions for a 4 parameter LSD. The blue line indicates the optimal absorption profile.

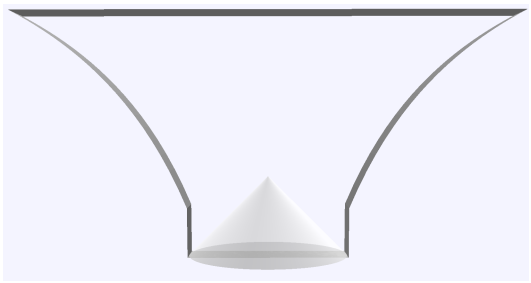

Figure 6.12: A visualisation of the 4 parameter LSD after 20 generations of parameter optimisation.

6.2.3 A 2D, six-parameter LSD with C. Vulgaris

The six parameter LSD has a curved top surface, with the extra two parameters being the top surface curvature K_{inner} and the height of the starting point of the top surface, as expressed by the inner height ratio r_{inner}, as explained in subsection 6.1.3. The parameter limits are defined in Table 6.4.

The results are shown below. The optimal design parameters for planar and diffuse light are very different as shown in Table 6.5, and pictorially in Figure 6.14. A more complex model gives rise to much improved, but still not zero, χ^2_{RMS} values of $\chi^2_{RMS} = 1.57$ and $\chi^2_{RMS} = 1.99$, with a decrease of 25.2% and 33.2% for planar and diffuse optimised designs respectively. The amount of incident light absorbed

in the algae rises slightly by 1.1% for the planar design, but more significantly by 7.5% for the diffuse design.

Beyond pure optics and the scope of this chapter, a further benefit of the 6 parameter planar design is a decrease in the total volume of the funnel, which would provide a decrease in material, and therefore cost, for production.

	Minimum	Maximum
Base radius	0	0.1
Top radius	0.1	0.45
Outer height ratio	0	1
Inner height ratio	0	1
Inner curvature	0.001	10
Outer curvature	0.001	10

Table 6.4: Physical parameter limits for the six parameters of the LSD

	Planar	Diffuse
Base radius	0.070	0.097
Top radius	0.243	0.254
Outer height ratio	0.006	0.029
Inner height ratio	0.189	0.547
Inner curvature	2.910	0.136
Outer curvature	2.792	2.80
χ^2_{RMS}	1.57	1.99
Total light absorbed	72.3 %	64.1 %

Table 6.5: Optimal parameter limits for a six parameters LSD, and their respective χ^2_{RMS} and total light absorbed by the algae

6.2.3.1 Switching light sources on the optimal designs

The performance of the LSD optimised for planar light is tested with diffuse light, and the one optimised for diffuse light is tested with planar light. χ^2_{RMS} values are higher, however the planar structure is less detrimental than the diffuse structure when illuminated with its non-optimal light source.

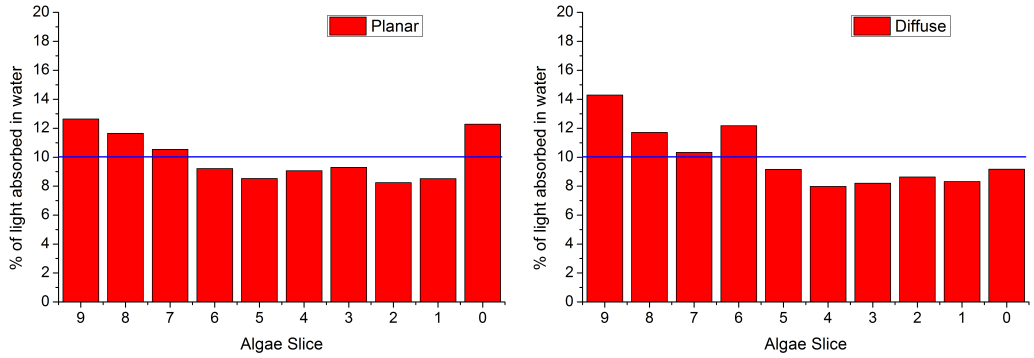

(a) Planar (b) Diffuse

Figure 6.13: Absorption profile of algae for planar and diffuse (isotropic) light conditions for a 6 parameter LSD. The blue line indicates the optimal absorption profile.

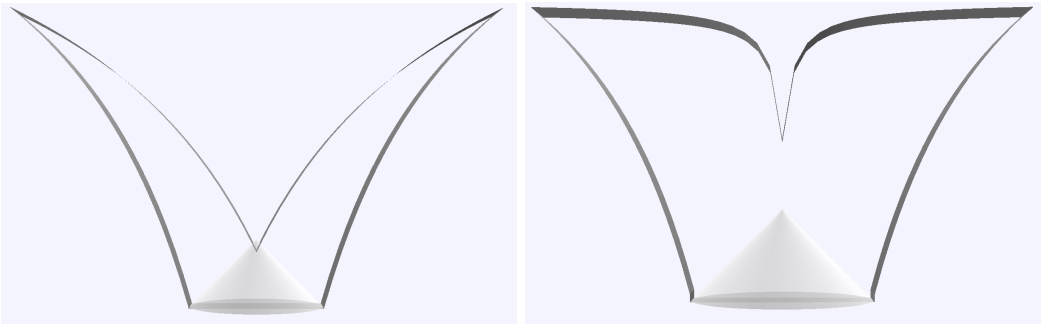

(a) Planar light (b) Diffuse light

Figure 6.14: Visualisations of the 6 parameter LSD after 20 generations of parameter optimisation for planar light (a) and diffuse light (b)

An interesting observation however is that the total light absorbed in the algae is higher for both designs with non-optimal incident light. The light absorbed using the planar structure is 72.3% with planar light and 73.3% for the diffuse light, and the light absorbed using the diffuse structure is 64.1% for the diffuse light and 66.8% for the planar light. This can be explained by a couple of layers absorbing significant amounts of light, namely the top two layers in the planar structure (Figure 6.15a) and the bottom two layers in the diffuse structure (Figure 6.15b). In this case however, having a higher percentage of light absorption does not mean a better performing LSD, as the quantity of light entering these high absorption is much above that of the saturation intensity for photosynthesis. This would mean

this light will be wasted through luminescence or heat dissipation.

	Planar structure, diffuse light	Diffuse structure, planar light
χ^2_{RMS}	4.03	4.70
Total light absorbed	73.3 %	66.8 %

Table 6.6: χ^2_{RMS} and total light absorbed for a six parameters LSD, with the opposite light source to which it was optimsed for

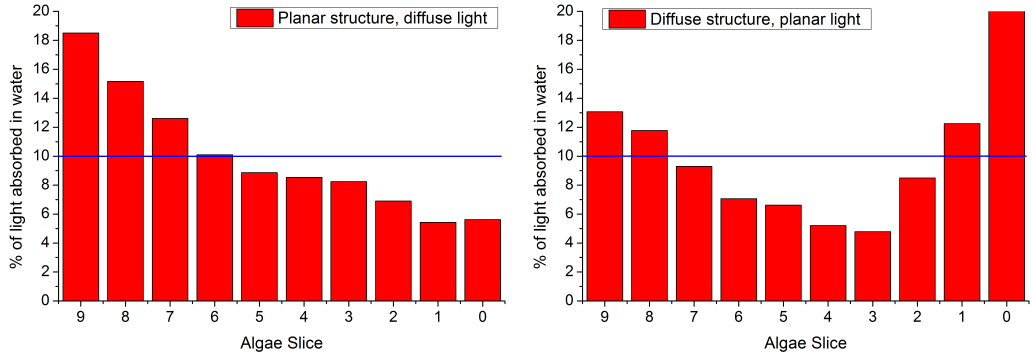

(a) Diffuse on planar structure

(b) Planar on diffuse structure

Figure 6.15: Absorption profile of algae using a 6 parameter LSD, where the opposed light source type is used on the design, with diffuse light used on the planar-optimised design (a) and planar light used on the diffuse-optimised design (b). The blue line indicates the optimal absorption profile.

6.3 Ascertaining growth rate increase due to the LSD

The main objective of this chapter was to determine the capacity for optimisation of the LSD to a figure of merit $\chi^2_{RMS} = 0$ by using a genetic algorithm. This is to ensure that each layer of algae in a pond does not receive more than the necessary quantity of light (400-600 μmolm^{-2}s^{-1}). The LSD was optimised for both planar and diffuse illumination conditions. In reality, the light incident on the raceway pond is a mix of the two components. In ASTM G-173 conditions, the ratio of direct:diffuse light intensity is 9:1. As such the LSD will be receiving a mixture of the two components.

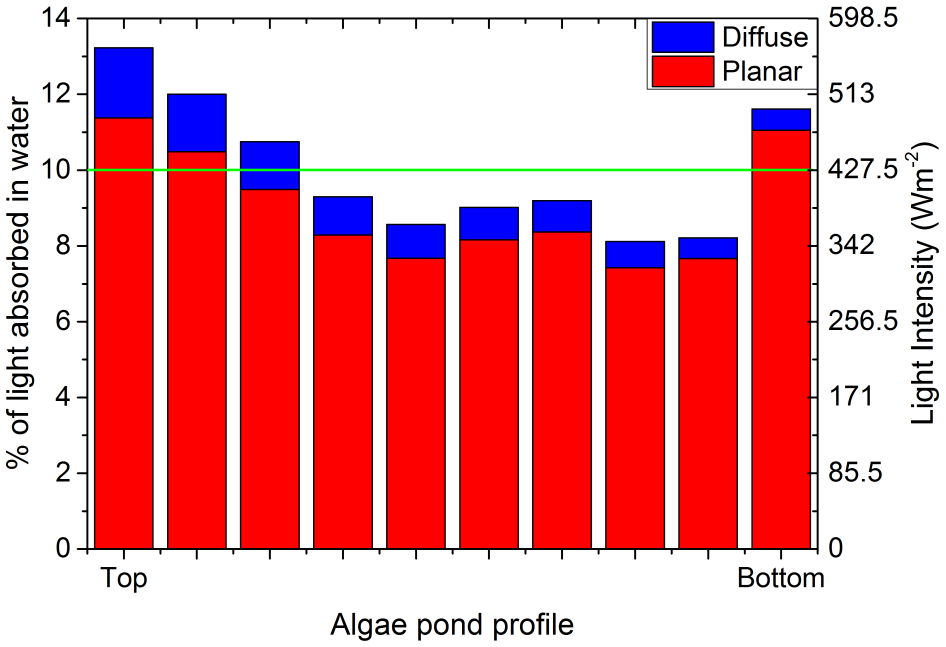

Figure 6.16: Absorption profile of algae using a 6 parameter LSD, factoring in the ratio of direct:diffuse light incident on the LSD. The green line indicates the optimal absorption profile.

When taking into account the 9:1 ratio of intensities between the incident light components, the absorption profile through the pond depth becomes less uniform due to the diffuse component being absorbed a lot more in the upper region of the pond. This is reflected by a higher χ^2_{RMS} value of $\chi^2_{RMS} = 1.69$. The merged absorption profile of light as a function of pond depth is shown in Fig. Figure 6.16.

There are two benefits of having a LSD, namely providing an increase in surface area for a given volume of algae culture and providing a more suitable illumination intensity. With the planar-optimised LSD from above, in a cylindrically symmetric 3D form, the surface area of the algae if were to not have an LSD is 0.186m^2. The LSD funnel surface area is 0.311m^2, giving a surface area increase of 67.5%.

In order to calculate the predicted increase in growth rate (μ) due to the use of the LSD, data is needed on the specific growth rate of *C. Vulgaris* as a function of incident light intensity. Data from Dauta *et al.* of *C. Vulgaris* at 30°C [140] is

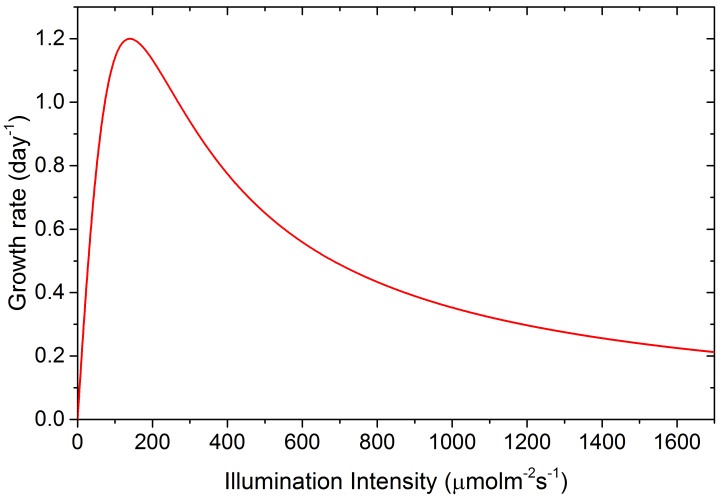

Figure 6.17: Growth rate as a function of illumination intensity, using a model taken from Peeters & Eilers (1978) [252].

used. Also used is their adjusted model from Peeters & Eilers (1978) [252]:

$$\mu = \mu max_T \cdot 2 \cdot (1 + \beta) \cdot I_r / (I_r^2 + 2 \cdot \beta \cdot I_r + 1) \tag{6.4}$$

where μmax_T is the maximum growth rate at a given temperature T, β is a fitting variable and $I_r = I/I_{opt}$ is the ratio between the incident intensity I and the optimal incident intensity I_{opt}. μmax_T is set at 1.3 day^{-1}, I_{opt} at 140 μmolm^{-2}s^{-1} and the fitting variable β at 0.1. This is shown graphically in Figure 6.17. The data and model parameters agree with more recent observational data of *C. Vulgaris* growth [253, 254, 255].

Of the incident photons on the LSD, 83.5% are transferred into the algae. The illumination intensity on the algae I_{algae} through a perfect LSD is therefore:

$$I_{algae} = 0.835 \cdot I_{inc} \cdot (A_{top}/A_{LSD}) \tag{6.5}$$

where I_{inc} is the incident intensity on the LSD top surface, A_{top} is the area of the pond surface which the LSD takes up and A_{LSD} is the surface area of the sides of the LSD in contact with the algae culture. As seen in Figure 6.16, the real LSD

Full solar spectrum intensity (Wm^{-2})	1000	600	300
Incident intensity ($\mu molm^{-2}s^{-1}$)	1678	1007	503
Perfect LSD intensity ($\mu molm^{-2}s^{-1}$)	837.87	502.82	251.16

Table 6.7: Incident intensity on the LSD and incident intensity on the algae with a perfect LSD of $\chi^2_{RMS} = 0$

illumination profile is not exactly perfect. Each "slice" then has its illumination corrected for the values shown in the figure:

$$I_{slice} = I_{algae} \cdot (L_{slice}/L_{opt}) \tag{6.6}$$

where L_{slice} is the percentage of light absorbed by the algae as determined by the raytrace model, shown in Figure 6.16, and L_{opt} is the percentage of light absorbed if the LSD was perfect. In this case, ten slices are used therefore $L_{opt} = 10\%$.

Three incident light intensities are used: 1, 0.6 and 0.3 suns (1000, 600, 300 Wm^{-2}). Table 6.7 shows the incident PAR intensity and the perfect intensity as determined by Equation 6.5.

The light intensity distribution across the depth of the pond with the LSD, as determined by Equation 6.6, is shown for three incident light intensities in Figure 6.18. For each illumination intensity point on the LSD, as shown in Figure 6.19, a Beer-Lambert penetration profile is calculated, and the Peeters & Eilers model (Equation 6.4), is applied through the penetration profile to obtain a growth rate profile of the algae as a function of penetration depth into the algae culture. This is shown in Figure 6.20. Each of these graphs is integrated as a function of penetration depth, and multiplied by the surface area of each LSD slice to obtain the integrated growth rate for the volume of algae. The integrated values for the growth rate increase in the raceway pond is given in Table 6.8.

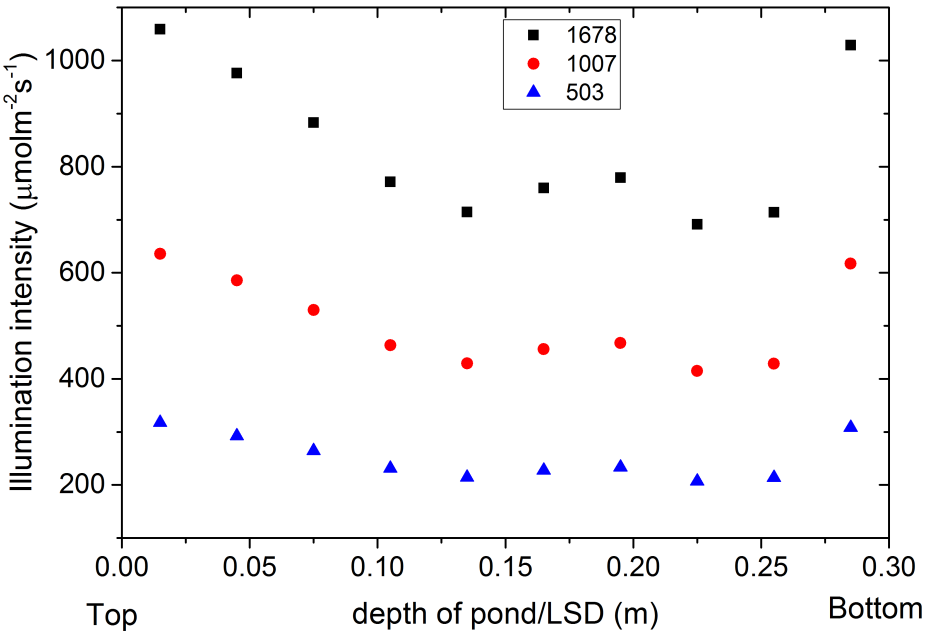

Figure 6.18: The light power density across the depth of the pond at each algae slice. This is done for 1, 0.6 and 0.3 suns (1678, 1007 and 503 $\mu molm^{-2}s^{-1}$)

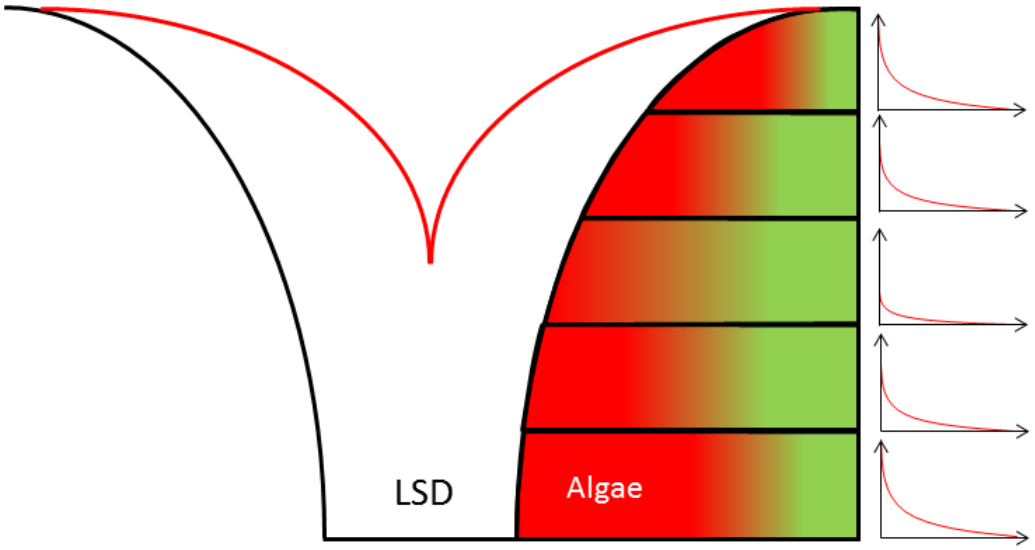

Figure 6.19: Each illumination value above in Figure 6.18 is the peak light intensity at the wall of the LSD. A Lambertian absorption profile is assumed horizontally through the algae slices. This means the total integrated amount of light absorbed is different with each slice.

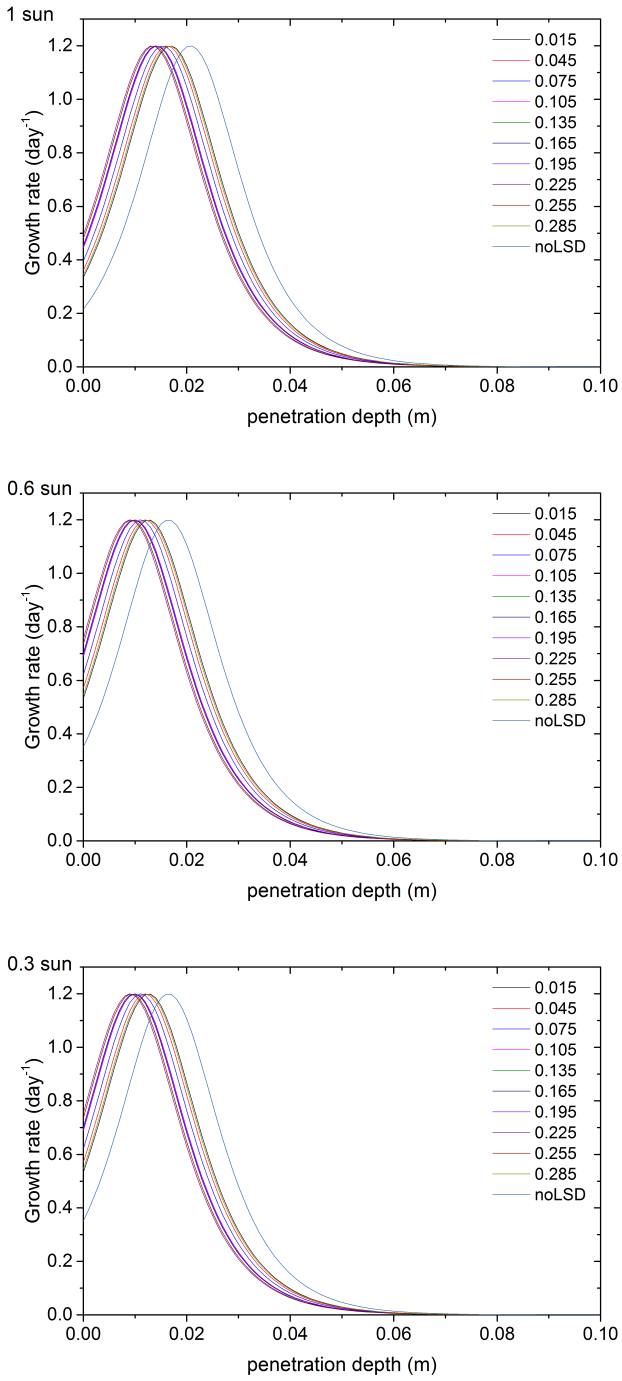

Figure 6.20: The growth rate of algae as a function of penetration depth for each LSD slice, corresponding to the relevant algae slice referencing in Figure 6.16. Incident intensities are 1 sun (top), 0.6 suns (middle) and 0.3 suns (bottom). The profile is also shown for the algae if there was no LSD. The growth rate as a function of penetration depth matches well with a similar graph in Figure 3 of Ritchie *et al.* (2012) of net photosynthesis as a function of penetration depth into a raceway pond [254].

Incident light intensity	Algae growth increase
1 sun	57.0 %
0.6 sun	50.2 %
0.3 sun	35.2 %

Table 6.8: Increase in growth rate of algae when using a LSD

The growth rate of algae in a raceway pond is increased by using a LSD even in low incident light conditions by at least 35%, and at 1 sun light conditions the growth rate of algae is improved by 57%. The LSD in this chapter has been optimised for incident light at normal incidence to the the raceway pond. In order to optimise the LSD for best average performance over the course of a day, optimisation simulations must be run over a number of incident angles. The importance of each angle of incidence can be weighted by the likelihood of it being the sun's zenithal angle over the course of a day or year, given the global location of the raceway pond.

A secondary byproduct of more optimal light intensities into the algae and their more efficient use of it is a decrease in heat dissipation. This leads to less evaporative loss in a raceway pond, a small but not insignificant ($\sim$ 1.5%) amount of operating costs in an algae farm [131]. Furthermore, the LSD would take up space in the pond, displacing some volume of algae mixture. The illuminated surface area:volume ratio for algae is improved. This removes "dead volume" within the raceway pond where it is too dark for algae to photosynthesize and grow.

The added capital cost of buying the LSD, as well as the added operating cost of cleaning, cannot be overlooked. Plastic pond lining alone can constitute around 25% of the total capital cost of an algae farm [131]. It would not be unreasonable to think that filling raceway ponds with bespoke PMMA-based LSDs would at the very least match the cost of pond lining. Reliable cost analysis to determine whether the LSD is an economically viable concept cannot be made without first knowing practically by how much the LSD would increase algae yield.

6.4 Conclusion

Algae raceway ponds are the cheapest method of large scale algae farming for biofuel production, yet there is a lack of investigation interest into innovative optics for intrinsic loss mechanisms. The fact that algae has an absorption coefficient of the order of 100m^{-1} means that of the 30cm depth of pond, only the top few centimetres are actually effective in algae growth. This algae over-absorbs incident light and energy is lost both through radiative (optical and thermal) dissipation and through active inhibition of algae survival and growth. This chapter introduced a novel optical device in the form of a retrofitting luminescent solar diffuser (LSD). The device, a form of optical funnel, spectrally converts incident light into a more desirable wavelength and distributes it uniformly across the depth of a pond, both increasing the illumination surface area:volume of the algae and minimising energy losses due to over-absorption.

Using a root-mean-square comparison of a perfect illumination distribution across a pond depth as a figure of merit, a 2D raytrace model in pvtrace was used in conjunction with a genetic algorithm to optimise design parameters of a LSD designed to be retrofitted into a 30cm deep raceway pond using *C. Vulgaris* as the algae species. Whilst less light is absorbed in total (90% without the LSD, 64.1 - 72.3% with the LSD), the light incident on the algae with the LSD is at a lower light intensity closer to that for optimal growth rates. Using the optimised illumination profile across the LSD depth literature data on growth rates of algae as a function of illumination intensity, it is calculated that by using a LSD one can obtain an increase in growth rate for algae of 57% at 1 sun, 50.2% at 0.6 sun and 35.2% and 0.3 sun intensities.

Improved light distribution and more optimal incident light illumination, spectral conversion of incident light and higher surface area:volume ratios are the main benefits of the LSD. Secondary effects caused by these benefits would be less evap-

orative loss in a raceway pond due to less heat dissipation losses in the algae and less optically dark “dead zones” within a raceway pond.

Chapter 7

Conclusions

This thesis aimed to contribute to the fields of luminescent solar concentrators (LSCs), photoelectrochemical (PEC) water splitting and algae farming for biofuels. The thesis addressed optical phenomena related to the geometry of cylinders, a waveguiding solution to illuminate a two-sided PEC reactor and an optical method to mitigate the loss mechanisms of photosynthesis in algae.

7.1 Thesis Achievements

7.1.1 Pvtrace

The raytrace model pvtrace was upgraded to be parallelisable using the ParallelPython module. Simple as well as truncated cones were added as shape geometries. 3D mesh generation capability was also added as a separate module which utilises the "Polygon" shape class. Different light sources were added to pvtrace: a planar light source which uses the Sun's zenithal and azimuthal values as input variables, and a hemispherical light source was added to simulate diffuse light conditions.

7.1.2 Cylindrical array LSCs

First, a practical demonstration showed that photon concentration of fibre LSCs increases linearly with fibre length up to 2m. This is due to losses from re-absorption and re-emission occurring mostly in the first 5cm of the fibre, shown by the red-shifting of the edge emission.

Using pvtrace for 2D raytrace modelling, it was found that light trapping of incident light occurs in a circular array from an angle of incidence of 60°. This light trapping effect then starts to decrease at 70°. A hypothesis was put forward that the optical efficiency of a cylindrical LSC array would increase at solar angles of incidence between 60° and 70°.

A north-south aligned cylindrical LSC array was simulated in clear sky light conditions in London, UK for four separate days. The cylindrical LSC array experiences an efficiency boost for the times of the day where the Sun's incident zenithal angle is within the light trapping range of 60° - 70°, an effect not seen in planar geometry LSCs with identical simulation conditions. At peak light trapping, that cylindrical LSC efficiencies reach a value 5%-10.7% higher than that of planar LSCs. This efficiency boost could be seen as a practical way to improve a LSC array in the field; Effective alignment of the array could provide an efficiency boost at desired time or seasonal periods.

7.1.3 Concentrating waveguide optics for a water splitting reactor

A novel method to illuminate a double-illuminated PEC reactor was introduced. A reflective cone is embedded inside a waveguide, where it reflects incident light concentrated by a Fresnel lens into the waveguide, and therefore in the PEC reactor. Pvtrace simulations show that with reflective material on three out of the four waveguide edges, the optical efficiency of the cone in a waveguide can be 49.6%. Having reflective material on the waveguide edges also homogenises the illumination

profile across the edge.

Practical flash lamp high concentration illumination experiments with a drilled cone in a PMMA waveguide gave an optical efficiency between 1.15% and 3%. This was due to cone surface roughness due to drilling striations, scattering much of the incident light.

A full demonstration PEC reactor with a reflective cone / Fresnel lens optical system was tested outdoors. Measuring the illumination profile across the waveguide edge confirms that the cone acts Lambertian rather than specular. The middle of the waveguide edge produced 1.5x and 2.5x concentration without and with edge reflectors respectively. Using a specular cone and better edge reflectors could improve the concentration by a factor of 4.

A quantum well solar cell (QWSC) was used as a luminescent centre, to replace the reflective cone in a waveguide. Measuring the photoluminescence (PL) out of the edge of a sample showed that the waveguiding efficiency of a QWSC is four orders of magnitude less than the needed value to validate the concept of using the PL of a QWSC for secondary optical processes.

7.1.4 The luminescent solar diffuser

A luminescent solar diffuser (LSD) is an optical funnel that can be retrofitted into an algae raceway pond in order to homogenise the illumination profile of incident light through the depth of the pond. This is beneficial as on the top surface the algae receive too much light, which is detrimental to its growth rate. The high optical density of algae also means most of the pond volume is dark, meaning the algae do not grow.

A pvtrace 2D model of the LSD was merged with a genetic algorithm to prove that the LSD is optimisable within the pond constraints. By using a LSD one can

obtain an increase in growth rate for algae of 57% at 1 sun, 50.2% at 0.6 sun and 35.2% and 0.3 sun intensities, with values calculated by using literature data on algae growth rates as a function of illumination intensity.

The main benefits of the LSD are improved light distribution, more optimal incident light illumination, spectral conversion of incident light to more favourable wavelengths and higher surface area:volume ratios in a raceway pond. Secondary effects caused by these benefits are less evaporative loss in a raceway pond due to less heat dissipation losses in the algae and less optically dark "dead zones" within a raceway pond.

The LSD increases algae yield as a way to improve economic viability in algae raceway ponds, already the cheapest method of large scale algae farming for biofuel production.

7.2 Further work

A significant amount of the achievements of the thesis have been through ray-trace modelling. As such, most of the next steps for the pieces of work is to determine whether experiments agree with the modelling.

7.2.1 Cylindrical LSCs

A practical demonstration of the efficiency boost in cylindrical LSC arrays due to light trapping can be shown to complement the results obtained from the pvtrace simulation. This would require buildling a module-sized cylindrical LSC (CLSC) array. Multiple arrays could be oriented North-South and East-West. The tilt of the module can be investigated along these two cardinal orientations. The two objectives of this work would be to a) confirm the efficiency boost when the sun is at the light trapping angle-of-incidence, and b) to practically quantify this efficiency boost. The setup would be similar to that of the sound barriers constructed by

Kanellis *et al.* [256].

A further research topic would be to quantify the efficiency boost for CLSCs with different luminophores. It was hypothesised that the efficienct boost would be more significant with aligned luminophores that luminescence with an anisotropy favourable to waveguiding.

7.2.2 Waveguiding optics for water splitting

For the fully functioning PEC reactor, the final measurement needed for publication is direct collection of hydrogen to determine the solar-to-hydrogen (STH) efficiency of the setup. Measuring the photocurrent gives an indication for STH efficiencies [77] and is suitable for conferences, but is unsatisfactory for publication.

The embedded cone in a waveguide manufacturing can be improved. Polishing can be done on the cone surface, and reflective material can be coated on or placed on the cone surfaces. Reflectors with a higher reflectivity can be used on the waveguide edges. These improvements can improve the amount of light coming out of the waveguide edge by a factor of 4.

Neverthless, the ideal distribution of light on a photo-electrode is uniform. Therefore whilst the cone/Fresnel lens configuration can be improved on, the next step should be to utilise a linear Fresnel lens and a reflective wedge. This is demonstrated in Figure 5.7. A further benefit of using a wedge / linear Fresnel lens include the need to only have single-axis tracking, rather than dual-axis tracking for the cone / Fresnel lens setup. This would make a larger scale up cheaper and easier to manufacture.

Raytrace modelling should be performed to determine the optimal angle of the reflective wedge. Light from the edges of the Fresnel lens will be impinging on

the wedge at an acute angle, and so would be reflected into the waveguide an an angle inside the escape cone. Placing reflectors on the top and bottom of the waveguide would help direct this light towards the PEC reactor windows.Raytrace modelling can be performed on placing reflectors on the top and bottom surfaces of the waveguide to determine the efficacy of this idea (Figure 7.1).

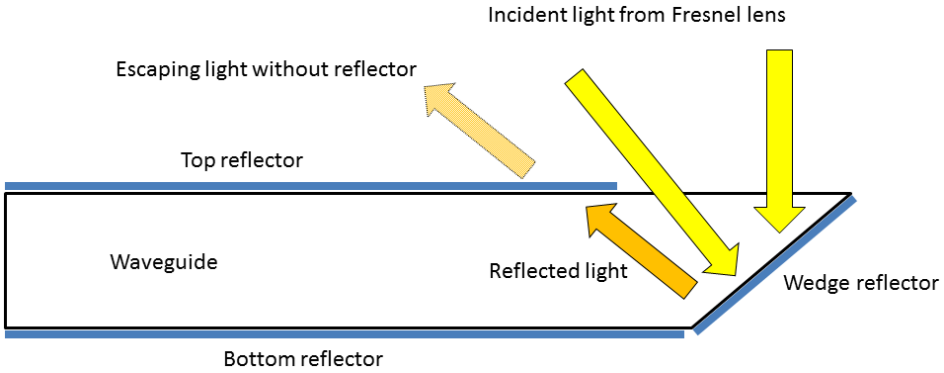

Figure 7.1: Having reflectors on the top and bottom of the waveguide might help contain escaping light.

Linear Fresnel lenses and new waveguides have been purchased and are in the possession of Dr. Anna Hankin. The waveguides are awaiting final design confirmation before wedges are cut into them.

Further to the optics, the triple-junction photo-cathode can be optimised. The current device is a standard high efficiency solar cell, optimised for conventional concentrator PV operation with an AM1.5 spectrum. It also has tall (micron height) gold contacts, which mean the evaporated layer of titanium dioxide (TiO_2) is highly non-uniform. This introduces many locations for which the electrolyte to attack and dissolve the underlying device material.

The light impinging on the device in the reactor has a different spectrum due to light interacting with reflectors, passing through a PMMA waveguide, which has its own absorption spectrum, and through the electrolyte. Due to Kirchoff's law of current being the same throughout the whole circuit, the top junction is

current limiting the whole device as the PMMA, electrolyte and TiO_2 layer absorb a significant amount of light in the UV/blue region. Therefore there is an opportunity to design the device's three junctions in order to not have any junction current limiting the others.

7.2.3 Luminescent Solar Diffuser

A practical demonstration of a LSD can be built and tested in an algae raceway pond to confirm this thesis's claim that the growth rate of algae can increase by 35.2 - 57%. This will require collaboration with a research group or company with access to experimental sized raceway ponds.

Preliminary investigation into plastics manufacturing has determined that either extrusion or machining a LSD from a solid block of PMMA is the most practical and fastest way to manufacture small numbers of LSDs to place into a small raceway pond. Extrusion means the LSD will be of a linear configuration (see Figure 6.2). Further 3D raytrace modelling should be undertaken to determine how the figure of merit differs from a circular configuration LSD.

Once the LSD has been practically proven to improve algae growth rates, further 3D raytrace models should be built to optimise LSDs for a certain location in the world. The distribution of light across the pond depth will change as the sun moves across the sky, and so the LSD performance should be analysed for all angles of incidence.

The current version of pvtrace is not up to task for extended 3D simulations. The core intersection algorithm for a polygon mesh should be changed to make it operate faster. Because computer graphics cards are highly optimised for parallel tasks, they would complete raytrace simulations much faster than a computer's CPU. The algorithm should be modified so that it can be run through a computer's

graphics card (the calculation functions need to be made basic enough to be communicated to the graphics card via CUDA [257] or PyCUDA [258]). Conversely, a different raytrace software should be used if the task proves too difficult.

There are practical aspects to investigate with the LSD. The best performing LSD design currently has a highly curved top surface. This might prove difficult to clean, and so there should be an investigation on the cost trade-off between increased algae yield and higher maintenance due to cleaning.

Appendix A

Matlab fitting of cone in a waveguide emission profiles

A.1 Specular Cone and reflectors on waveguide edges

General model Sin2:

$f(x) = a1 * sin(b1 * x + c1) + a2 * sin(b2 * x + c2)$

Coefficients (with 95% confidence bounds):

a1 = 2.858 (-228.8, 234.5)

b1 = 19.43 (-137.3, 176.1)

c1 = 1.58 (1.47, 1.689)

a2 = 1.918 (-229.8, 233.6)

b2 = 23.08 (-187.6, 233.8)

c2 = -1.56 (-1.712, -1.408)

Goodness of fit:

SSE: 0.04347

R-square: 0.9724

Adjusted R-square: 0.9684

RMSE: 0.03575

A.2 Lambertian Cone and reflectors on waveguide edges

General model Gauss1:

$f(x) = a1 * exp(-((x - b1)/c1)^2)$

Coefficients (with 95% confidence bounds):

a1 = 0.9507 (0.9332, 0.9682)

b1 = 0 (fixed at bound)

c1 = 0.09395 (0.09124, 0.09666)

Goodness of fit:

SSE: 0.03808

R-square: 0.978

Adjusted R-square: 0.9775

RMSE: 0.03166

Appendix B

Irradiance spectra for a cone in a waveguide

B.1 Spectral irradiance of a reflective cone in a waveguide for 5 concentrations as stated in Table 3.2

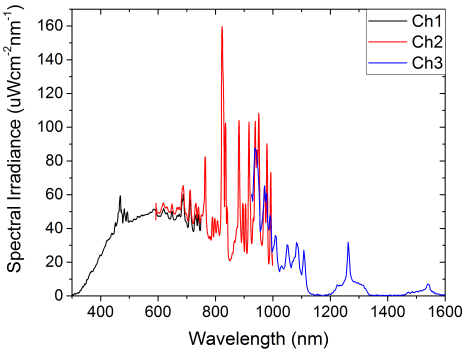

(a) P5

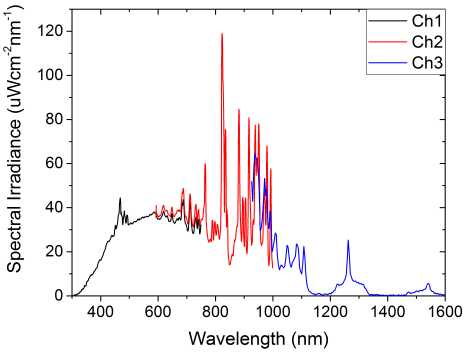

(b) P4

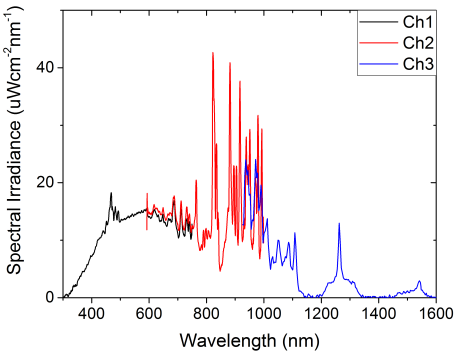

(c) P3

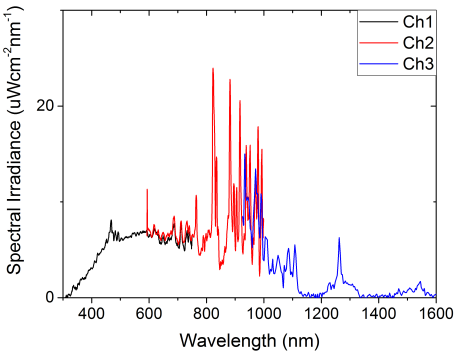

(d) P2

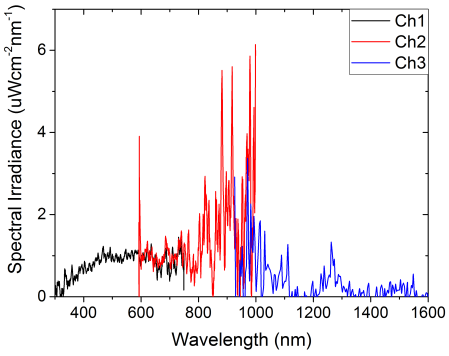

(e) P1

B.2 Spectral irradiance of a reflective cone in a waveguide with reflectors on 3 of its edges, for 5 concentrations as stated in Table 3.2

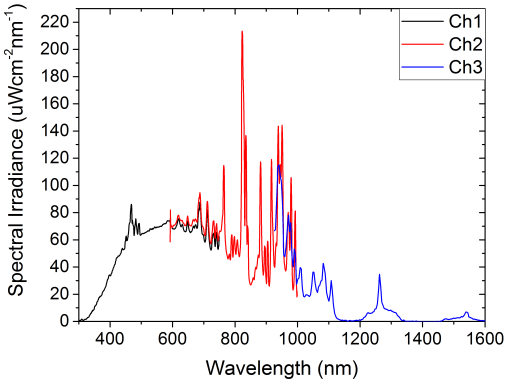

(a) P5

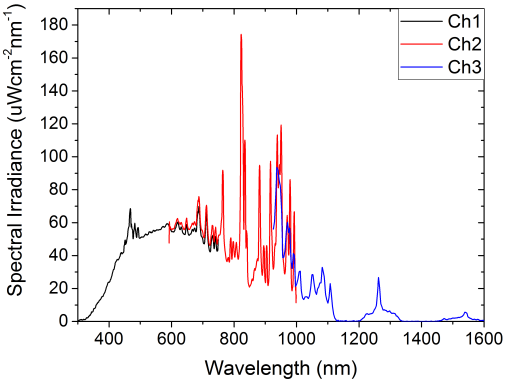

(b) P4

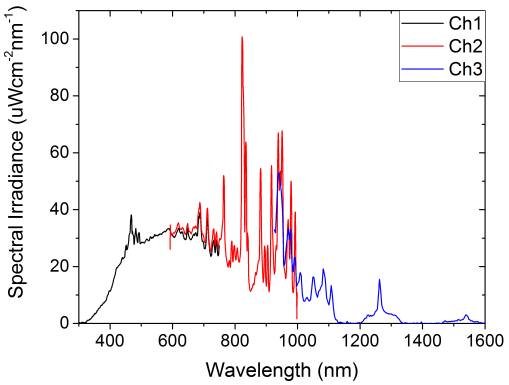

(c) P3

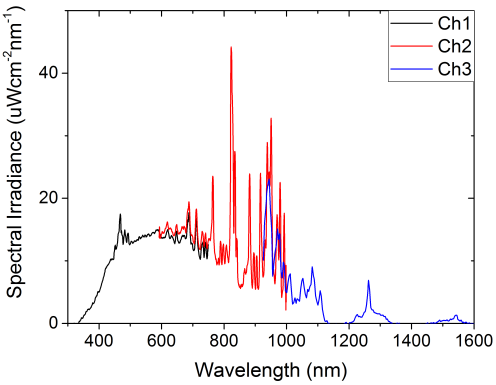

(d) P2

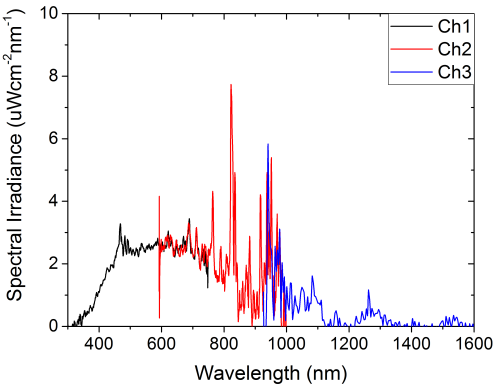

(e) P1

Appendix C

Irradiance spectra for a quantum well solar cell in a waveguide

C.1 Isolated spectral irradiance of QT1604 in a waveguide for 5 concentrations as stated in Table 3.2

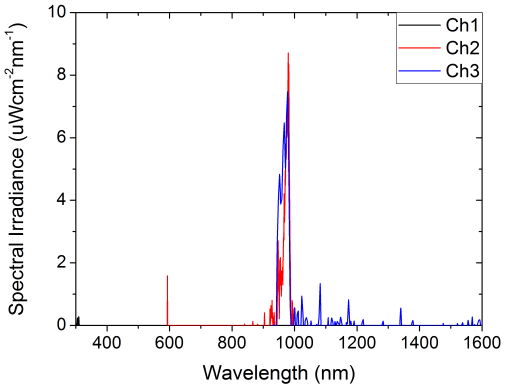

(a) P5

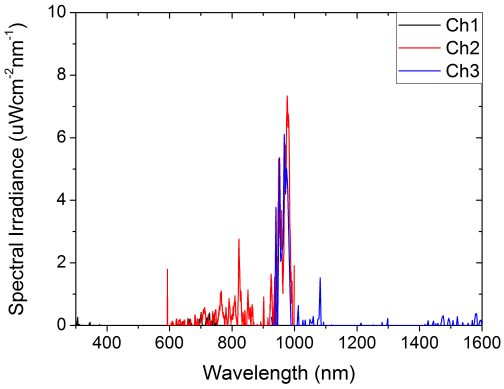

(b) P4

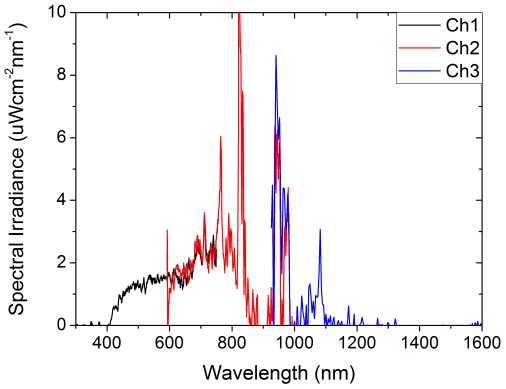

(c) P3

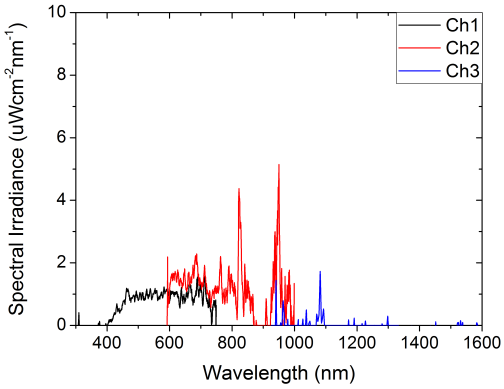

(d) P2

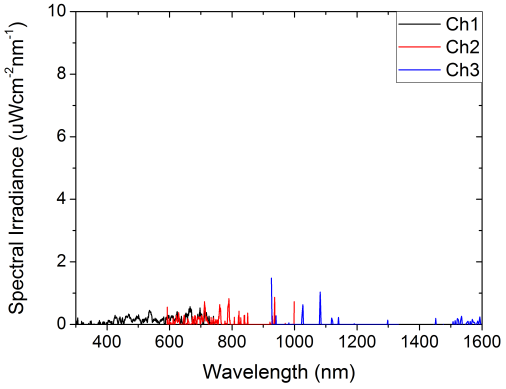

(e) P1

Appendix D

Quantum Well Solar Cell Structure

Table D.1: Structure of Photoluminescence sample QT1604

Layer	Repeats	Material	Thickness (Å)	Dopant Type	Dopant	Dopant conc. (cm^{-3})
Cap	1	GaAs	2200	p	Zn	$3x10^{19}$
Window	1	$Al_{0.8}GaAs$	450	p	C	$2x10^{18}$
i-region	1	GaAs	100			
$\frac{1}{2}$ barrier	22	$GaAsP_{0.06}$	210			
QW		$In_{0.17}GaAs$	80			
$\frac{1}{2}$ barrier		$GaAsP_{0.06}$	210			
i-region	1	GaAs	100			
Base	1	GaAs	20000	n	Si	$1.4x10^{17}$
Buffer	1	GaAs	3000	n	Si	$1.5x10^{18}$

Appendix E

Publications

E.1 First Author Publications

Videira J.J.H, Bilotti E., Chatten A.J., "*Cylindrical array luminescent solar concentrators: Performance boosts by geometric effects*", Optics Express 24 (14), A1188-A1200 (2016), DOI:10.1364/OE.24.0A1188

E.2 Conferences

Videira JJH, Bilotti E, Chatten AJ, "*Cylindrical and square fibre luminescent solar concentrators: Experimental and Simulation comparisons*", IEEE 40th Photovoltaic Specialist Conference (PVSC), Denver, USA (2014), p. 2280-2285, DOI:10.1109/PVSC.2014.6925381

Videira JJH, Bilotti E, Chatten AJ, "*Cylindrical and square fibre luminescent solar concentrators compared*", Proc. of the 6th World Conference on Photovoltaic Energy Conversion (WCPEC), Kyoto, Japan (2014).

Videra JJH, Barnham KWJ, Hankin A, Connolly JP, Leak M, Johnson J, Kelsall GH, Kennedy K, Roberts JS, Cowan AJ, Chatten AJ, "*Introducing novel light management to design a hybrid high concentration photovoltaic/water splitting sys-*

tem", IEEE 42nd Photovoltaic Specialist Conference (PVSC), New Orleans, USA (2015), p. 1-6, DOI: 10.1109/PVSC.2015.7356182

Videra JJH, Barnham KWJ, Hankin A, Connolly JP, Leak M, Johnson J, Kelsall GH, Kennedy K, Roberts JS, Cowan AJ, Chatten AJ, "*Introducing novel light management to design a hybrid high concentration photovoltaic/water splitting system*", Early Career Researchers' Symposium: "Solar Fuels: moving from materials to devices", London, UK (2015).

Hankin A, Videira JJH, Bedoya-Lora F, Barnham KWJ, Ekins-Daukes N, Kelsall GH, "*Design and development of photo-electrochemical reactors for hydrogen production with solar energy*", Advances in Semiconductors and Catalysts for Photoelectrochemical Fuel Production (SolarFuel16), Berlin, Germany (2016).

Appendix F

Permissions

Title: Solar energy conversion efficiencies in photosynthesis: Minimizing the chlorophyll antennae to maximize efficiency

Author: Anastasios Melis

Publication: Plant Science

Publisher: Elsevier

Date: October 2009

Order Completed

Thank you for your order.

This Agreement between Jose Videira ("You") and Elsevier ("Elsevier") consists of your license details and the terms and conditions provided by Elsevier and Copyright Clearance Center.

Your confirmation email will contain your order number for future reference.

Get the printable license.

License Number	3901570987978
License date	Jul 03, 2016
Licensed Content Publisher	Elsevier
Licensed Content Publication	Plant Science
Licensed Content Title	Solar energy conversion efficiencies in photosynthesis: Minimizing the chlorophyll antennae to maximize efficiency
Licensed Content Author	Anastasios Melis
Licensed Content Date	October 2009
Licensed Content Volume	177
Licensed Content Issue	4
Licensed Content Pages	9
Type of Use	reuse in a thesis/dissertation
Portion	figures/tables/illustrations
Number of figures/tables/illustrations	2
Format	both print and electronic
Are you the author of this Elsevier article?	No
Will you be translating?	No
Order reference number	
Original figure numbers	Figures 1, 2
Title of your thesis/dissertation	Novel applications of luminescence for solar energy
Expected completion date	Aug 2016
Estimated size (number of pages)	200
Elsevier VAT number	GB 494 6272 12
Requestor Location	Jose Videira 11 Belgrave Square London, other SW1X 8PP United Kingdom Attn: Jose Videira
Total	0.00 GBP

ORDER MORE CLOSE WINDOW

Bibliography

[1] US EIA. "Annual energy review 2011". In: *Energy Information Administration* (2012).

[2] IPCC Working Group I. *Fifth Assessment Report, Climate Change 2013: The Physical Science Basis, A Summary for Policymakers*. Intergovernmental Panel on Climate Change, 2013.

[3] Edward Wong. *Cost of Environmental Damage in China Growing Rapidly Amid Industrialization*. URL: http://www.nytimes.com/2013/03/30/world/asia/cost-of-environmental-degradation-in-china-is-growing.html.

[4] Mark A Delucchi and Mark Z Jacobson. "Providing all global energy with wind, water, and solar power, Part II: Reliability, system and transmission costs, and policies". In: *Energy policy* 39.3 (2011), pp. 1170–1190.

[5] *2030 climate and energy goals for a competitive, secure and low-carbon EU economy*. URL: http://europa.eu/rapid/press-release_IP-14-54_en.htm.

[6] *Directive 2010/31/EU of the European Parliament and of the Council on the energy performance of buildings*. Tech. rep. European Union, 2010.

[7] *'Historic day' as 175 countries sign Paris Climate Agreement*. URL: http://www.climateactionprogramme.org/news/historic_day_as_175_countries_sign_paris_climate_agreement.

[8] C.A. Gueymard, D. Myers, and K. Emery. "Proposed reference irradiance spectra for solar energy systems testing". In: *Solar energy* 73.6 (2002), pp. 443–467.

[9] PVPS Photovoltaic Power Systems Programme. *2015 - Snapshot of Global PV Markets*. Tech. rep. Report IEA PVPS T1-29:2016. IEA - International Energy Agency, 2016.

[10] *GTM Research: Global Solar PV Installations Grew 34% in 2015*. URL: http://www.greentechmedia.com/articles/read/gtm-research-global-solar-pv-installations-grew-34-in-2015.

[11] M Tripathy, PK Sadhu, and SK Panda. "A critical review on building integrated photovoltaic products and their applications". In: *Renewable and Sustainable Energy Reviews* 61 (2016), pp. 451–465.

[12] Bjørn Petter Jelle, Christer Breivik, and Hilde Drolsum Røkenes. "Building integrated photovoltaic products: A state-of-the-art review and future research opportunities". In: *Solar Energy Materials and Solar Cells* 100 (2012), pp. 69–96.

[13] Erin Baker et al. "The economics of solar electricity". In: *resource* 5 (2013).

[14] Rasmus Luthander et al. "Photovoltaic self-consumption in buildings: A review". In: *Applied Energy* 142 (2015), pp. 80–94.

[15] Shafiqur Rehman, Luai M Al-Hadhrami, and Md Mahbub Alam. "Pumped hydro energy storage system: a technological review". In: *Renewable and Sustainable Energy Reviews* 44 (2015), pp. 586–598.

[16] D Larcher and JM Tarascon. "Towards greener and more sustainable batteries for electrical energy storage". In: *Nature chemistry* 7.1 (2015), pp. 19–29.

[17] AM Foley et al. "A long-term analysis of pumped hydro storage to firm wind power". In: *Applied Energy* 137 (2015), pp. 638–648.

[18] AB Gallo et al. “Energy storage in the energy transition context: A technology review”. In: *Renewable and Sustainable Energy Reviews* 65 (2016), pp. 800–822.

[19] Markos Katsanevakis, Rodney A Stewart, and Junwei Lu. “Aggregated applications and benefits of energy storage systems with application-specific control methods: A review”. In: *Renewable and Sustainable Energy Reviews* (2016).

[20] Georg Fuchs et al. “Technology overview on electricity storage”. In: *ISEA, Aachen, Juni* (2012).

[21] Coalition of Organisations. *Commercialisation of Energy Storage in Europe*. Tech. rep. Fuel Cells and Hydrogen Joint Undertaking, 2015.

[22] Jaephil Cho, Sookyung Jeong, and Youngsik Kim. “Commercial and research battery technologies for electrical energy storage applications”. In: *Progress in Energy and Combustion Science* 48 (2015), pp. 84–101.

[23] O Teller et al. “Joint EASE EERA recommendations for a European energy storage technology development roadmap towards 2030”. In: *Brussels, Belgium: European Association for Storage of Energy (EASE) and European Energy Research Alliance (EERA)* (2013).

[24] Exxon Mobil. *World Jet Fuel Specifications, 2005 Edition*. Tech. rep. Exxon Mobil Aviation, 2005.

[25] Michael M Thackeray, Christopher Wolverton, and Eric D Isaacs. “Electrical energy storage for transportation—approaching the limits of, and going beyond, lithium-ion batteries”. In: *Energy & Environmental Science* 5.7 (2012), pp. 7854–7863.

[26] Michael G Walter et al. “Solar water splitting cells”. In: *Chemical reviews* 110.11 (2010), pp. 6446–6473.

[27] Allen J Bard et al. *Electrochemical methods: fundamentals and applications*. Vol. 2. Wiley New York, 1980.

[28] Michael Grätzel. "Photoelectrochemical cells". In: *Nature* 414.6861 (2001), pp. 338–344.

[29] Krishnan Rajeshwar. "Hydrogen generation from irradiated semiconductor-liquid interfaces". In: *Solar Hydrogen Generation*. Springer, 2008, pp. 167–228.

[30] Diana Moreira and Jose CM Pires. "Atmospheric CO2 capture by algae: negative carbon dioxide emission path". In: *Bioresource Technology* 215 (2016), pp. 371–379.

[31] Changhai Peng, Ying Huang, and Zhishen Wu. "Building-integrated photovoltaics (BIPV) in architectural design in China". In: *Energy and Buildings* 43.12 (2011), pp. 3592–3598.

[32] Solar Century. *Solar Century's c21e solar tiles*. URL: www.solarcentury.com/uk/c21e-tiles-and-slates/.

[33] Tesla. *Tesla Solar Roof*. URL: https://www.tesla.com/en_GB/solar.

[34] Danny HW Li, Liu Yang, and Joseph C Lam. "Zero energy buildings and sustainable development implications–A review". In: *Energy* 54 (2013), pp. 1–10.

[35] Marco Raugei and Paolo Frankl. "Life cycle impacts and costs of photovoltaic systems: current state of the art and future outlooks". In: *Energy* 34.3 (2009), pp. 392–399.

[36] Bjørn Petter Jelle et al. "Fenestration of today and tomorrow: A state-of-the-art review and future research opportunities". In: *Solar Energy Materials and Solar Cells* 96 (2012), pp. 1–28.

[37] Christopher JM Emmott et al. "Organic photovoltaic greenhouses: a unique application for semi-transparent PV?" In: *Energy & environmental science* 8.4 (2015), pp. 1317–1328.

[38] Brian Norton et al. "Enhancing the performance of building integrated photovoltaics". In: *Solar Energy* 85.8 (2011), pp. 1629–1664.

[39] Patrina Eiffert and International Energy Agency PVPS Task 7. *Guidelines for the economic evaluation of building-integrated photovoltaic power systems*. National Renewable Energy Laboratory, 2003.

[40] Marios D Chatzisideris et al. "Ecodesign perspectives of thin-film photovoltaic technologies: A review of life cycle assessment studies". In: *Solar Energy Materials and Solar Cells* (2016).

[41] P Bonomo et al. "BIPV: building envelope solutions in a multi-criteria approach. A method for assessing life-cycle costs in the early design phase". In: *Advances in Building Energy Research* (2016), pp. 1–26.

[42] Farshad Azadian and MAM Radzi. "A general approach toward building integrated photovoltaic systems and its implementation barriers: A review". In: *Renewable and Sustainable Energy Reviews* 22 (2013), pp. 527–538.

[43] Toby Couture and Yves Gagnon. "An analysis of feed-in tariff remuneration models: Implications for renewable energy investment". In: *Energy policy* 38.2 (2010), pp. 955–965.

[44] James Murray. *Solarcentury debuts 'great-looking' Sunstation solar system*. URL: http://www.businessgreen.com/bg/news/2457603/solarcentury-debuts-great-looking-sunstation-solar-system.

[45] *Musac Museum*. URL: https://pixabay.com/en/musac-museum-contemporary-art-leon-703016/.

[46] *Palais de Congres - Montreal*. URL: https://www.flickr.com/photos/manumilou/5674712062.

[47] OxfordPV. *OxfordPV*. URL: http://www.oxfordpv.com/.

[48] *EPFL's campus has the world's first solar window*. URL: https://actu.epfl.ch/news/epfl-s-campus-has-the-world-s-first-solar-window/.

[49] W. H. Weber and J. Lambe. "Luminescent greenhouse collector for solar radiation". In: *Appl. Opt.* 15.10 (1976), pp. 2299–2300.

[50] A. Goetzberger and W. Greubel. "Solar energy conversion with fluorescent collectors". In: *Applied physics* 14.2 (1977), pp. 123–139. ISSN: 0340-3793.

[51] J. A. Levitt and W. H. Weber. "Materials for luminescent greenhouse solar collectors". In: *Appl. Opt.* 16.10 (1977), pp. 2684–2689.

[52] A Goetzberger. "Fluorescent solar energy collectors: operating conditions with diffuse light". In: *Applied physics* 16.4 (1978), pp. 399–404.

[53] M.G. Debije and P.P.C. Verbunt. "Thirty Years of Luminescent Solar Concentrator Research: Solar Energy for the Built Environment". In: *Advanced Energy Materials* 2.1 (2012), pp. 12–35.

[54] Petr Klán and Jakob Wirz. *Photochemistry of organic compounds: From concepts to practice*. John Wiley & Sons, 2009.

[55] AM Hermann. "Luminescent solar concentrators—a review". In: *Solar Energy* 29.4 (1982), pp. 323–329.

[56] *An Annotated History Of Oil Prices Since 1861*. URL: http://uk.businessinsider.com/annotated-history-crude-oil-prices-since-1861-2014-12.

[57] N Aste et al. "Performance analysis of a large-area luminescent solar concentrator module". In: *Renewable Energy* 76 (2015), pp. 330–337.

[58] WGJHM van Sark. "Recent developments in luminescent solar concentrators". In: *SPIE Solar Energy+ Technology*. International Society for Optics and Photonics. 2014, pp. 917804–917804.

[59] Michael G Debije and Vikram A Rajkumar. "Direct versus indirect illumination of a prototype luminescent solar concentrator". In: *Solar Energy* 122 (2015), pp. 334–340.

[60] Finn M Vossen, Mariëlle PJ Aarts, and Michael G Debije. "Visual performance of red luminescent solar concentrating windows in an office environment". In: *Energy and Buildings* 113 (2016), pp. 123–132.

[61] A Kerrouche et al. “Luminescent solar concentrators: From experimental validation of 3D ray-tracing simulations to coloured stained-glass windows for BIPV”. In: *Solar Energy Materials and Solar Cells* 122 (2014), pp. 99–106.

[62] Guillaume Doudart de la Gree et al. “A new design for luminescent solar concentrating PV roof tiles”. In: *Photovoltaic Specialist Conference (PVSC), 2015 IEEE 42nd*. IEEE. 2015, pp. 1–5.

[63] Paul D Swift, Geoffrey B Smith, and Jim B Franklin. “Light-to-light efficiencies in luminescent solar concentrators”. In: *SPIE's International Symposium on Optical Science, Engineering, and Instrumentation*. International Society for Optics and Photonics. 1999, pp. 21–28.

[64] Paul D Swift and Geoff B Smith. “Color considerations in fluorescent solar concentrator stacks”. In: *Applied optics* 42.25 (2003), pp. 5112–5117.

[65] Alan A Earp et al. “Optimisation of a three-colour luminescent solar concentrator daylighting system”. In: *Solar Energy Materials and Solar Cells* 84.1 (2004), pp. 411–426.

[66] Chen Wang, H Abdul-Rahman, and SP Rao. “Daylighting can be fluorescent: Development of a fiber solar concentrator and test for its indoor illumination”. In: *Energy and Buildings* 42.5 (2010), pp. 717–727.

[67] Chen Wang, H Abdul-Rahman, and SP Rao. “A new design of luminescent solar concentrator and its trial run”. In: *International Journal of Energy Research* 34.15 (2010), pp. 1372–1385.

[68] B Vishwanathan et al. “A comparison of performance of flat and bent photovoltaic luminescent solar concentrators”. In: *Solar Energy* 112 (2015), pp. 120–127.

[69] Oreane Y Edelenbosch et al. “Luminescent solar concentrators with fiber geometry”. In: *Optics express* 21.103 (2013), A503–A514.

[70] Fatih Yilmaz, M Tolga Balta, and Resat Selbas. "A review of solar based hydrogen production methods". In: *Renewable and Sustainable Energy Reviews* 56 (2016), pp. 171–178.

[71] Tim Patterson et al. "Life cycle assessment of the electrolytic production and utilization of low carbon hydrogen vehicle fuel". In: *International Journal of Hydrogen Energy* 39.14 (2014), pp. 7190–7201.

[72] MY Azwar, MA Hussain, and AK Abdul-Wahab. "Development of biohydrogen production by photobiological, fermentation and electrochemical processes: A review". In: *Renewable and Sustainable Energy Reviews* 31 (2014), pp. 158–173.

[73] Z Abdin, CJ Webb, and E MacA Gray. "Solar hydrogen hybrid energy systems for off-grid electricity supply: A critical review". In: *Renewable and Sustainable Energy Reviews* 52 (2015), pp. 1791–1808.

[74] H Ahmad et al. "Hydrogen from photo-catalytic water splitting process: A review". In: *Renewable and Sustainable Energy Reviews* 43 (2015), pp. 599–610.

[75] A. Fujishima and K. Honda. "Electrochemical Photolysis of Water at a Semiconductor Electrode". In: *Nature* 238 (1972), pp. 37–78.

[76] Joel W Ager et al. "Experimental demonstrations of spontaneous, solar-driven photoelectrochemical water splitting". In: *Energy & Environmental Science* 8.10 (2015), pp. 2811–2824.

[77] Roel Van de Krol et al. *Photoelectrochemical hydrogen production*. Vol. 90. Springer, 2012.

[78] T Jesper Jacobsson et al. "Sustainable solar hydrogen production: from photoelectrochemical cells to PV-electrolyzers and back again". In: *Energy & Environmental Science* 7.7 (2014), pp. 2056–2070.

[79] Xavier Elias et al. "Neutral water splitting catalysis with a high FF triple junction polymer cell". In: *ACS Catalysis* (2016).

[80] Daniel G Nocera. "The artificial leaf". In: *Accounts of chemical research* 45.5 (2012), pp. 767–776.

[81] Peter Bogdanoff et al. "Artificial Leaf for Water Splitting Based on a Triple-Junction Thin-Film Silicon Solar Cell and a PEDOT: PSS/Catalyst Blend". In: *Energy Technology* (2016).

[82] T Jesper Jacobsson et al. "A monolithic device for solar water splitting based on series interconnected thin film absorbers reaching over 10% solar-to-hydrogen efficiency". In: *Energy & Environmental Science* 6.12 (2013), pp. 3676–3683.

[83] Matthias M May et al. "Efficient direct solar-to-hydrogen conversion by in situ interface transformation of a tandem structure". In: *Nature communications* 6 (2015).

[84] Jurga Juodkazyte et al. "Solar water splitting: efficiency discussion". In: *International Journal of Hydrogen Energy* (2016).

[85] Gerhard Peharz, Frank Dimroth, and Ursula Wittstadt. "Solar hydrogen production by water splitting with a conversion efficiency of 18%". In: *International Journal of Hydrogen Energy* 32.15 (2007), pp. 3248–3252.

[86] Katsushi Fujii et al. "Characteristics of hydrogen generation from water splitting by polymer electrolyte electrochemical cell directly connected with concentrated photovoltaic cell". In: *International Journal of Hydrogen Energy* 38.34 (2013), pp. 14424–14432.

[87] Akihiro Nakamura et al. "A 24.4% solar to hydrogen energy conversion efficiency by combining concentrator photovoltaic modules and electrochemical cells". In: *Applied Physics Express* 8.10 (2015), p. 107101.

[88] Canan Acar and Ibrahim Dincer. "Experimental investigation and analysis of a hybrid photoelectrochemical hydrogen production system". In: *International Journal of Hydrogen Energy* (2016).

[89] Yusuf Bicer and Ibrahim Dincer. “Experimental investigation of a PV-Coupled photoelectrochemical hydrogen production system”. In: *International Journal of Hydrogen Energy* (2016).

[90] John Stevens and Adam Z Weber. “A Theoretical Comparison of Optically Concentrating, Solar Water-Splitting Devices”. In: *Meeting Abstracts*. 37. The Electrochemical Society. 2015, pp. 1977–1977.

[91] MK Nowotny et al. “Observations of p-type semiconductivity in titanium dioxide at room temperature”. In: *Materials Letters* 64.8 (2010), pp. 928–930.

[92] Charles CL McCrory et al. “Benchmarking hydrogen evolving reaction and oxygen evolving reaction electrocatalysts for solar water splitting devices”. In: *Journal of the American Chemical Society* 137.13 (2015), pp. 4347–4357.

[93] Oscar Khaselev and John A Turner. “A monolithic photovoltaic-photoelectrochemical device for hydrogen production via water splitting”. In: *Science* 280.5362 (1998), pp. 425–427.

[94] Steven Y Reece et al. “Wireless solar water splitting using silicon-based semiconductors and earth-abundant catalysts”. In: *Science* 334.6056 (2011), pp. 645–648.

[95] Anna Hankin et al. “Photo-electrochemical production of H_2 using solar energy”. In: *Chemical Engineering Transactions* 41 (2014).

[96] Andebet Gedamu Tamirat et al. “Using hematite for photoelectrochemical water splitting: a review of current progress and challenges”. In: *Nanoscale Horizons* (2016).

[97] Craig A Grimes, Oomman K Varghese, and Sudhir Ranjan. *Light, water, hydrogen: the solar generation of hydrogen by water photoelectrolysis*. Springer Science & Business Media, 2007.

[98] Chin K Ong. "Design and performance of photoelectrochemical reactors with Fe_2O_3 photo-anodes for water splitting". PhD thesis. Imperial College London, 2013.

[99] *IQE - Enabling Advanced Technologies*. URL: http://www.iqep.com/.

[100] K.W.J. Barnham and G. Duggan. "A new approach to high-efficiency multi-band-gap solar cells". In: *Journal of Applied Physics* 67.7 (1990), pp. 3490–3493.

[101] D.C. Johnson et al. "Observation of photon recycling in strain-balanced quantum well solar cells". In: *Applied physics letters* 90.21 (2007), p. 213505.

[102] K. Lee et al. "Demonstration of photon coupling in dual multiple-quantum-well solar cells". In: *Photovoltaics, IEEE Journal of* 2.1 (2012), pp. 68–74.

[103] NJ Ekins-Daukes et al. "Controlling radiative loss in quantum well solar cells". In: *Journal of Physics D: Applied Physics* 46.26 (2013), p. 264007.

[104] HC Casey Jr, DD Sell, and KW Wecht. "Concentration dependence of the absorption coefficient for n- and p- type GaAs between 1.3 and 1.6 eV". In: *Journal of Applied Physics* 46.1 (1975), pp. 250–257.

[105] N. J. Ekins-Daukes. "An investigation into the efficiency of strained and strain-balanced quantum well solar cells". PhD thesis. Imperial College London, 1999.

[106] Keith Barnham and Dimitri Vvedensky. *Low-dimensional semiconductor structures: fundamentals and device applications*. Cambridge University Press, 2008.

[107] Simon M Sze and Kwok K Ng. *Physics of semiconductor devices*. John Wiley & Sons, 2006.

[108] World Economic Forum. *Repowering Transport*. 2011.

[109] Stuart A Scott et al. "Biodiesel from algae: challenges and prospects". In: *Current opinion in biotechnology* 21.3 (2010), pp. 277–286.

[110] Biofuels Digest admin. *What are - and who's making - 2G, 3G and 4G biofuels?* 2010. URL: http://www.biofuelsdigest.com/bdigest/2010/05/18/3g-4g-a-taxonomy-for-far-out--but-not-far-away--biofuels.

[111] T. Buckley. *Sustainability of Biofuels: Future Generations*. URL: http://biomassmagazine.com/articles/2070/sustainability-of-biofuels-future-generations.

[112] UK Department of Energy and Climate Change (DECC). *Energy Trends and Energy Prices December 2015*. 2015.

[113] AL Stephenson, JS Dennis, and SA Scott. "Improving the sustainability of the production of biodiesel from oilseed rape in the UK". In: *Process Safety and Environmental Protection* 86.6 (2008), pp. 427–440.

[114] Firoz Alam, Saleh Mobin, and Harun Chowdhury. "Third generation biofuel from algae". In: *Procedia Engineering* 105 (2015), pp. 763–768.

[115] Yusuf Chisti. "Biodiesel from microalgae". In: *Biotechnology advances* 25.3 (2007), pp. 294–306.

[116] Dang P Ho, Huu Hao Ngo, and Wenshan Guo. "A mini review on renewable sources for biofuel". In: *Bioresource Technology* 169 (2014), pp. 742–749.

[117] "Vijai K. Gupta et al. "Chapter 2 - Bioenergy Research: An Overview on Technological Developments and Bioresources". In: *Bioenergy Research: Advances and Applications*. Amsterdam: Elsevier, 2014, pp. 23–47.

[118] Paul Upham et al. "Substitutable biodiesel feedstocks for the UK: a review of sustainability issues with reference to the UK RTFO". In: *Journal of Cleaner Production* 17 (2009), S37–S45.

[119] Anna L Stephenson et al. "Influence of nitrogen-limitation regime on the production by Chlorella vulgaris of lipids for biodiesel feedstocks". In: *Biofuels* 1.1 (2010), pp. 47–58.

[120] Liliana Rodolfi et al. “Microalgae for oil: Strain selection, induction of lipid synthesis and outdoor mass cultivation in a low-cost photobioreactor”. In: *Biotechnology and bioengineering* 102.1 (2009), pp. 100–112.

[121] Ayhan Demirbas and Muhammet Fatih Demirbas. *Algae energy: algae as a new source of biodiesel*. Springer Science & Business Media, 2010.

[122] Jorge Alberto Vieira Costa and Michele Greque De Morais. “The role of biochemical engineering in the production of biofuels from microalgae”. In: *Bioresource technology* 102.1 (2011), pp. 2–9.

[123] Cíntia Simas-Rodrigues et al. “Microalgae for economic applications: advantages and perspectives for bioethanol”. In: *Journal of experimental botany* (2015), erv130.

[124] A Alaswad et al. “Technologies and developments of third generation biofuel production”. In: *Renewable and Sustainable Energy Reviews* 51 (2015), pp. 1446–1460.

[125] K. Hannis. “Optical behavior of algae particles in photobioreactors”. MA thesis. TU Delft, 2013.

[126] Ismail Rawat et al. “Biodiesel from microalgae: A critical evaluation from laboratory to large scale production”. In: *Applied Energy* 103 (2013), pp. 444–467.

[127] R. Slade and A. Bauen. “Micro-algae cultivation for biofuels: cost, energy balance, environmental impacts and future prospects”. In: *Biomass and Bioenergy* 53 (2013), pp. 29–38.

[128] Kanhaiya Kumar et al. “Recent trends in the mass cultivation of algae in raceway ponds”. In: *Renewable and Sustainable Energy Reviews* 51 (2015), pp. 875–885.

[129] James W Richardson, Myriah D Johnson, and Joe L Outlaw. “Economic comparison of open pond raceways to photo bio-reactors for profitable pro-

duction of algae for transportation fuels in the Southwest". In: *Algal Research* 1.1 (2012), pp. 93–100.

[130] David Chiaramonti et al. "Review of energy balance in raceway ponds for microalgae cultivation: re-thinking a traditional system is possible". In: *Applied Energy* 102 (2013), pp. 101–111.

[131] J.N. Rogers et al. "A critical analysis of paddlewheel-driven raceway ponds for algal biofuel production at commercial scales". In: *Algal Research* 4 (2014), pp. 76–88.

[132] DC Lynn et al. "High frequency algal pond harvest demonstration: a proof-of-principal in culture viability under applied algal farm management and operations with methodology comparisons in the evaluation and prediction of crop productivity and yield". In: *Center of Excellence for Hazardous Materials Management, Carlsbad, New Mexico* (2011).

[133] Adam R Brandt. "Converting oil shale to liquid fuels: Energy inputs and greenhouse gas emissions of the Shell in situ conversion process". In: *Environmental science & technology* 42.19 (2008), pp. 7489–7495.

[134] Carey W King. "Energy intensity ratios as net energy measures of United States energy production and expenditures". In: *Environmental Research Letters* 5.4 (2010), p. 044006.

[135] Colin M Beal et al. "Algal biofuel production for fuels and feed in a 100-ha facility: A comprehensive techno-economic analysis and life cycle assessment". In: *Algal Research* 10 (2015), pp. 266–279.

[136] Thomas E Murphy et al. "Vertical distribution of algal productivity in open pond raceways". In: *Algal Research* 11 (2015), pp. 334–342.

[137] Orlando Jorquera et al. "Comparative energy life-cycle analyses of microalgal biomass production in open ponds and photobioreactors". In: *Bioresource technology* 101.4 (2010), pp. 1406–1413.

[138] Anastasios Melis. "Solar energy conversion efficiencies in photosynthesis: minimizing the chlorophyll antennae to maximize efficiency". In: *Plant science* 177.4 (2009), pp. 272–280.

[139] Catharina Casper-Lindley and Olle Björkman. "Fluorescence quenching in four unicellular algae with different light-harvesting and xanthophyll-cycle pigments". In: *Photosynthesis research* 56.3 (1998), pp. 277–289.

[140] Alain Dauta et al. "Growth rate of four freshwater algae in relation to light and temperature". In: *Hydrobiologia* 207.1 (1990), pp. 221–226.

[141] Yecong Li et al. "Effect of light intensity on algal biomass accumulation and biodiesel production for mixotrophic strains Chlorella kessleri and Chlorella protothecoide cultivated in highly concentrated municipal wastewater". In: *Biotechnology and bioengineering* 109.9 (2012), pp. 2222–2229.

[142] Marcel Janssen et al. "Specific growth rate of Chlamydomonas reinhardtii and Chlorella sorokiniana under medium duration light/dark cycles: 13–87 s". In: *Journal of biotechnology* 70.1 (1999), pp. 323–333.

[143] Anastasios Melis, John Neidhardt, and John R Benemann. "Dunaliella salina (Chlorophyta) with small chlorophyll antenna sizes exhibit higher photosynthetic productivities and photon use efficiencies than normally pigmented cells". In: *Journal of Applied Phycology* 10.6 (1999), pp. 515–525.

[144] James C Ogbonna, Toshihiko Soejima, and Hideo Tanaka. "An integrated solar and artificial light system for internal illumination of photobioreactors". In: *Journal of Biotechnology* 70.1 (1999), pp. 289–297.

[145] Chun-Yen Chen et al. "Phototrophic hydrogen production in photobioreactors coupled with solar-energy-excited optical fibers". In: *International Journal of Hydrogen Energy* 33.23 (2008), pp. 6886–6895.

[146] Chun-Yen Chen et al. "Cultivation, photobioreactor design and harvesting of microalgae for biodiesel production: a critical review". In: *Bioresource technology* 102.1 (2011), pp. 71–81.

[147] Dan Dye et al. “Design and performance of a solar photobioreactor utilizing spatial light dilution”. In: *Journal of Solar Energy Engineering* 133.1 (2011), p. 015001.

[148] Jan-Willem F Zijffers et al. “Capturing sunlight into a photobioreactor: Ray tracing simulations of the propagation of light from capture to distribution into the reactor”. In: *Chemical Engineering Journal* 145.2 (2008), pp. 316–327.

[149] Martin Heining and Rainer Buchholz. “Photobioreactors with internal illumination–A survey and comparison”. In: *Biotechnology journal* 10.8 (2015), pp. 1131–1137.

[150] Chih-Yu Wang, Chun-Chong Fu, and Yung-Chuan Liu. “Effects of using light-emitting diodes on the cultivation of Spirulina platensis”. In: *Biochemical Engineering Journal* 37.1 (2007), pp. 21–25.

[151] Tomohisa Katsuda et al. “Astaxanthin production by Haematococcus pluvialis under illumination with LEDs”. In: *Enzyme and microbial technology* 35.1 (2004), pp. 81–86.

[152] Hans CP Matthijs et al. “Application of light-emitting diodes in bioreactors: Flashing light effects and energy economy in algal culture (Chlorella pyrenoidosa)”. In: *Biotechnology and Bioengineering* 50.1 (1996), pp. 98–107.

[153] Chin-Hang Shu et al. “Effects of light quality on the accumulation of oil in a mixed culture of Chlorella sp. and Saccharomyces cerevisiae”. In: *Journal of Chemical Technology and Biotechnology* 87.5 (2012), pp. 601–607.

[154] Probir Das et al. “Enhanced algae growth in both phototrophic and mixotrophic culture under blue light”. In: *Bioresource technology* 102.4 (2011), pp. 3883–3887.

[155] Shi-Kai Wang et al. “Microalgae cultivation in photobioreactors: An overview of light characteristics”. In: *Engineering in Life Sciences* 14.6 (2014), pp. 550–559.

[156] Yeong Hwan Seo et al. “Enhancement of growth and lipid production from microalgae using fluorescent paint under the solar radiation”. In: *Bioresource technology* 173 (2014), pp. 193–197.

[157] Hossein Delavari Amrei et al. “An integrated wavelength-shifting strategy for enhancement of microalgal growth rate in PMMA-and polycarbonate-based photobioreactors”. In: *European Journal of Phycology* 49.3 (2014), pp. 324–331.

[158] H Delavari Amrei et al. “Using fluorescent material for enhancing microalgae growth rate in photobioreactors”. In: *Journal of Applied Phycology* 27.1 (2015), pp. 67–74.

[159] L. Wondraczek et al. “Solar spectral conversion for improving the photosynthetic activity in algae reactors”. In: *Nature communications* 4 (2013).

[160] Seyedeh Fatemeh Mohsenpour, Bryce Richards, and Nik Willoughby. “Spectral conversion of light for enhanced microalgae growth rates and photosynthetic pigment production”. In: *Bioresource technology* 125 (2012), pp. 75–81.

[161] Seyedeh Fatemeh Mohsenpour and Nik Willoughby. “Luminescent photobioreactor design for improved algal growth and photosynthetic pigment production through spectral conversion of light”. In: *Bioresource technology* 142 (2013), pp. 147–153.

[162] Angela M Detweiler et al. “Evaluation of wavelength selective photovoltaic panels on microalgae growth and photosynthetic efficiency”. In: *Algal Research* 9 (2015), pp. 170–177.

[163] D. Farrell. *PVTrace Raytrace Model*. URL: https://github.com/danieljfarrell/pvtrace/wiki.

[164] D. Farrell. "Characterising the Performance of Luminescent Solar Concentrators". PhD thesis. Imperial College London, 2008.

[165] Renata Reisfeld and Christian K Jørgensen. "Luminescent solar concentrators for energy conversion". In: *Solar Energy Materials*. Springer, 1982, pp. 1–36.

[166] R. Reisfeld et al. "Luminescent solar concentrators based on thin films of polymethylmethacrylate on a polymethylmethacrylate support". In: *Solar Energy Materials* 17.6 (1988), pp. 439 –455.

[167] Mauro Pravettoni et al. "External quantum efficiency measurements of luminescent solar concentrators: a study of the impact of backside reflector size and shape". In: *Corresponding author.-Fax* 39.0 (2009), p. 332789268.

[168] Paul PC Verbunt et al. "Special dispersion chiral nematic reflectors for luminescent solar concentrators". In: *Photovoltaic Specialist Conference (PVSC), 2015 IEEE 42nd*. IEEE. 2015, pp. 1–6.

[169] Lu Xu et al. "Enhanced Photon Collection in Luminescent Solar Concentrators with Distributed Bragg Reflectors". In: *ACS Photonics* 3.2 (2016), pp. 278–285.

[170] Ryan Connell and Vivian E Ferry. "Integrating Photonics with Luminescent Solar Concentrators: Optical Transport in the Presence of Photonic Mirrors". In: *The Journal of Physical Chemistry C* (2016).

[171] M. Carrascosa, S. Unamuno, and F. Agullo-Lopez. "Monte Carlo simulation of the performance of PMMA luminescent solar collectors". In: *Appl. Opt.* 22.20 (1983), pp. 3236–3241.

[172] Michael Kasha. "Characterization of electronic transitions in complex molecules". In: *Discussions of the Faraday society* 9 (1950), pp. 14–19.

[173] George Gabriel Stokes. "On the change of refrangibility of light". In: *Philosophical Transactions of the Royal Society of London* 142 (1852), pp. 463–562.

[174] Gregory K Schenter, Bruce C Garrett, and Donald G Truhlar. "The role of collective solvent coordinates and nonequilibrium solvation in charge-transfer reactions". In: *The Journal of Physical Chemistry B* 105.40 (2001), pp. 9672–9685.

[175] EU Condon. "The Franck-Condon principle and related topics". In: *American journal of physics* 15.5 (1947), pp. 365–374.

[176] BASF. *Product literature for Lumogen*. 2016. URL: http://product-finder.basf.com/group/corporate/product-finder/en/overview-page:/Marke+Lumogen.

[177] *Franck-Condon Energy diagram*. URL: https://commons.wikimedia.org/wiki/File:Franck-Condon-diagram.png.

[178] *Franck-Condon absorption and emission peaks diagram*. URL: https://commons.wikimedia.org/wiki/File:Vibration-fluor-abs-fr.pngg.

[179] AD McNaught and AD Wilkinson. *International Union of Pure and Applied Chemistry (IUPAC)*. 1997.

[180] Mauro Mosca et al. "Hybrid LEDs Pave Way to New Lighting Applications". In: *Photonics Spectra* 47.4 (2013), pp. 60–64.

[181] Diego Alonso-Álvarez et al. "Luminescent down-shifting experiment and modelling with multiple photovoltaic technologies". In: *Progress in Photovoltaics: Research and Applications* 23.4 (2015), pp. 479–497.

[182] W.G.J.H.M. Van Sark et al. "Luminescent solar concentrators: a review of recent results". In: *Optics express [E]* 16.26 (2008), pp. 21773–21792.

[183] V. Sholin, J.D. Olson, and S.A. Carter. "Semiconducting polymers and quantum dots in luminescent solar concentrators for solar energy harvesting". In: *Journal of applied physics* 101.12 (2007), pp. 123114–123114.

[184] Rahul Bose et al. "The effect of size and dopant concentration on the performance of nanorod luminescent solar concentrators". In: *Proceedings of the 23rd European Photovoltaic Solar Energy Conference*. 2008.

[185] Lindsay R Wilson et al. “Characterization and reduction of reabsorption losses in luminescent solar concentrators”. In: *Applied optics* 49.9 (2010), pp. 1651–1661.

[186] P.P.C. Verbunt et al. “Anisotropic light emissions in luminescent solar concentrators–isotropic systems”. In: *Optics express* 21.103 (2013), A485–A493.

[187] Alan A Earp, Jim B Franklin, and Geoff B Smith. “Absorption tails and extinction in luminescent solar concentrators”. In: *Solar Energy Materials and Solar Cells* 95.4 (2011), pp. 1157–1162.

[188] M.G. Debije et al. “Promising fluorescent dye for solar energy conversion based on a perylene perinone”. In: *Appl. Opt.* 50.2 (2011), pp. 163–169.

[189] Pierpaolo Minei et al. “Cost-effective solar concentrators based on red fluorescent Zn (ii)–salicylaldiminato complex”. In: *RSC Advances* 6.21 (2016), pp. 17474–17482.

[190] Marco Carlotti et al. “Enhancing optical efficiency of thin-film luminescent solar concentrators by combining energy transfer and stacked design”. In: *Journal of Luminescence* 171 (2016), pp. 215–220.

[191] Riccardo Turrisi et al. “Stokes shift/emission efficiency trade-off in donor–acceptor perylenemonoimides for luminescent solar concentrators”. In: *Journal of Materials Chemistry A* 3.15 (2015), pp. 8045–8054.

[192] Rabih O Al-Kaysi et al. “The photophysical properties of chromophores at high (100 mM and above) concentrations in polymers and as neat solids”. In: *Physical Chemistry Chemical Physics* 8.29 (2006), pp. 3453–3459.

[193] Th Förster. “Intramolecular energy transfer and fluorescene”. In: *Ann. Phys* 2 (1948), p. 55.

[194] Adam P Green and Alastair R Buckley. “Solid state concentration quenching of organic fluorophores in PMMA”. In: *Physical Chemistry Chemical Physics* 17.2 (2015), pp. 1435–1440.

[195] Daniel J Farrell and Megumi Yoshida. “Operating regimes for second generation luminescent solar concentrators”. In: *Progress in Photovoltaics: Research and Applications* 20.1 (2012), pp. 93–99.

[196] WRL Thomas, JM Drake, and ML Lesiecki. “Light transport in planar luminescent solar concentrators: the role of matrix losses”. In: *Applied optics* 22.21 (1983), pp. 3440–3450.

[197] J. Sansregret et al. “Light transport in planar luminescent solar concentrators: the role of DCM self-absorption”. In: *Appl. Opt.* 22.4 (1983), pp. 573–577.

[198] M.J. Kastelijn, C.W.M. Bastiaansen, and M.G. Debije. “Influence of waveguide material on light emission in luminescent solar concentrators”. In: *Optical Materials* 31.11 (2009), pp. 1720 –1722. ISSN: 0925-3467.

[199] Rapp C.F. and Boling N.L. “Solar collector structures containing thin film polysiloxane and solar cells”. Pat. US 7915210. 1979.

[200] M. Buffa et al. “Dye-doped polysiloxane rubbers for luminescent solar concentrator systems”. In: *Solar Energy Materials and Solar Cells* 103.0 (2012), pp. 114 –118.

[201] P. Polishuk. “Plastic optical fibers branch out”. In: *Communications Magazine, IEEE* 44.9 (2006), pp. 140–148.

[202] G. Griffini, M.Levi, and S. Turri. “Novel crosslinked host matrices based on fluorinated polymers for long-term durability in thin-film luminescent solar concentrators”. In: *Solar Energy Materials and Solar Cells* 118.0 (2013), pp. 36 –42.

[203] M.J. Currie et al. “High-Efficiency Organic Solar Concentrators for Photovoltaics”. In: *Science* 321.5886 (2008), pp. 226–228.

[204] S.J. Gallagher, P.C. Eames, and B. Norton. “Quantum dot solar concentrator behaviour, predicted using a ray trace approach”. In: *International journal of ambient energy* 25.1 (2004), pp. 47–56.

[205] *Weatherall - CLAREX U.V. TRANSMISSION FILTER.* URL: http://weatherall-uk.com/clarex-acrylic/uvtran.html.

[206] J.S. Batchelder, A.H. Zewail, and T. Cole. "Luminescent solar concentrators. 1: Theory of operation and techniques for performance evaluation". In: *Appl. Opt.* 18.18 (1979), pp. 3090–3110.

[207] J.S. Batchelder, A.H. Zewail, and T. Cole. "Luminescent solar concentrators. 2: Experimental and theoretical analysis of their possible efficiencies". In: *Appl. Opt.* 20.21 (1981), pp. 3733–3754.

[208] K.R. McIntosh, N. Yamada, and B.S. Richards. "Theoretical comparison of cylindrical and square-planar luminescent solar concentrators". In: *Applied Physics B* 88.2 (2007), pp. 285–290.

[209] Giuseppe Colantuono, Alastair Buckley, and Robert Erdélyi. "Ray-optics modelling of rectangular and cylindrical 2-layer solar concentrators". In: *Journal of Lightwave Technology* 31.7 (2013), pp. 1033–1044.

[210] Wenxuan Wu et al. "Hybrid solar concentrator with zero self-absorption loss". In: *Solar Energy* 84.12 (2010), pp. 2140–2145.

[211] Sandra FH Correia et al. "High-efficiency luminescent solar concentrators for flexible waveguiding photovoltaics". In: *Solar Energy Materials and Solar Cells* 138 (2015), pp. 51–57.

[212] R.H. Inman et al. "Cylindrical luminescent solar concentrators with near-infrared quantum dots". In: *Opt. Express* 19 (2011), pp. 24308–24313.

[213] T. Wang et al. "A theoretical model of a cylindrical luminescent solar concentrator with a dye-doping coating". In: *Journal of Optics* 15.5 (2013), p. 055709.

[214] Esmaeil-Hooman Banaei and Ayman F Abouraddy. "Design of a polymer optical fiber luminescent solar concentrator". In: *Progress in Photovoltaics: Research and Applications* 23.4 (2015), pp. 403–416.

[215] Esmaeil-Hooman Banaei and Ayman F Abouraddy. "Fiber luminescent solar concentrator with 5.7% conversion efficiency". In: *SPIE Solar Energy+ Technology*. International Society for Optics and Photonics. 2013, pp. 882102–882102.

[216] Jongseung Yoon et al. "Flexible concentrator photovoltaics based on microscale silicon solar cells embedded in luminescent waveguides". In: *Nature communications* 2 (2011), p. 343.

[217] Carley Corrado et al. "Optimization of gain and energy conversion efficiency using front-facing photovoltaic cell luminescent solar concentratordesign". In: *Solar Energy Materials and Solar Cells* 111 (2013), pp. 74–81.

[218] Efthymios Klampaftis et al. "Enhancing the performance of solar cells via luminescent down-shifting of the incident spectrum: A review". In: *Solar Energy Materials and Solar Cells* 93.8 (2009), pp. 1182–1194.

[219] Efthymios Klampaftis et al. "Increase in short-wavelength response of encapsulated CIGS devices by doping the encapsulation layer with luminescent material". In: *Solar Energy Materials and Solar Cells* 101 (2012), pp. 62–67.

[220] David Ross et al. "The impact of luminescent down shifting on the performance of CdTe photovoltaics: impact of the module vintage". In: *Photovoltaics, IEEE Journal of* 4.1 (2014), pp. 457–464.

[221] Efthymios Klampaftis, David Ross, and Bryce S Richards. "Color, graphic design and high efficiency for photovoltaic modules". In: *Photovoltaic Specialist Conference (PVSC), 2014 IEEE 40th*. IEEE. 2014, pp. 0025–0029.

[222] R. Bose et al. "Resonance energy transfer in luminescent solar concentrators". In: *Photovoltaic Specialists Conference (PVSC), 2010 35th IEEE*. IEEE. 2010, pp. 000467–000470.

[223] Zachar Krumer et al. "Exploration of parameters influencing the self-absorption losses in luminescent solar concentrators with an experimentally validated combined ray-tracing/Monte-Carlo model". In: *SPIE Solar Energy+ Tech-*

nology. International Society for Optics and Photonics. 2013, pp. 882104–882104.

[224] R. Bose et al. "Luminescent solar concentrators: Nanorods and raytrace modeling". In: *Photovoltaic Specialists Conference, 2008. PVSC'08. 33rd IEEE*. IEEE. 2008, pp. 1–5.

[225] Donald D Chamberlin and Raymond F Boyce. "SEQUEL: A structured English query language". In: *Proceedings of the 1974 ACM SIGFIDET (now SIGMOD) workshop on Data description, access and control*. ACM. 1974, pp. 249–264.

[226] Maurice Herlihy and Nir Shavit. *The Art of Multiprocessor Programming, Revised Reprint*. Elsevier, 2012.

[227] *Parallel Python*. URL: http://www.parallelpython.com/.

[228] *RAMdisk from Dataram*. URL: http://memory.dataram.com/products-and-services/software/ramdisk.

[229] *Intersection of a Line and a Cone*. URL: http://www.geometrictools.com/Documentation/IntersectionLineCone.pdf.

[230] Paul Heckbert. *Graphics Gems IV*. Academic Press, 1994.

[231] Alan W Paeth. *Graphics Gems V*. Academic Press, 2014.

[232] *The Little Grasshopper: Graphics Programming Tips - Mesh Generation with Python*. URL: http://prideout.net/blog/?p=44.

[233] Randy L Haupt and Sue Ellen Haupt. *Practical genetic algorithms*. John Wiley & Sons, 2004.

[234] Mauro Pravettoni et al. "Characterization of CPV cells on a high intensity solar simulator: a detailed uncertainty analysis". In: *Photovoltaic Specialists Conference (PVSC), 2011 37th IEEE*. IEEE. 2011, pp. 001762–001767.

[235] KWJ Barnham et al. "Quantum well solar cells". In: *Physica E: Low-dimensional Systems and Nanostructures* 14.1 (2002), pp. 27–36.

[236] M Paxman et al. “Modeling the spectral response of the quantum well solar cell”. In: *Journal of Applied Physics* 74.1 (1993), pp. 614–621.

[237] JP Connolly et al. “Efficiency limits of quantum well solar cells”. In: *arXiv preprint arXiv:1006.1835* (2010).

[238] Mathworks. *Matlab*. URL: https://uk.mathworks.com/products/matlab/.

[239] WG Spitzer and JM Whelan. “Infrared absorption and electron effective mass in n-type gallium arsenide”. In: *Physical Review* 114.1 (1959), p. 59.

[240] John S Burlew. “Algal culture”. In: *From Laboratory to Pilot Plant, Carnegie Inst. Washington Publ* 600.1 (1953).

[241] William J Oswald and Claeence G Golueke. “Biological transformation of solar energy”. In: *Advances in applied microbiology* 2 (1960), pp. 223–262.

[242] John Downing. *Effects of Light Absorption and Scattering in Water Samples on OBS Measurements*. Tech. rep. Campbell Scientific, Inc, 2008.

[243] Halil Berberoglu, Juan Yin, and Laurent Pilon. “Light transfer in a bubble sparged photobioreactor for simultaneous hydrogen production and CO2 mitigation”. In: *Comput Therm Radiations in Participating Media II* (2006).

[244] Haan Volten et al. “Laboratory measurements of angular distributions of light scattered by phytoplankton and silt”. In: *Limnology and Oceanography* 43.6 (1998), pp. 1180–1197.

[245] Amanda L Whitmire et al. “Spectral backscattering properties of marine phytoplankton cultures”. In: *Optics Express* 18.14 (2010), pp. 15073–15093.

[246] MW Matthews and S Bernard. “Using a two-layered sphere model to investigate the impact of gas vacuoles on the inherent optical properties of Microcystis aeruginosa”. In: (2013).

[247] Arturo Quirantes and Stewart Bernard. “Light scattering by marine algae: two-layer spherical and nonspherical models”. In: *Journal of Quantitative Spectroscopy and Radiative Transfer* 89.1 (2004), pp. 311–321.

[248] Mark N Merzlyak et al. “Light absorption and scattering by cell suspensions of some cyanobacteria and microalgae”. In: *Russian Journal of Plant Physiology* 55.3 (2008), pp. 420–425.

[249] Wen Zhou et al. “Variations in the optical scattering properties of phytoplankton cultures”. In: *Optics express* 20.10 (2012), pp. 11189–11206.

[250] Arturo Quirantes and Stewart Bernard. “Light-scattering methods for modelling algal particles as a collection of coated and/or nonspherical scatterers”. In: *Journal of Quantitative Spectroscopy and Radiative Transfer* 100.1 (2006), pp. 315–324.

[251] B Rylander and S Gotshall. “Optimal population size and the genetic algorithm”. In: *Population* 100.400 (2002), p. 900.

[252] JCH Peeters and P Eilers. “The relationship between light intensity and photosynthesis—a simple mathematical model”. In: *Hydrobiological Bulletin* 12.2 (1978), pp. 134–136.

[253] Hee-Jeong Choi and Seung-Mok Lee. “Effect of temperature, light intensity and ph on the growth rate of chlorella vulgaris”. In: *Journal of Korean Society of Environmental Engineers* 33.7 (2011), pp. 511–515.

[254] RJ Ritchie and AWD Larkum. “Modelling photosynthesis in shallow algal production ponds”. In: *Photosynthetica* 50.4 (2012), pp. 481–500.

[255] Ana L Goncalves, Jose CM Pires, and Manuel Simoes. “The effects of light and temperature on microalgal growth and nutrient removal: an experimental and mathematical approach”. In: *RSC Advances* 6.27 (2016), pp. 22896–22907.

[256] Michalis Kanellis et al. “The solar noise barrier project: 1. Effect of incident light orientation on the performance of a large-scale luminescent solar concentrator noise barrier”. In: *Renewable Energy* (2016).

[257] Continuum Analytics. *CUDA*. URL: https://developer.nvidia.com/how-to-cuda-python.

[258] Andreas Kl'ockner. *PyCUDA*. URL: https://mathema.tician.de/software/pycuda/.